

# In Situ Characterization of Thin Films Utilizing Second Harmonic Generation

Mikkel Aarup Buch & Nicolai Sennels  
Nanomaterials and Nanophysics, 2019-06

Master Thesis





**AALBORG UNIVERSITY**  
STUDENT REPORT

Department of Materials and Production  
Aalborg University  
<http://www.nano.aau.dk/>

**Title:**  
In Situ Characterization of Thin Films  
Utilizing Second Harmonic Generation

**Theme:**  
Applied Nanotechnology

**Project Period:**  
Autumn Semester 2018  
- Spring Semester 2019

**Project Group:**  
Group 5.326

**Participant(s):**  
Nicolai Sennels  
Mikkel Aarup Buch

**Supervisor(s):**  
Kjeld Pedersen

**Copies:** 2

**Page Numbers:** 100

**Date of Completion:**  
June 9, 2019

**Abstract:**

The aim of this project is to investigate second harmonic generation (SHG) as a method for in situ characterization of Thin Films. The report covers the basics of nonlinear optics, SHG, low energy electron diffraction (LEED), Optical Parametric Oscillator (OPO), and substrate surface theory. Furthermore, a method section describing the different setups, methods, and software used throughout the project. The SHG response from Si, Si/SiO<sub>2</sub> and hydrogen terminated Si surfaces have been studied as a preparation for the in situ measurements. In situ measurements were carried out on silver (Ag), aluminum (Al) and aluminum nitride (AlN), where Ag showed a strong correlation between the film thickness and the SHG signal. Furthermore, a correlation between crystallinity and SHG signal was observed on the AlN films. Finally, an outlook with a design for an industrial SHG setup, build upon the findings of this project.

*The content of this report is restricted, publication (with reference) may only be pursued due to agreement with the author.*

# Contents

<b>Preface</b>	<b>v</b>
<b>1 Introduction</b>	<b>1</b>
1.1 Nonlinear Optics . . . . .	3
1.2 Second Harmonic Generation . . . . .	4
1.3 Aluminum Nitride . . . . .	10
1.4 Surface of Substrate . . . . .	11
1.5 Low Energy Electron Diffraction . . . . .	13
1.6 Optical Parametric Oscillator . . . . .	14
<b>2 Method</b>	<b>17</b>
2.1 Vacuum and Film Deposition . . . . .	17
2.2 Optical Setup . . . . .	24
2.3 AlN Setup . . . . .	29
2.4 Characterization . . . . .	30
2.5 Software . . . . .	32
<b>3 Results and Discussion</b>	<b>33</b>
3.1 Low Energy Electron Diffraction . . . . .	33
3.2 Azimuthal Angle Setup . . . . .	36
3.3 Nonlinear Spectroscopy on Si . . . . .	38
3.4 Evaporation Rate . . . . .	39
3.5 Atomic Force Microscopy . . . . .	41
3.6 Evaporation of Ag . . . . .	48
3.7 First AlN Setup . . . . .	56
3.8 Nonlinear Spectroscopy in Azimuthal Angle Setup. . . . .	64
3.9 Second AlN Setup . . . . .	65
3.10 Femtosecond Laser . . . . .	71
3.11 Obstacles and Experiences . . . . .	72
<b>4 Conclusion</b>	<b>75</b>

<b>5 Outlook</b>	<b>77</b>
5.1 Model of SHG Setup . . . . .	77
5.2 Methods for Comparison of SHG Measurements . . . . .	81
<b>Bibliography</b>	<b>83</b>
<b>A Temperature Measurements</b>	<b>91</b>
<b>B AFM Histograms</b>	<b>93</b>
<b>C Equipment</b>	<b>95</b>
<b>D <math>d_{eff}</math> calculations for AlN</b>	<b>99</b>

# Preface

This report is written by group 5.326 consisting of fourth-semester Nanomaterials and Nanophysics students of Aalborg University from September 4th to June 10th. The report is written in collaboration with the company Polyteknik A/S, with Professor Kjeld Pedersen as the primary supervisor. A special thanks to Christian Kjelde for being the communication link between us and Polyteknik. A special thanks also goes to Peter Kjær Kristensen, for helping with experiments, measurements, and setup maintenance. The topic of this project is the utilization of SHG for in situ measurements. This report includes a brief introduction to the state of the art which covers thin films, optics, and the motivation behind the project. The report includes sections describing nonlinear optics, low energy electron diffraction, the interface between film and substrate, and optical parametric oscillator. A method chapter will follow with a description of the experiments, setups, and software used, leading to a chapter with results and discussion, which will end in a conclusion with an outlook. Throughout this report, each chapter and section will have numbered titles. Furthermore, all significant equations and tables will be numbered. The reference system applied is the numerical system and every reference is then represented by a [number], which refers directly to a specific source in the bibliography. Figures with no reference are composed by the group itself.

Aalborg University, June 9, 2019

---

Nicolai Sennels  
nsenne14@student.aau.dk

---

Mikkel Aarup Buch  
mab14@student.aau.dk



# Chapter 1

## Introduction

Often when working with thin film deposition, especially in industry, it is based on Physical Vapor Deposition (PVD) in a vacuum system. When working with thin films, many factors have an influence and thus development of new films relies primarily on trial and error. This is especially true when working with a deposition rate higher than that of molecular beam epitaxy (MBE). [1] In order to get a proper understanding of the film growth over time, many experiments are required and need to be analyzed individually, which is very time consuming and not very cost efficient. This can pose a severe problem as the quality of the film can have an influence on the properties. Duquenne et al. [2] report a big difference in the thermal conductivity of aluminum nitride (AlN) films grown by reactive magnetron sputtering, depending on the crystallization of the film. This is why developing a technique for characterization of the films during the growth is such a potent tool, as it could drastically decrease the number of experiments needed for the most optimal result. [3]

The field of optics is the study of light and the interaction between light and its surroundings. Often in optics, the linear part is sufficient in order to describe lenses, mirrors, and diffraction. In a linear environment, if red light enters a material, a red light will exit. With high-power lasers, nonlinear effects may appear. Under illumination, a material can cause a change in frequency, generating a wave with twice the frequency (half the wavelength), which is called second harmonic generation (SHG) and is a possible outcome of nonlinear optics (NLO). [4]

One of the main reasons NLO initially wasn't a big topic of discussion, was due to the electric field strength used in research at that time. Since the applied electric fields were too weak in comparison to the fields inside the atoms and molecules, the perturbations were too small, thus the nonlinear response was too small to reliably measure. One of the first indications of a nonlinear relation was found by John Kerr in the 1870s when he demonstrated a slight change in the refractive

index of solids and liquids by applying a strong DC field [5], later the phenomenon was named after Kerr as the DC Kerr effect. [6] This was furthered in 1961 when Franken et al. [7] were the first to demonstrate SHG in a quartz crystal, using the setup shown in Figure 1.1 [7, 8].

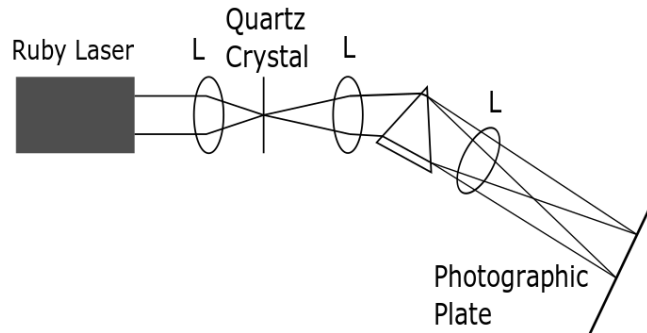


**Figure 1.1:** Schematic of the first setup to show second harmonic generation by Franken et al. [7]

The following year after Armstrong et al. [9] laid the theoretical foundation for wave mixing in nonlinear media [8, 9], which was later improved by Bloembergen and Pershan by adding better boundary conditions [8, 10]. The theory was confirmed by experiments on semiconductors [8, 11] and metals [8, 12]. Based on the research from these groups, the field of nonlinear optics on surfaces and SHG really took off. [8]

An example of modern applications of SHG is green laser pointers, as the wave generated has half the wavelength of the incident light and can thus generate green light from infrared light. Many photochemical processes, such as photocatalysis [13, 14], photosynthesis [13, 15] and photoresists [13, 16] for lithography are governed by the low wavelengths, able to be generated through SHG. [13] Paul Campagnola [17] has shown SHG microscopy can get to sub-micron resolution using a femtosecond laser to image and detect cancer in the early stages. It can also be used as a probe for different properties such as crystallinity and general characterization of materials. [4] Hu et al. [18] were able to determine the precise crystallographic orientation in zinc sulfide nanowires.

An important factor for SHG is the symmetry in the material, as SHG is forbidden in materials with inversion symmetry, which is illustrated in Figure 1.2. Figure 1.2 shows a nonlinear medium, a centrosymmetric medium (medium with inversion symmetry), and the generation of the second harmonic waves with double the fundamental frequency. This can be utilized to characterize specific areas. An example of broken symmetry is a surface. This allows for characterization of

the film at the film/air and film/substrate interfaces for thin films and coatings. For non-centrosymmetric films the film itself can be probed as well.

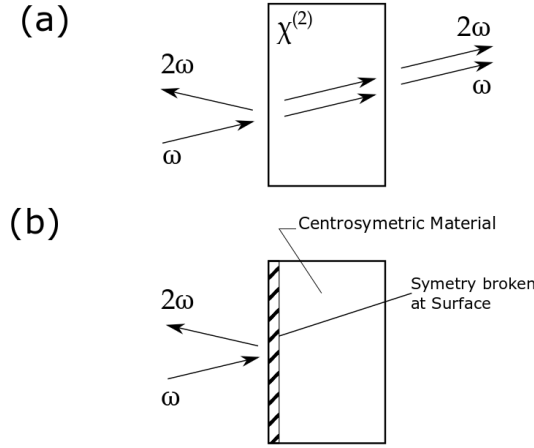


**Figure 1.2:** Illustration of SHG in reflection at the surface of a) a second-order nonlinear optical material and b) a centrosymmetric nonlinear optical material.

## 1.1 Nonlinear Optics

Optics is studying how molecules and atoms respond to electromagnetic (EM) fields. For many years the relation between the polarization of the medium in question  $P$  and the applied electric field  $E$  was thought to be linear

$$P = \epsilon_0 \chi^{(1)} E, \quad (1.1)$$

where  $\chi^{(1)}$  is the linear susceptibility and  $\epsilon_0$  is the vacuum permittivity. Equation 1.1 further dictates the electric displacement as

$$D = \epsilon_0 E + P = \epsilon_0 (1 + \chi^{(1)}) E = \epsilon \epsilon_0 E, \quad (1.2)$$

where  $\epsilon = 1 + \chi^{(1)}$  is known as the relative dielectric constant. The main reason this assumption held up was due to the strength of the electric field used at the time, as mentioned in Section 1. The fields inside the atoms and molecules were far greater than the fields applied and thus were not significantly affected, thereby not giving a large enough response to be considered. [6]

The electric susceptibilities contain a lot of information about the medium.  $\chi^{(1)}$  is a second order tensor and contain information about refraction and reflection. Equation 1.1 can be expanded when working with strong electric fields to

$$P = \epsilon_0 [\chi^{(1)} \cdot E + \chi^{(2)} : EE + \chi^{(3)} : EEE + \dots] \quad (1.3)$$

$$\equiv P^{(1)} + P^{(2)} + P^{(3)} + \dots$$

With  $\chi^{(2)}$  and  $\chi^{(3)}$  being the second and third order susceptibilities respectively, with  $\chi^{(2)}$  being the primary interest of this report. [6] These susceptibilities are actually tensors of second, third, and fourth rank respectively going from the linear to the third order susceptibility, thus  $\chi^{(n)}$  being the susceptibility of the  $n$ th-order would be a tensor of  $n + 1$  rank. These tensors can be written as a matrix where the rank determines the dimensionality of the matrix, so Equation 1.3 can be rewritten as

$$P_i = \epsilon_0 \left( \sum_j \chi_{ij}^{(1)} E_j + \sum_{jk} \chi_{ijk}^{(2)} E_j E_k + \sum_{jkl} \chi_{ijkl}^{(3)} E_j E_k E_l \right), \quad (i, j, k, l) = (x, y, z). \quad (1.4)$$

Here summation over repeated indices is applied. [6] This could indicate the second order susceptibility  $\chi_{ijk}^{(2)}$  has  $3^3 = 27$  components, though this problem can be simplified for many common nonlinear crystals as many elements will turn zero. [6] This will be discussed further in Section 1.2.1.

It is always possible to make a Taylor expansion of any function, though if the function indeed was linear the higher order coefficients would be zero. In the case of NLO, the function turns nonlinear under a strong field with high intensity and thus the coefficients are non-zero. The coefficients get smaller as the order increases, thus a stronger field is needed to study higher orders.

## 1.2 Second Harmonic Generation

By taking a closer look at Equation 1.4 it is apparent that other frequencies than the fundamental frequency can contribute to the polarization. Focusing on the second order term given as

$$\mathbf{P}^{(2)}(t) = \epsilon_0 \chi^{(2)} \mathbf{E}(t)^2. \quad (1.5)$$

The incoming field can be written as  $\mathbf{E}(t) = \mathbf{E}e^{-i\omega t}$  and putting into Equation 1.5 gives

$$\mathbf{P}^{(2)}(t) = \epsilon_0 \chi^{(2)} \mathbf{E}^2 e^{-i2\omega t}. \quad (1.6)$$

Looking at Equation 1.6 it is noticeable that the nonlinear polarization has a component radiating at double the input frequency, later referred to as the fundamental frequency, giving the characteristic second harmonic generation. SHG is a specific case of sum frequency generation (SFG) with two photons of the same frequency merging to one photon with double the frequency. [6, 4]

### 1.2.1 Symmetry Considerations

As mentioned earlier, often when working with the second order susceptibility, many elements becomes zero. This is mainly due to symmetry. Considering the Neumann principle, the properties of a material and its corresponding tensor must have the same symmetry. A material with a center of inversion symmetry is known as centrosymmetric and is invariant under transformation. Performing the operation  $\mathbf{r} \rightarrow -\mathbf{r}$ , does not affect the media if centrosymmetric, but requires the electric field and polarization to also follow in a similar manner, by adding a minus sign to both  $\mathbf{P} \rightarrow -\mathbf{P}$  and  $\mathbf{E} \rightarrow -\mathbf{E}$ . For this to hold true all  $\chi^{(n)}$  with an even value for  $n$  must be zero. This is apparent when looking at Equation 1.4. [19, 20]

The tensors related to NLO can be rather complex before making any assumptions or simplifications. These simplifications are based on the crystallinity and symmetry of the probing area, as bulk, surface, and interfaces between layers have different symmetries. Though, some general symmetry considerations can be made in order to more easily calculate the tensor elements.

Earlier the possibility of 27 components of  $\chi_{ijk}^{(2)}$  was mentioned, but this can be reduced to 18. Essentially  $\chi_{ijk}^{(2)}(\omega_3 = \omega_1 + \omega_2)$  is dependant on the fundamental frequency, with  $\omega_1$  and  $\omega_2$  being the fundamental frequencies and  $\omega_3$  being the generated sum frequency. In case of SHG  $\omega_1 = \omega_2$ , thus leading to  $\chi_{ijk}^{(2)} = \chi_{ikj}^{(2)} = 2d_{i(jk)} = 2d_{il}$  where  $d_{il}$  is known as the nonlinear susceptibility coefficient. The new notation will be as follow

i:	x	1	jk=l:	xx	1
	y	2		yy	2
	z	3		zz	3
				yz=zy	4
				xz=zx	5
				xy=yx	6

and thus the nonlinear coefficient tensor can be reduced to a  $3 \times 6$  matrix with only 18 elements

$$d_{il} = \begin{bmatrix} d_{11} & d_{12} & d_{13} & d_{14} & d_{15} & d_{16} \\ d_{21} & d_{22} & d_{23} & d_{24} & d_{25} & d_{26} \\ d_{31} & d_{32} & d_{33} & d_{34} & d_{35} & d_{36} \end{bmatrix}. \quad (1.7)$$

This notation contraction can be more generally applied if the optical frequencies are much smaller than the resonance frequency of the medium, it can then be assumed to be a lossless medium and thus full permutation symmetry can be

applied. This allows for indices to be permuted as long as the frequencies are permuted as well, but since  $\chi^{(2)}$ , in this case, is independent of frequency, it is not necessary to permute the frequency. This results in

$$\begin{aligned}\chi_{ijk}^{(2)}(\omega_3 = \omega_1 + \omega_2) &= \chi_{jki}^{(2)}(\omega_3 = \omega_1 + \omega_2) = \chi_{kij}^{(2)}(\omega_3 = \omega_1 + \omega_2) \\ &= \chi_{ikj}^{(2)}(\omega_3 = \omega_1 + \omega_2) = \chi_{jik}^{(2)}(\omega_3 = \omega_1 + \omega_2) \\ &= \chi_{kji}^{(2)}(\omega_3 = \omega_1 + \omega_2)\end{aligned}\tag{1.8}$$

and is known as the Kleinman symmetry condition (KSC). [4, 21] Not only does the KSC allow the contracted notation to be applied more generally for three-wave mixing, but also reduces the number of independent elements for SHG from 18 to 10. The new tensor can thus be written as

$$\begin{bmatrix} d_{11} & d_{12} & d_{13} & d_{14} & d_{15} & d_{16} \\ d_{21} & d_{22} & d_{23} & d_{24} & d_{25} & d_{26} \\ d_{31} & d_{32} & d_{33} & d_{34} & d_{35} & d_{36} \end{bmatrix} \rightarrow \begin{bmatrix} d_{11} & d_{12} & d_{13} & d_{14} & d_{15} & d_{16} \\ \mathbf{d}_{16} & d_{22} & d_{23} & d_{24} & \mathbf{d}_{14} & \mathbf{d}_{12} \\ \mathbf{d}_{15} & \mathbf{d}_{24} & d_{33} & \mathbf{d}_{23} & \mathbf{d}_{13} & \mathbf{d}_{14} \end{bmatrix}.\tag{1.9}$$

This way of writing the coefficient and its tensor elements is more often used in experimental physics compared to  $\chi_{ijk}^{(2)}$  which is preferred in theory. Another difference in literature is whether  $\epsilon_0$  is included in  $\chi^{(2)}$  or not in which the relation may also be written as  $d_{ijk} = \frac{1}{2}\epsilon_0\chi_{ijk}^{(2)}$ . [4, 6, 22]

In this project, the focus is examining the surface of the (111) face of silicon, referred to as Si(111) and depositing a thin layer of either silver (Ag), aluminum (Al) or AlN on it. The equation for calculating the tensor used in this report is developed by J.E. Sipe et al. [23] looking at reflected second harmonic generation from cubic centrosymmetric crystal surfaces (such as Si). Sipe et al. assume an unreconstructed Si(111) surface with a diamond lattice and considering the 3 uppermost layers, as seen in Figure 1.3. The surface possesses  $C_{3v}$  symmetry, which is known as Schoenflies notation.  $C_{3v}$  means a cyclic symmetry with 3 fold rotation ( $120^\circ$  rotation is needed for similar orientation) and 3 mirror planes [24, 25].

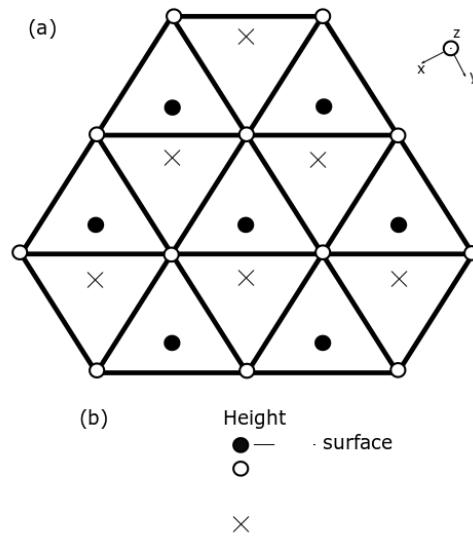


**Figure 1.3:** Atomic Layer for the first 3 layers of a Si(111) face as considered by Sipe et al. [23]

Often in literature, another symmetry notation is seen, the Hermann-Mauguin notation, in which the Si(111) would have a  $3m$  symmetry [24]. Studies have shown the same symmetry for a  $7 \times 7$  reconstruction of Si(111) [26]. The tensor matrix for the (111) face with  $C_{3v}$  symmetry, and the y-axis perpendicular to the plane of symmetry, becomes [23]

$$\begin{bmatrix} P_x^s \\ P_y^s \\ P_z^s \end{bmatrix} = \begin{bmatrix} d_{11} & -d_{11} & 0 & 0 & d_{15} & 0 \\ 0 & 0 & 0 & d_{15} & 0 & -d_{11} \\ d_{31} & d_{31} & d_{33} & 0 & 0 & 0 \end{bmatrix} \begin{bmatrix} E_x^2 \\ E_y^2 \\ E_z^2 \\ 2E_y E_z \\ 2E_x E_z \\ 2E_x E_y \end{bmatrix}. \quad (1.10)$$

Equation 1.10 shows  $d_{11}$  must be zero for an isotropic surface, if looking at the xy-plane, applying an electric field in x or y direction should only affect the polarization in the respective direction, this will only hold true if  $d_{11} = 0$  for an isotropic surface. Thus  $d_{11}$  contains information about the surface disorder and further the crystallinity.

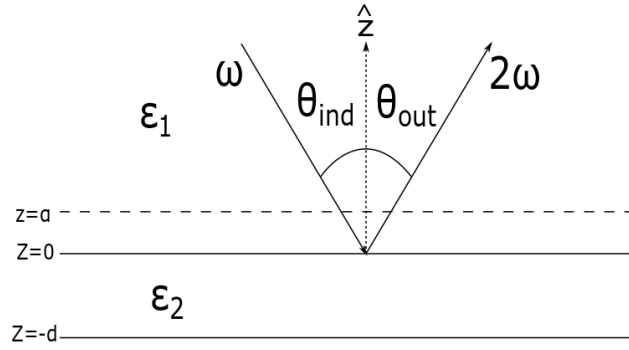


**Figure 1.4:** Geometry of an interface at  $z = 0$  and a polarization sheet at  $z = \alpha$ .

Sipe et al. [23] found an expression for the total second harmonic field, taking into account both bulk and surface contributions for p-polarized pump beams for a (111) crystal face. This is based on looking at the fields in vacuum generated by a source polarization, represented as a sheet seen in Figure 1.4, under the assumption of the source being placed just above the surface and combining it with Equation 1.10, the upward second harmonic wave, and the reflected downward second harmonic wave from the surface [23, 27]. The expression for the reflected second harmonic field is

$$\begin{aligned} \frac{E^{(2\omega)}(\parallel, \parallel)}{E_p^2 A_p} &= a_{\parallel, \parallel} + c_{\parallel, \parallel}^{(3)} \cos(3\phi) \\ \frac{E^{(2\omega)}(\parallel, \perp)}{E_p^2 A_p} &= b_{\parallel, \perp}^{(3)} \sin(3\phi). \end{aligned} \quad (1.11)$$

Here  $(\parallel, \parallel)$  refers to p-polarized pump and p-polarized second harmonic and  $(\parallel, \perp)$  refers to p-polarized pump and s-polarized second harmonic. Focusing on the tensor elements,  $a_{(\parallel, \parallel)}$  is dependant on  $d_{33}$ ,  $d_{31}$  and  $d_{15}$  while  $c_{(\parallel, \parallel)}^{(3)}$  and  $b_{(\parallel, \perp)}^{(3)}$  only depend on  $d_{11}$ . [23] As mentioned earlier linking  $d_{11}$  to the anisotropy, the SHG signal should not change with the azimuthal angle if the surface and bulk are isotropic. Another important aspect is whether the bulk or the surface contributes most to the second harmonic signal. Guyot-Sionnest et al. [28] have found a relation saying the surface to bulk ratio is always larger than the  $\epsilon - 1$  thus a material with a high refractive index, such as metals and semiconductors, are preferable for probing the surface. Sipe et al. [23] also reported an isotropic bulk would not produce any s-polarized output, thus looking at the s-polarized signal would be usable for probing anisotropy in the surface. Tom et al. [29] comes to the same conclusion that no s-polarized SHG will be generated for an isotropic medium by

pure s- or p-polarized fundamental beam.

Both bulk Ag and Al have an FCC structure and are centrosymmetric [30] thus no bulk SHG signal is expected. As the Ag layer grows, less signal is generated from the substrate surface and instead signal comes purely from the surface of the thin film. Though an important thing to note is the difficulty in predicting the surface symmetry of the Ag thin film, as it is heavily influenced by deposition parameters as well as the surface structure of which the thin film is grown upon. The surface structure could be determined from other experiments afterward. Che et al. [31] have investigated the reflected SHG intensity as a function of the incident power of the laser beam for different metal films at a thickness of around 100 nm. Most of the metal films showed the same quadratic tendency of higher intensity with larger power with specifically Ag, Al and Au showing very similar tendencies for both 100 and 50 nm film thickness.

## 1.2.2 Phase Matching

When working with SHG from non-centrosymmetric materials (eg. AlN), especially when looking at the signal generated through a crystal, phase matching is an important parameter. The effect of phase matching on the second harmonic signal intensity can be seen in Figure 1.5.

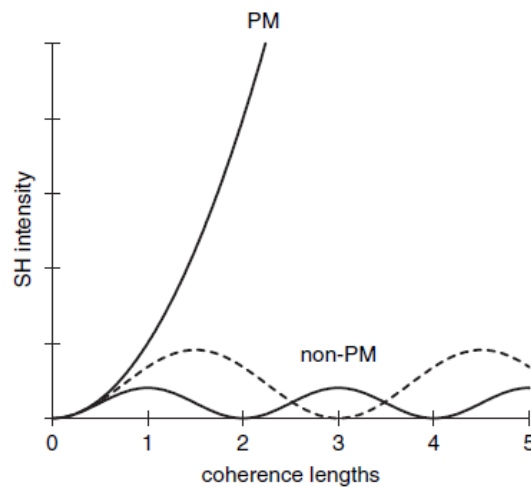


**Figure 1.5:** The second harmonic intensity through a crystal under phase matched conditions and non-phase matched conditions.  $\Delta k_{PM} < \Delta k_{Dashed} < \Delta k_{non-PM} < .$  [6]

If there is a phase mismatch between the fundamental and the second harmonic wave, they can create destructive interference. The reason for phase mismatching is rather simple if comparing the phase velocity: The fundamental field propagates as  $c/n(\omega)$  and the second harmonic field propagates as  $c/n(2\omega)$ . Thus the different

velocities will put them out of phase unless the distance is very short. [4, 6, 22] In order to achieve phase matching  $\Delta k = 2k_1 - k_2 = 0$ , with indices 1 and 2 being linked to the fundamental and second harmonic wave respectively. This can only hold true if  $n_1(\omega) = n_2(2\omega)$ , but due to dispersion in the material, this will almost never be the case. As mentioned earlier this mismatch is also dependant on the length of the propagation and the severity can be quantified through the nonlinear coherence length, which is shown to be [6, 32]

$$L_{coh} = \frac{\pi}{|\Delta k|} = \frac{\lambda}{4|n_2 - n_1|}. \quad (1.12)$$

For optical materials, the coherence length has been shown to be on the scale of a few tens of microns, after which the SHG process will go in reverse. [6] Since thin films often are thinner than ten microns, the problem is not as severe, compared to generating second harmonic waves by transmission of a fundamental wave through a crystal. In all cases, interference between waves will happen, since there will be reflections between each layer similar to linear optics. [33]

### 1.3 Aluminum Nitride

AlN coatings are of great interest due to the wide bandgap at 6.2 eV ( $\approx 200$  nm) thus making it transparent at many wavelengths including UV, which is utilized in optical devices. AlN is also of interest due to the low difficulty in making high-quality films through PVD and its piezoelectric behavior. AlN has also found interest in the field of protective coatings with high thermal conductivity and good resistance against oxidation [34, 35]. AlN has a melting point higher than 2000 °C [36] and in crystalline form, the melting temperature of AlN at nitrogen pressure of 100 atm was found to be around 2800 °C [37]. In the case of this study, the wide bandgap at a relatively low wavelength (compared to Si) makes it great for SHG studies. [38, 39, 40]

Looking at the bulk symmetry of AlN it exhibits a wurtzite structure (w-AlN) with a 6mm ( $C_{6v}$ ) hexagonal close-packed symmetry. [40] AlN bulk is non-centrosymmetric, which follows that the entirety of the film would contribute to the second harmonic signal. The signal is expected to be much larger than for Ag and Al, and grow quadratic with film thickness up to a certain thickness, as phase matching will pose a problem for thick films. Theoretically, the second harmonic polarization for the AlN film would be

$$\mathbf{P}_{pp}^{(2)}(2\omega) = 2(2d_{15}\cos(\theta)\sin(\theta) + d_{33}\sin^2(\theta) + d_{31}\cos^2(\theta))E_0^2. \quad (1.13)$$

This is based on the same calculations mentioned in Section 1.2.1, and taking the polarization of light into consideration, with the only non-zero tensor elements

being  $d_{15}$ ,  $d_{33}$ , and  $d_{31}$  and  $\theta$  being the incident angle. [38] If KSC is applied, this can be further reduced to

$$\mathbf{P}_{pp}^{(2)}(2\omega) = 2(3d_{15}\cos^2(\theta)\sin(\theta) + d_{33}\sin^3(\theta))E_0^2. \quad (1.14)$$

The calculations for Equation 1.14 can be seen in Appendix D. Looking at Equation 1.14, it is evident that in the scenario KSC applies, almost no signal will be generated from a small incident angle. Based on other works an incident angle of  $\sim 50\text{-}60^\circ$  should yield the maximum signal [39, 41].

Important to note that these elements are not of the same value as the previous tensor elements described for Si. Theoretically no s-polarized signal should be generated from p-polarized fundamental beam ( $\mathbf{P}_{ps}^{(2)}(2\omega) = 0$ ). When growing AlN epitaxially on Si(111) at room temperature it is also possible for the first couple of layers to grow in a zinc-blende structure (z-AlN) as this has same symmetry point group as the Si(111) surface and a better lattice match. [42]

## 1.4 Surface of Substrate

The focus of this reported is the reflected second harmonic signal generated from a surface and the deposited thin film layer upon it. So far a lot of attention has been put into explaining SHG from surfaces and thin films, but not as much on the surface itself and why it is important. The chosen substrate in this report is a Si(111) substrate. When the substrate is cut from the bulk a surface is created with dangling bonds which does not have the benefit of the equilibrium within the bulk and thus needs some sort of a reconstruction to counteract the lack of it. Initially the Si(111) when cleaved at low temperatures in ultra high vacuum (UHV) would create a  $2 \times 1$  reconstruction and during heating above  $\sim 275^\circ\text{C}$  begin transforming to a  $7 \times 7$  reconstruction which is more stable. [43, 1] This transition can be probed by SHG as shown by Heinz et al. [43] as they heated a Si(111) sample from  $20^\circ\text{C}$  to  $600^\circ\text{C}$ .

Another benefit of heating the substrate surface is the removal of the native oxide layer. Unless the cleavage was performed in high vacuum a native oxide layer will almost always be present. Within 10 minutes from cleavage, a couple of Angstrom thick oxide layer will be present in ambient pressure at room temperature. When growing a film epitaxially or using a low flux PVD technique, the atoms will arrange after the topmost layer, which would be the undefined amorphous native oxide layer and thus creating low quality films. [44] Studies have shown that heating silicon in UHV up to  $1200^\circ\text{C}$  for a minute is enough to remove the native oxide layer [45, 46, 47]. Reider et al. [48] used a temperature of  $1030^\circ\text{C}$

to remove the native oxide layer in UHV from a Si(111) surface.

Another method for creating clean well-defined substrate surfaces is through hydrogen termination. The principle is using hydrofluoric acid (HF) to remove the native oxide layer and hydrogen terminate the Si surface. [49] Though it would not prevent a native oxide layer growing on the substrate in ambient conditions over time, it can protect the substrate for a duration around 20 minutes. A big advantage of using hydrogen termination is that it can be removed at much lower temperatures compared to the oxide layer. The temperature for removal of the hydrogen termination in UHV is 800 °C [50]. Reider et al. [48] measured the desorption kinetics of hydrogen on a Si(111)  $7 \times 7$  surface in UHV. A hydrogen layer of 0.08 monolayers (ML) was removed after roughly 7 minutes at 520 °C. The hydrogen showed to affect the SH intensity at even small amounts, a coverage of 0.3 ML is enough to decrease the intensity by a factor of 100.

Thin film growth is dependant on several factors such as deposition rate, method, substrate temperature, pressure, surface energy, and lattice mismatch. When working with epitaxial growth at room temperature, often the lattice mismatch is the biggest factor in determining the outcome. Ag and Si does not have a great lattice match, thus island growth is expected. Epitaxial growth of Ag on Si(111)  $7 \times 7$  at room temperature has shown to grow in Stranski-Krastanov growth mode [51, 52]. This growth mode is defined by a very thin layer growth for the first couple of layers and then starting to grow 2D islands on top. [1]

## 1.5 Low Energy Electron Diffraction

Low energy electron diffraction (LEED) is a characterization method developed in the 1970s to analyze diffraction patterns from crystalline surfaces. LEED is often run at energies around 20 to 500 eV and thus is very sensitive to diffraction of the surface, thereby making it prominent in characterizing the topmost layers of a surface. UHV and a clean surface is required for LEED, as the tiniest contaminants on the surface or general obstacles in the mean free path will have an impact on the measurements. [25, 30, 53]

The working principle of LEED consists of an electron gun shooting electrons at a surface and the reflected diffraction pattern becomes visible on a fluorescent screen, a schematic can be seen in Figure 1.6.

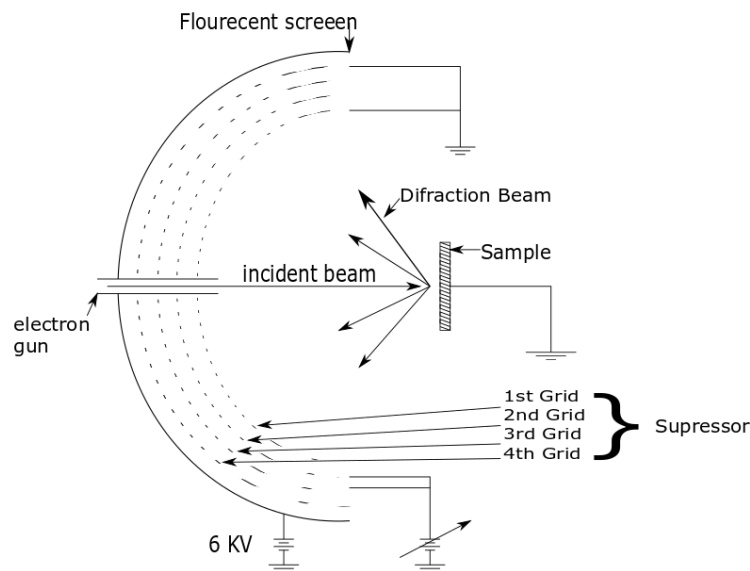


Figure 1.6: Schematic of a classic LEED setup. [53]

The pattern will often be seen as green spots and is known as LEED spots or LEED pattern. These spots are the product of constructive interference. The condition for constructive interference is [25, 30, 53]

$$k - k' = \Delta k = G. \quad (1.15)$$

Here  $k$  is the wavevector for the incoming electrons,  $k'$  is the reflected wave vector,  $\Delta k$  is the scattering vector and  $G$  is the reciprocal lattice vector. [25, 30, 53] A way to visualize the pattern from constructive inference occurring after diffraction is the Ewald's sphere. When the difference in wavevectors equals the recipro-

cal lattice vector and lands on the circumference of the sphere, a spot will appear, this is illustrated in Figure 1.7.

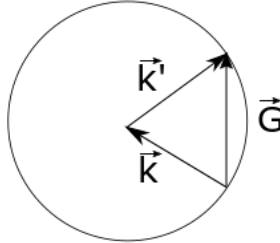


Figure 1.7: Illustration of the Ewald's Sphere

The number of spots on the pattern is increased when increasing the radius of the sphere, as it would intersect the circumference in more points. The sphere is made from the length of the wavevectors, thus the size of the sphere is dependant on the wavelength, as the length of the wavevector is inversely proportional with the wavelength as shown in Equation 1.16: [25, 30, 53]

$$|\mathbf{k}| = \frac{2\pi}{\lambda}. \quad (1.16)$$

When working with LEED, in order to get more fluorescent spots, the energy of the electrons is often increased. This due to the energy being inversely proportional to the wavelength, making it directly proportional to the length of the wavevector. The relation between the photon energy and the wavelength is given by 1.17 [25, 30, 53]

$$E = \frac{hc}{\lambda}. \quad (1.17)$$

## 1.6 Optical Parametric Oscillator

Due to the nature of a laser, creating tunable coherent radiation have been a problem for a long time. A solution seems to have been found by replacing the amplifying medium in a traditional laser by a nonlinear crystal, thus having an optical parametric amplifier in the optical cavity. This method is known as an optical parametric oscillator (OPO), a schematic can be seen in Figure 1.8. [6, 22, 54] Optical parametric amplification comes from the difference frequency process in which a pump beam at frequency  $\omega_3$  is being split when traversing a nonlinear crystal

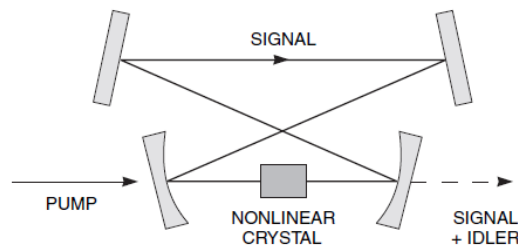


Figure 1.8: Schematic diagram of an optical parametric oscillator [6].

into two beams with frequency  $\omega_1 = \omega_3 - \omega_2$  and  $\omega_2$ , called *signal* and *idler* respectively, where the wave with the highest frequency of the two is referred to as the signal. The name optical parametric amplifier stems from the  $\omega_1$  field being amplified by difference frequency generation which is a parametric process. [4, 6, 22, 54, 55]

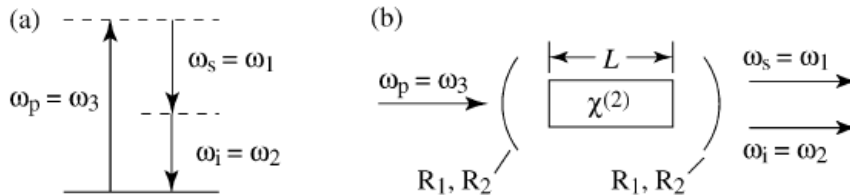


Figure 1.9: a) Relationship between difference frequency generation and optical parametric amplification. b) The gain of optical parametric amplification, which is used to make OPO. [4]

Figure 1.9 shows how the pump beam  $\omega_p$  is being split into signal  $\omega_s$  and idler  $\omega_i$  and how  $\omega_s$  is being amplified.  $R_1$  and  $R_2$  are reflectors and  $L$  is the length of the optical cavity. [4, 6, 22, 54] Adjusting the wavelength is done by rotating the crystal. [6, 22, 54, 55] When utilizing a OPO, loss in the average output power is expected, compared to the pump laser. [22]



# Chapter 2

## Method

### 2.1 Vacuum and Film Deposition

#### 2.1.1 Setup Overview

The setup utilized in the first experiments can be seen in Figure 2.1 and will be referred to as the Ag setup. The setup consists of different elements, some being different types of vacuum pumps to achieve the desired vacuum level, see Section 2.1.3. The setup also includes a sample holder. This sample holder allows for control of the sample position and orientation in the chamber. It also provides an option to thermally anneal the sample, through Joule heating, while mounted in the chamber. This allows for cleaning of the sample both prior and after deposition, by removing the initial oxide layer, diffusing the Ag into the silicon or resputtering of the deposited Ag.

A Q-pod quartz crystal is mounted on the sample holder in order to monitor the evaporation rate of the material described in Section 2.1.4. Furthermore, a thermal evaporation PVD setup is mounted to the chamber to evaporate Ag onto the substrate, described in Section 2.1.4. A Mass spectrometer is coupled to the chamber to help identify the presence of leaks during the different pumping steps and was further utilized to find the origins of the leaks, which will be described in Section 2.1.6. A LEED setup is mounted on the side of the chamber to make measurements on the samples crystalline surface structure before and after deposition, as described in section 1.5. Finally, different gauges were used to measure the pressure at different levels, described further in Section 2.1.5.

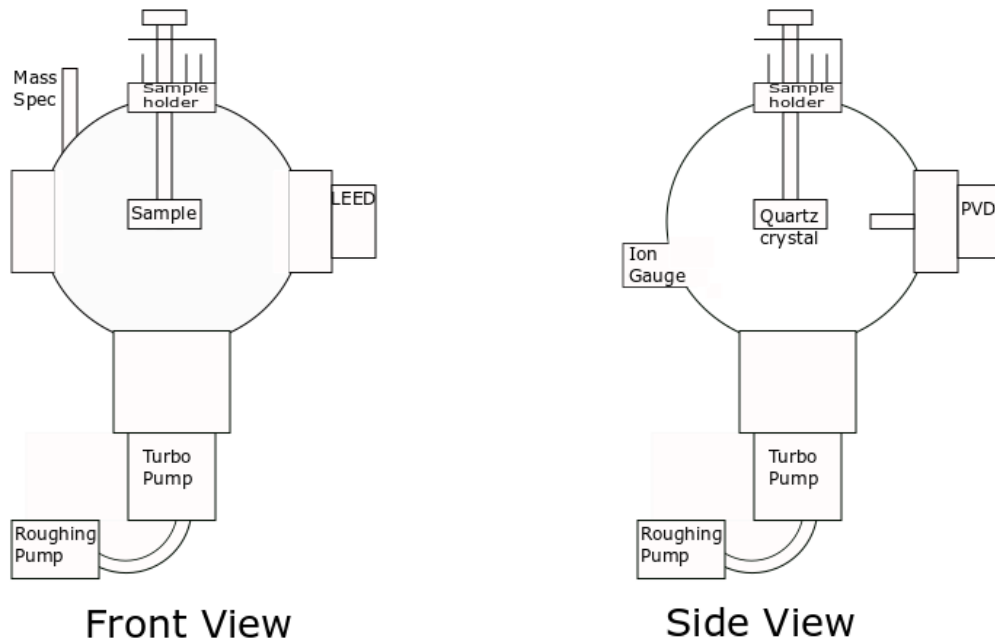


**Figure 2.1:** An overview of the vacuum chamber with a visualization of the different components utilized and their placements in correlation to each other.

### 2.1.2 Substrate Preparation

- Elma S 30 H Elmasonic
- DAD321 Disco Automatic Dicing Saw

Before each experiment the Si substrate was treated and prepared. The Si(111) wafer used in this project was a 1-mm-thick *n*-type wafer with a resistivity of 5  $\Omega$ -cm. The Si(111) wafer was cut into smaller pieces measuring 30x10 mm using the Dicing Saw. Afterwards, each sample was cleaned in an ultra sonic bath, first 2 minutes in acetone, then 2 minutes in demineralised water, and finally 2 minutes in ethanol followed by blow drying using a nitrogen gun. Substrates used in the AlN setup undergoes one more treatment, where the Si(111) substrates were emerged in HF to remove the oxide layer and hydrogen terminate the surface. After the substrates were mounted in the chamber, either in the Ag or AlN setup, the surface layer was removed through thermal annealing. In the Ag setup, 12 A was passed through the substrate for 20 seconds and in the AlN setup the sample holder was heated to 1100 °C. Correlation between the temperature and current for the Ag setup can be seen in Appendix A.

### 2.1.3 Vacuum Generation

- Roughing pump (achieving medium vacuum)
- Turbomolecular pump (going from medium to high vacuum)
- Baking of the vacuum chamber (to release gasses)
- Ion pump (to reach ultra-high vacuum)
- Titanium sublimation pump (this decreases the pressure with roughly a magnitude of order to end up in the  $10^{-10}$  mbar range)

Vacuum lowers the rate at which a contamination layer forms on the surface from unwanted sources such as oxygen. At atmospheric pressure, it takes  $10^{-6}$  seconds to form a monolayer of foreign material compared to  $10^4$  seconds at a pressure of  $10^{-10}$  mbar. [3, 56, 57] Another factor benefiting from a high vacuum was the LEED equipment, as UHV was necessary in order to give proper measurements. LEED requires a high mean free path to avoid changes in the trajectory of the electrons towards the sample, as mentioned in Section 1.5.

To achieve vacuum in the high to ultra-high region for the Ag setup, a few different methods were taken into use. To go from atmospheric pressure to the medium vacuum range ( $10^{-3}$  mbar) a roughing pump was utilized. Figure 2.2 illustrates a roughing pump, to show its working principle. First, a vacuum is created on the side connected to the chamber by expanding the volume, this leads to a pressure difference that draws air into the pump. Then by decreasing the volume near the exhaust, the pressure builds up and the gasses are forced into the atmosphere. [3, 56, 57]

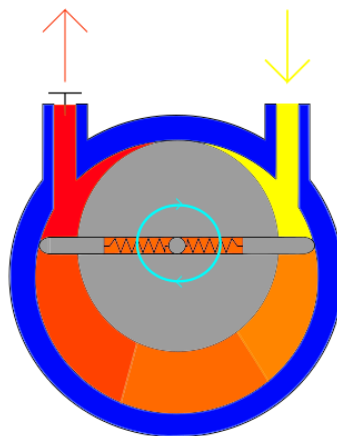


**Figure 2.2:** A schematic showing the working principals of a roughing pump.

After a medium vacuum was achieved using a roughing pump, a turbomolecular pump, often called a turbo pump, was utilized to achieve high vacuum. Figure 2.3 shows an illustration of a turbo pump, where two different kinds of blades can be seen, rotary blades and stationary blades. Both sets of blades are tilted in such a way that incoming molecules are forced away from the chamber. The rotary blades add energy to the molecules, forcing them further down the pump. [3, 56, 57] Turbo pumps are always used in series with a roughing pump. This is because a turbo pump works as a compressor and as a consequence, the pressure difference between the chamber and the bottom of the pump can't exceed beyond a certain value. This means a roughing pump is used to pump the backside of the turbo to reduce the pressure difference. [3, 56, 57]

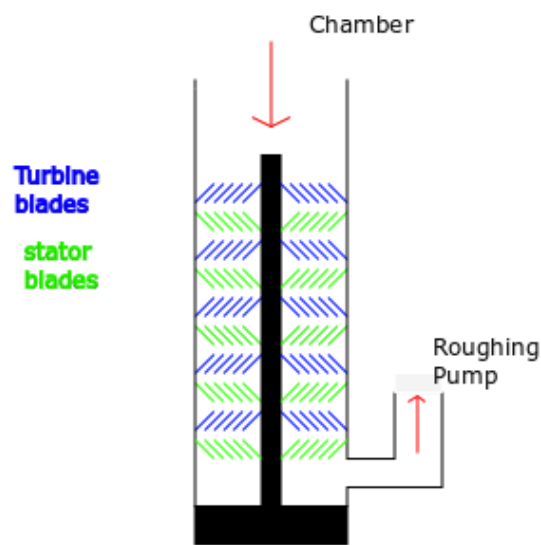


**Figure 2.3:** A schematic showing the working principals of a turbomolecular pump.

The chamber was then baked at 170 °C to further reduce the pressure. Baking releases molecules bound to the surface of the chamber, where normally this would be released slowly and thus putting a lower limit on the vacuum. By heating the chamber, energy is transferred to the molecules trapped in the wall thus releasing them quicker. Furthermore, the water that entered the chamber through the air, gets split into oxygen and hydrogen, which can then be pumped through the turbo. [56, 57]

An ion pump was utilized to reach UHV. A schematic of an ion pump can be seen in figure 2.4. The working principle of an ion pump lays in its ability to ionize molecules and atoms. This ionization leads to positively charged molecules, that is accelerated into a solid electrode where they are either buried or sputter material to the walls of the chamber. Electrons generated are trapped in the magnetic field,

thus ionizing more incoming gas. An ion pump can only be utilized at high vacuum due to the possibility of overloading the pump with too many ionized atoms. [3, 56, 57]

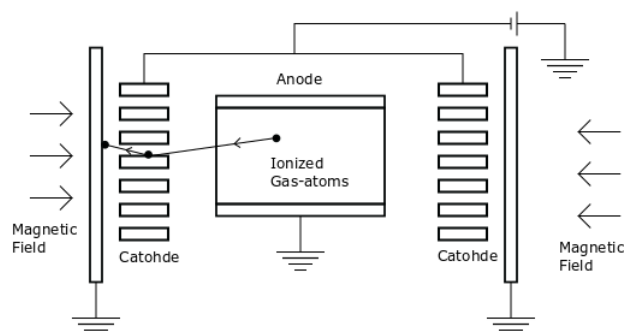


**Figure 2.4:** A schematic showing the working principals of a ion pump.

Lastly, a titanium sublimation pump (TSP) was used. TSP consists of a filament made from titanium where a current is passed through. This causes the titanium to evaporate and create a thin film of titanium on the inner walls of the pump walls. As the residual gas in the chamber comes into contact with the titanium coated walls, it will react and form a stable solid material, thus reducing the pressure with up to an order of magnitude. The titanium film will at some point be saturated and a new layer has to be created to keep the low pressure. [3, 56, 57] At the pressure level of using the TSP, the turbo was closed off as the chamber pressure was below the working range of the turbo pump.

#### 2.1.4 Thermal Evaporation

- Pure Ag
- Pyrolytic boron nitride (PBN) crucible
- Tungsten coil
- Water cooling
- Chimney add-on (Used to focus the evaporated Ag)

A schematic of the evaporator used during the experiments in the Ag setup can be seen in Figure 2.5. The setup utilizes Joule heating from a tungsten wire wrapped around a ceramic crucible made of pyrolytic boron nitride (PBN). A water cooling system was used in conjunction with the evaporation system. This both cools the evaporation setup and shields the chamber from heating. A chimney

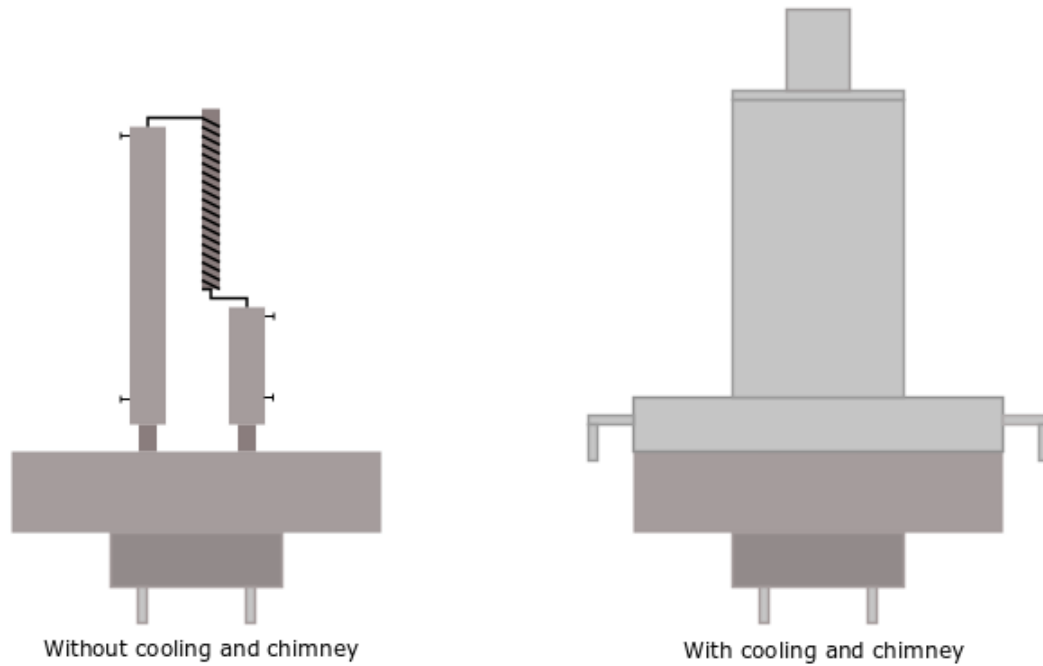


**Figure 2.5:** a) a visualization of the evaporator used during the experiments with and without a the chimney.

was used to reduce the spread of the evaporated material, to avoid damaging the different components present in the chamber.

To measure the flux of the incoming evaporated material, a Q-pod quartz crystal was utilized. This piezoelectric crystal vibrates at a specific frequency and sends out a corresponding signal. The frequency decreases as mass is added to the crystal which the Q-pod software uses to calculate the flux of the incoming material. [3]

### 2.1.5 Vacuum Measurement

- Pirani gauge (to measure the pressure in the medium to high vacuum range)
- Hot-filament ionization gauge (measuring pressure from high vacuum to ultra-high vacuum)
- Mass spectrometer (Used for leak checking often in conjunction with helium)

Two types of gauges were utilized, each with a specific pressure range where it functions most optimally. First, a pirani gauge was used for measuring the pressure in correlation with the roughing pump. The pirani gauge was placed on the backside of the turbo pump and was first used to measure the pressure in the

chamber before the turbo pump was turned on. Later it was used to measure the backside of the turbo pump. A pirani gauge consists of a metal wire exposed to the environment where the pressure was being measured. The wire is heated by a current flowing through it, by Joule heating, and cooled by collision with the gas molecules surrounding it. If the pressure of the surrounding gases is reduced, the cooling of the wire will decrease, thus increasing the temperature. [3, 56, 57] When the temperature of a system changes, so does the resistance, so by measuring the voltage and current across the wire, a change in resistance can be measured, and from there the temperature and the pressure can be determined. [3, 56, 57]

The second kind of gauge was a hot-filament ionization gauge, which was utilized in the high to ultra-high vacuum range. This gauge functions by ionizing gas present within its confinement. The electrons are generated from a heated filament, which can collide with the gas present and ionizing a fraction of the gas. Finally, the ionized gas is attracted to a collector, where it emits an ion current that can be measured. [56, 57]

The ion current measured depends on the type of gas. This means that hot-filament ionization gauge is dependant on the composition of the gases in the chamber. However, if the composition of the chamber stays constant, the ion current measured would be proportional to the density of molecules in the chamber and thus proportional to the pressure. [56, 57]

### 2.1.6 Mass Spectrometer

A mass spectrometer was used in two different ways. First and foremost it was used to see the effectiveness of both the pumping and baking of the chamber, as the measured amount of oxygen and nitrogen should fall during pumping and the amount of water should fall after baking. The second use was leak checking by applying helium directly to the different joints in the chamber, to see if it leads to a spike in helium measured.

The mass spectrometer utilized in the setup was a quadrupole mass analyser (QMS) utilizing electron ionization (EI). As the name implies EI functions by bombarding the gas present within the confine of the mass spectrometer with electrons in order to ionize it. These charged gases are then accelerated towards a collector by the quadrupole. The quadrupole bends the trajectory of the ions depending on their mass-to-charge ratio, where ions with the same ratio will undergo the same amount of deflection. The signal is then plotted as a function of the ion current signal strength to mass-to-charge ratio. Different atoms can then be identified by correlating this to the know atomic mass. [57]

## 2.2 Optical Setup

- Q-switched Nd:YAG nanosecond pulse laser (Schematic can be seen in Figure 2.6)
- Optical parametric oscillator
- Quartz crystal for reference
- High pass filter (RG 715)
- Low pass filter (C3C23)
- Photomultiplier tube
- Boxcar integrator

### 2.2.1 Laser

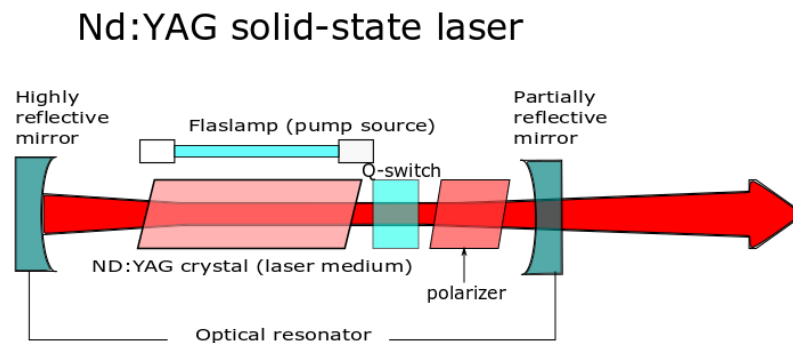


**Figure 2.6:** Schematic of Nd:YAG laser setup.

The primary laser used in this report was a Q-switched Nd:YAG nanosecond pulse laser. Able to generate pulses of 6 ns, working at a frequency of 10 Hz, a wavelength around 1064 nm, and an effective power of 10 mW after the OPO. The laser is a solid-state laser using a neodymium-doped yttrium aluminum garnet crystal as the laser medium. [58, 55] Q-switching is a method in which the Q-factor is purposely lowered to build up energy. The Q-factor stands for quality factor and describes the loss in energy relative to the optical resonator, as seen in Figure 2.6. While the Q-switch is active, energy will build up until it reaches saturation and the Q-switch changes to high Q-factor, thus letting out a pulse. The Q-switch used in this report is an electro-optic crystal that opens with a high voltage. The electro-optic crystal utilizes what is known as Pockels Effect, which means the refractive index of the crystal can be modified in proportion to applied the electric field strength, effectively working as a waveplate. The crystal together

with a polarizer, as seen in Figure 2.6 can create pulses in the nanosecond range, by using the electro-optic crystal to rotate the polarization.

### 2.2.2 Azimuthal Setup

An azimuthal setup was implemented in order to measure the reflected second harmonic signal from different rotational angles of the Si(111) surface. The sample holder is rotating clockwise during the measurements. The incident light is hitting the Si wafer at an angle of  $45^\circ$  in atmospheric conditions. A schematic of the azimuthal setup can be seen in Figure 2.7.

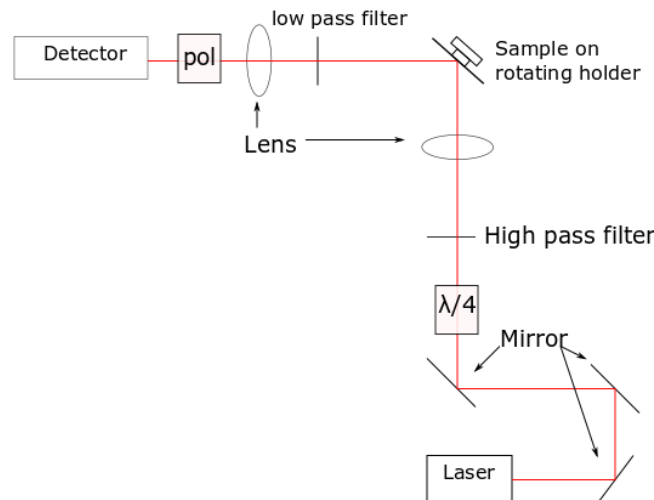


Figure 2.7: Schematic of the azimuthal setup.

### 2.2.3 Linear setup

- JDS Uniphase 1125P Helium Neon Laser
- Thorlabs PDA100A-EC Si Amplified Detector
- Chopper

Linear reflection measurements were carried out in the AIN setup to distinguish between the deposition of Al and AlN by measuring the reflected light. The laser is running at 633 nm wavelength and with a power of 10 mW. Here a chopper was utilized to make a reference to determine the amount of reflected light from the surface. Al deposition on a Si surface will increase the amount of reflected light, where the deposition of AlN will decrease the amount of reflected light, due to the difference in refractive index.

### 2.2.4 Second Harmonic Setup

Figure 2.8 shows the Nd:YAG laser and lens setup used for measuring the reflected SHG signal in the Ag setup. An OPO was then added in continuation of the laser to control the wavelength of the outgoing pulse. Then a high pass filter was set in front of the beam to sort out leakages from the OPO.

From here the beam can be send in two directions, through and around the vacuum chamber. This was done by having two sliding mirrors that can direct the light around the chamber. Both paths utilize lenses to focus the beam. the beam going through the chamber has two lenses, one to focus the beam onto the sample at an incident angle of  $60^\circ$  and one to focus the beam onto the detector. The other path has one to focus onto a wedge formed quartz crystal and the other to focus onto the detector.

The reason for the two paths the laser can travel was to be able to create a reference of the intensity of the incoming wave as the different wavelengths created by the OPO has varying intensities.

Both of these beams go through a low pass filter that removes the wavelength originating from the laser. The quartz wedge was used as a reference for the SHG, as the response is constant in the wavelength range. The wedge form of the reference was to ensure only front reflection would be directed towards the next mirror in order to remove bulk contribution and avoid interference with the back reflection. Then a polarizer was used to allow for observation of either p- or s-polarized light. Finally, the light traveled to a detector, which will be explained below.

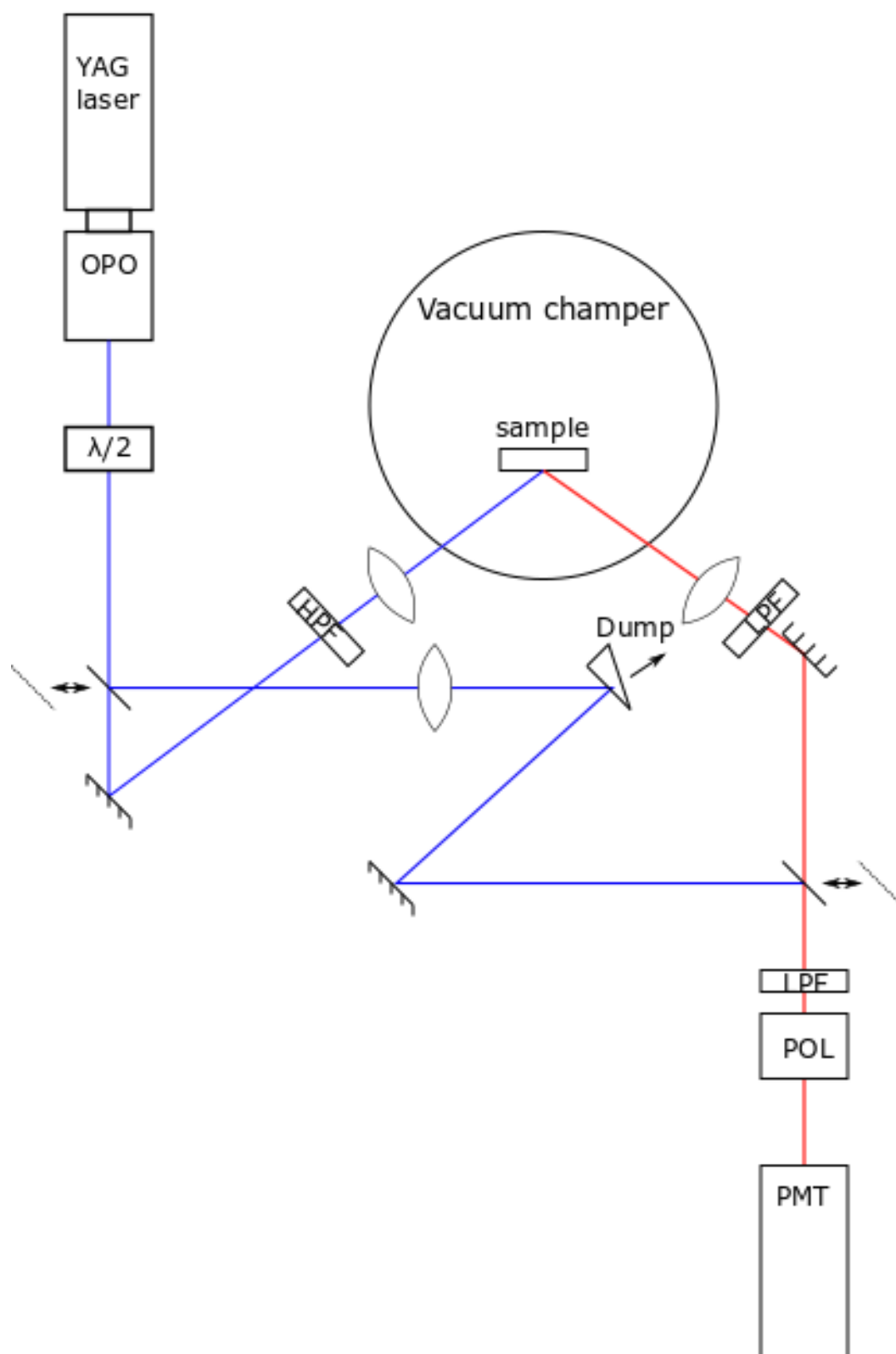


Figure 2.8: The laser setup used during the experiments.

### 2.2.5 Detector

The detection method used was composed of two parts, a photomultiplier tube (PMT) to amplify the signal and a boxcar integrator in order to align the measured signal with the pulse for improvement of the signal to noise ratio.

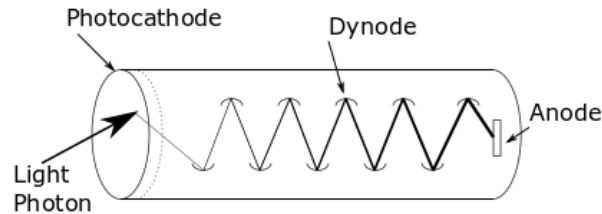


Figure 2.9: Schematic of the working principle of a PMT.

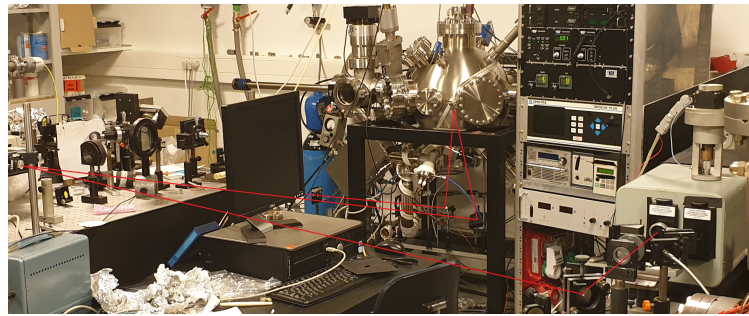
A PMT is a tube consisting of a photocathode, several dynodes with subsequently larger positive potentials, and an anode, as seen in Figure 2.9. When the light is incident on the photocathode an electron is ejected, accelerated in the potential, and hits the first dynode which ejects more electrons, effectively multiplying the number of electrons. The dynodes are angled so the electrons will keep hitting the next dynode, further multiplying the number of electrons, until hitting the anode at the end of the tube, creating a measurable signal in the form a sharp current pulse. [59] For most experiments in this project the PMT was operated at 1900 V.

The signal was then processed by a boxcar integrator, which integrates the input signal after a delay, over a specified time. This was done in order to decrease the impact of noise, as a large part of the incoming signal could be noise. This method is viable as the signal is pulsed and thus possible to predict the delay needed for measuring only the relevant signal. [60]

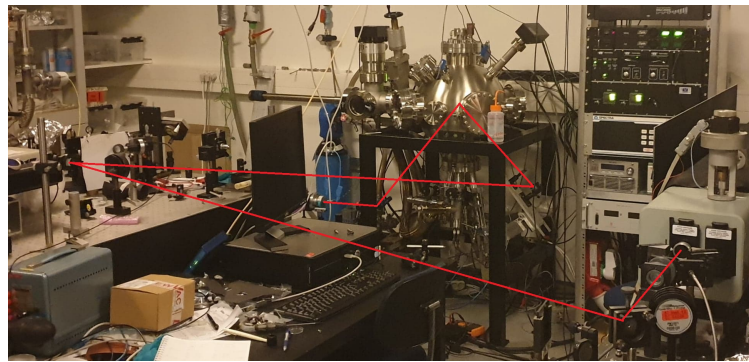
Due to the increased repetition rate for the Sapphire laser, being 80 MHz compared to the 10 Hz of the Nd:YAG, another detection method was needed instead of the Boxcar. PMT is able to detect individual photons and can thus be operated in photon counting mode. Compared to the averager technique utilized by the boxcar integrator, photon counting is more sensitive and can detect weaker signals. The PMT cannot remove background noise and would need a lock-in module to measure the signal with and without the laser on. Another downside is two photons can be counted as one, if two pulses arrive at the anode too closely in time, which can happen if working above 100 MHz repetition rate. Photon counting also requires a certain amount of signal pr time, thus putting some restrictions on the laser. Thus photon counting is not favorable when detecting at a repetition rate below MHz. The main problem with using boxcar at higher repetition rates (above

100 kHz) is the electronics will not be able to keep up with the laser. In conclusion, photon counting is often used for high repetition rate lasers and boxcar is used for low repetition rate. [59]

### 2.3 AlN Setup



(a)



(b)

**Figure 2.10:** a) Image of the first iteration of AlN chamber with the laser path drawn in. b) Image of the second iteration of AlN chamber with the laser path drawn in.

Other films of interest for this report are Al and AlN, which requires a different setup due to source limitations in the original setup. This setup will be referred to as the AlN setup. This setup utilizes a load lock, in order to reduce the amount of pumping needed each time the sample has to be changed, as such it only relies on a roughing pump and a turbo pump. When the Al source is changed, baking is used as well. The Al is thermally evaporated similar to the Ag. Both pirani and ionization gauges were used for pressure measurements.

Same laser and detection setup was used as mentioned previously. In Figure 2.10a an image of the setup with the laser path drawn in can be seen. Due to the physical placement of the AlN setup the incident polarization of the light will be a mix of p- and s-polarized light. The Al was thermally evaporated, similar to the Ag and

the atomic nitrogen for the AlN film comes from an RF source which cracks a nitrogen gas. Using RF to crack nitrogen gas can create  $N$ ,  $N_2$  and  $N^+$ , in which  $N$  is preferred to create nitride films [61]. In order to get the highest yield of atomic nitrogen a low gas flow (<2 sccm) and high RF power (300-450 W) are needed [62].

A big limitation of the AlN setup was the incident angle of the fundamental beam being almost parallel to the surface normal, which is not favorable when doing SHG on AlN. The chamber was considerably smaller, working at a base pressure of  $10^{-10}$  mbar. The load lock attached on the side was working at a base pressure of  $10^{-7}$  mbar.

A limitation of the AlN setup was that the substrate was not able to reach the same temperatures as the Ag setup. Thus the sample mounted was not able to reach the 1200 °C needed for removal of the native oxide layer and another method was needed. Hydrogen termination of the Si surface was done by using 7% HF for roughly two minutes to remove the native oxide layer and hydrogen terminate the surface, which can be removed at 800 °C, which should be obtainable by the sample mount.

A secondary iteration of the AlN setup was build as Seen in Figure 2.10b Here both the nitrogen and Al source has been moved to the bottom of the chamber to allow for a 45° incident angle of the fundamental beam trough side windows. The relocation of the Al and nitrogen sources to the bottom of the chamber increased the distance to the sample, thus giving a lower deposition rate.

## 2.4 Characterization

### 2.4.1 Atomic Force Microscopy

Atomic force microscopy (AFM) is a method often used for imaging static surfaces in the nanometer to micron scale. The working principle of the AFM is a tip on a cantilever moving in a raster pattern over a surface. A laser is directed at the back of the cantilever, reflecting back up at a detector, as the tip is moving over the surface the cantilever and surface will interact and thereby change the reflection of the beam, thus imaging the surface, a schematic can be seen in Figure 2.11. The AFM has different operating modes, for this project the tapping mode was utilized in which the cantilever was set into oscillation as it scans the surface, thereby tapping it. [63]

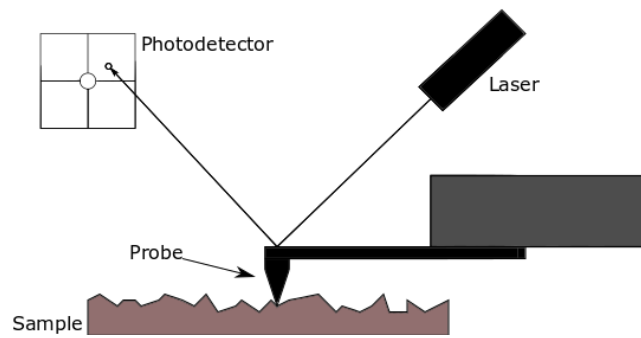


Figure 2.11: Working principle of an AFM.

### 2.4.2 Ellipsometry

Ellipsometry was utilized to measure the thickness and refractive index of the samples. The working principle of ellipsometry is measuring the change in polarization of the reflected light compared to the incident light on the sample. The data is then compared with a model in order to get the refractive index and film thickness. Often the reflected light becomes elliptical in polarization, thus the name ellipsometry. A schematic of an ellipsometer can be seen in Figure 2.12 also showing the elliptical polarization. A few restrictions in this method, which proves vital in the measurement, is keeping a low surface roughness to reduce scattering and have a thin enough film to ensure reflection from the substrate. Depending on the wavelength used, the ellipsometer is most reliable when the film is kept below a few microns in thickness, due to interference. [64]

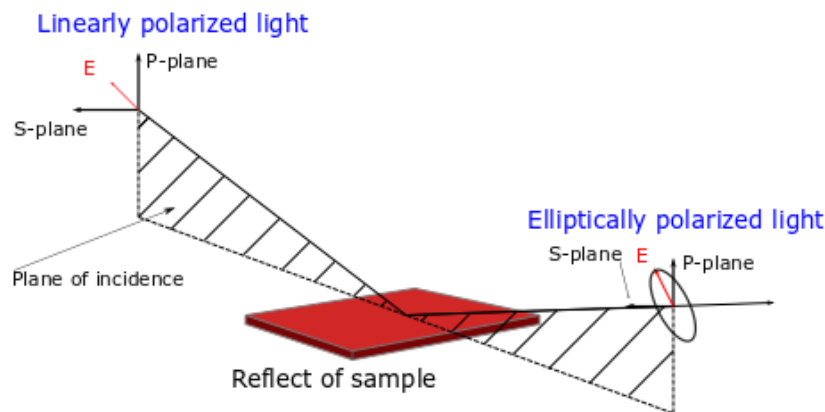


Figure 2.12: Schematic of an ellipsometer.

## **2.5 Software**

### **2.5.1 Gwyddion**

Images obtained by AFM were analyzed using the Gwyddion software. Gwyddion calculates the height, length, and typography of AFM images by utilizing the scale bar integrated into the image. This was then used to measure the thickness of the individual layers of the deposited thin film, and to estimate the size of the different crystalline domains, utilizing the built-in tools.

### **2.5.2 Matlab**

Matlab was used to create graphs and tables containing the data gathered from the above-mentioned methods. It was also used to make simple theoretical models to support the data collected.

### **2.5.3 OriginPro**

OriginPro software was used to analyze data and create most figures used throughout the project. Same purpose as Matlab but easier to use.

### **2.5.4 Inkscape**

Inkscape was used to make the illustrations through out the report. Inkscape is a sketching software with vector based schematics, which is preferable in order to avoid problem accruing in image quality.

### **2.5.5 Autodesk Inventor Professional 2019**

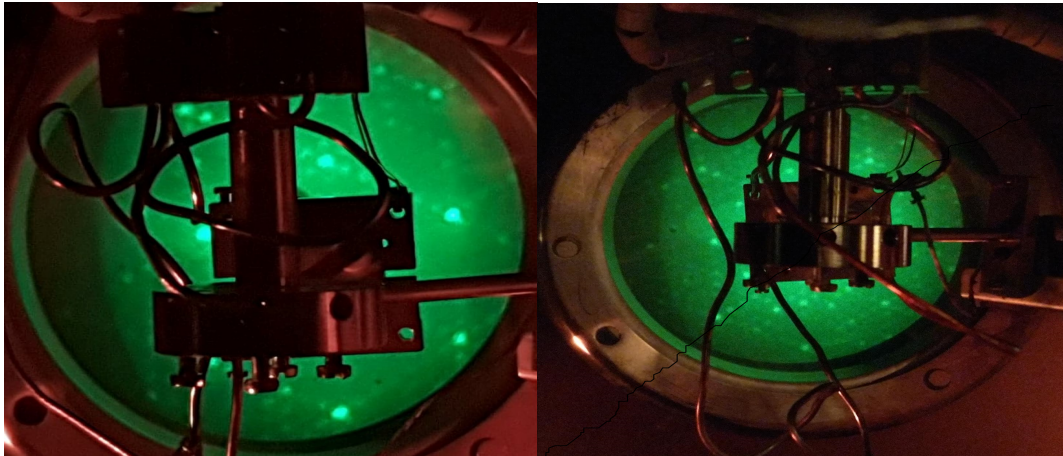
Inventor was used to make schematic drawings of the industrial setup. Inventor is a Computer-Aided Drawing (CAD) software, with a focus on creating precise solid parts in 3D, where each part fits together in the final assembly. As with Inkscape, Inventor uses vector-based graphics.

## Chapter 3

# Results and Discussion

The beam from the laser used in this report, described in section 2.2.1, is a p-polarized Nd:YAG Laser and when looking at either the p- or s-polarized signal it will be referred to as  $Pp$  and  $Ps$  respectively in order to clarify the polarization of the fundamental beam and the second harmonic signal.  $M$  and  $m$  is referring to a mixed polarization of fundamental and SH beam respectively. All spectra data presented in this report is made by averaging three consecutive measurements when possible.

### 3.1 Low Energy Electron Diffraction



(a)

(b)

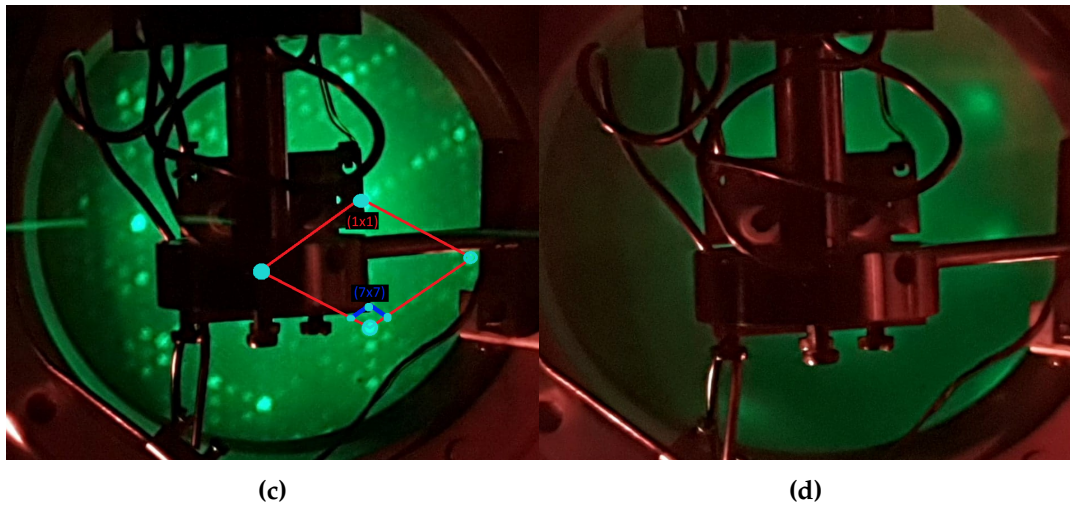


**Figure 3.1:** Images of the LEED pattern on a Si(111) surface a) After annealing at 12 A for 20 seconds prior to deposition showing a  $(7 \times 7)$  reconstruction (97 eV). b) After annealing at 4 A for 1 hour after deposition showing a  $6 \times 6$  reconstruction (75 eV). c) After annealing at 12 A for 20 seconds after deposition showing a  $(7 \times 7)$  reconstruction at (100 eV). d) Ag deposited on Si surface at (146 eV).

To carry out experiments focusing on SHG, a clean surface is needed to be certain that the signal originates from the Si surface and is not influenced by foreign elements or a native oxide layer. Cleaning was done by thermally annealing an Si substrate. The standard annealing process used in this project was increasing the current to 15 A for 2 seconds and then 12 A for 18 seconds. These currents correspond to a temperature measured on the Si surface of 1240 °C and 1164 °C respectively, as can be seen in Figure A.1 in the appendix. To estimate if the surface was clean, LEED was used.

As seen in Figure 3.1a a clear  $(7 \times 7)$  pattern is present on the Si surface before deposition of Ag. This pattern is recognizable as a hexagonal pattern with six smaller dots in between. When comparing Figure 3.1a with the findings of Saitoh et al. [65] showing a  $(7 \times 7)$  Reconstruction at 79 eV, a similar pattern can be seen. The similarity confirms the reconstruction of the sample in Figure 3.1a, where the only difference is the distance between individual dots. This is due to the difference in beam energy, as lower energy increases the distance between dots, as mentioned in Section 1.5.  $(7 \times 7)$  is the expected reconstruction of a Si surface, as it is the most stable [26, 66], thus giving the most replicable SHG measurements.

Figure 3.1d shows LEED measurements carried out on Ag deposited on a Si substrate. Here some vague dots can be seen in a hexagonal pattern, meaning that the Ag gradually extinguishes the  $(7 \times 7)$  signal leading to a  $(1 \times 1)$ , this is also observed by Saitoh et al. [65]. This indicates that Ag has been deposited on

the surface and the growth follows the underlying Si(111) structure at its current thickness.

Figure 3.1c shows the diffraction pattern after deposition and annealing. Here a  $(7 \times 7)$  pattern is observable, which indicates that annealing of the Si substrate is a reliable method for cleaning the sample after deposition. This is probably a combination of re-evaporation of the Ag from the sample, and diffusion of Ag into the Si, as even short annealing times should be sufficient in diffusing all the Ag [67]. If diffusion occurs during annealing, a saturation of the sample will eventually be reached. This means the sample is reusable a certain amount of times before the Si becomes over-saturated and Ag can no longer diffuse.

Figure 3.1b shows a different diffraction pattern than expected. Instead of a  $(7 \times 7)$  reconstruction a  $(6 \times 6)$  reconstruction is observed. This sample was annealed at 4 A, corresponding to a sample temperature around 872 °C as seen in appendix A, for an hour to clean it before experiments were carried out. The long annealing time could be the reason for the unexpected reconstruction pattern, as the constant heat could have destroyed the sample by removing some surface atoms. This would hinder the possibility for a  $(7 \times 7)$  reconstruction and another minimum energy configuration was created instead. Even though the temperature is enough for reconstruction, it is not enough to remove the native oxide layer, which might also explain the unexpected LEED pattern. This means the samples can be over annealed and the annealing time has to be taken into consideration to allow for repeatability of the experiments.

### 3.2 Azimuthal Angle Setup

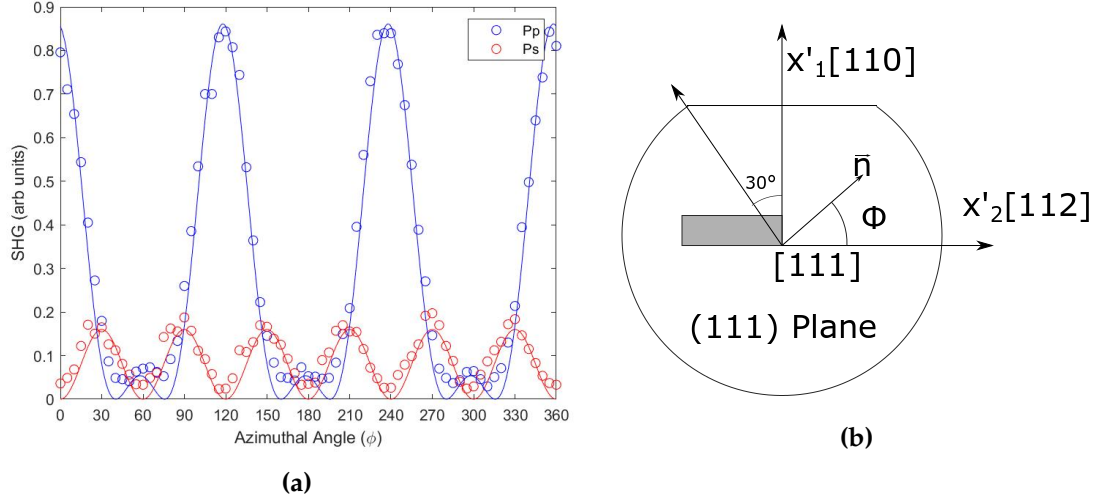


**Figure 3.2:** a) The second harmonic signal on a SiO<sub>2</sub> surface as a function of the azimuthal angle with  $\theta = 45^\circ$ . The circles are representing the measured data and the lines are model based on Equation 1.11. b) Illustration of the Si wafer at the starting angle with crystalline axis.

As mentioned in Section 1.2.1 it is seen that the SHG signal from a surface is very dependant on the surface symmetry. Due to the elongated shape of the substrates used, it is preferred to cut the Si Wafer in the angle yielding the largest possible signal for both  $Ps$  and  $Pp$ . To test this an experiment was carried out in which the Nd:YAG laser was set to a wavelength of 757 nm with an incident angle of  $45^\circ$  on a Si(111) wafer with a native oxide layer. The wafer was rotated clockwise around the surface normal during the experiment and a detector measuring the reflected  $Pp$  and  $Ps$  signals at different angles. This was done both to see how Equation 1.11 would fit and to find the right angle to cut out samples for mounting in the UHV system to secure both a  $Pp$  and a  $Ps$  signal. The experiments were conducted in free space.

Equation 1.11 shows the correlation between the orientation of a Si(111) surface and the SHG signal as found by Sipe et al. [23] This relation has been used to make a theoretical comparison to the experimental data, which can be seen in Figure 3.2a. It must be noted the values of the three constants  $a_{\parallel,\parallel}$ ,  $b_{(\parallel,\perp)}^{(3)}$  and  $c_{(\parallel,\parallel)}^{(3)}$  have been altered to fit the experimental data, but due to their complexity, will not be used further for determining other constants or relations. It can be seen the  $Ps$  signal fits well to the  $\sin(3\phi)$  with the sixfold symmetry as predicted and a maximum at  $30^\circ$  repeating every  $60^\circ$ . Looking at the  $Pp$  signal the six peaks are alternating more in intensity. This is due to the introduction of the isotropic contribution from the  $Pp$

signal as  $P_s$  only carries the contribution from the anisotropy. Tom et al. [29] have made similar experiments with similar results and the explanation for the missing peaks is an interference between the orientation-independent part of the isotropic term and the orientation-dependant part of the anisotropic term. The interference creates alternate increasing and decreasing peaks if the isotropic part ( $a_{\parallel,\parallel}$ ) had a similar amplitude to the anisotropic part ( $c_{(\parallel,\parallel)}^{(3)}$ ). This result is indeed obtained if  $a_{\parallel,\parallel} = -c_{(\parallel,\parallel)}^{(3)}$ . In the data presented in this report the amplitudes of the isotropic and anisotropic contributions are not exactly equal and thus three small intermediate peaks are observed for the  $Pp$  signal. The theoretical model is based on a Si(111) surface, while the experimental data is from a Si/SiO<sub>2</sub> interface cut from a Si(111) wafer. Though they still align pretty well in the azimuthal angle measurements and thus whether or not an oxide layer is present on the surface throughout the experiments will not be expected to have an impact on the orientation of the substrate in the sample holder.

Due to the anisotropic nature of the  $P_s$  signal and it being negligible in isotropic bulk [23], it is the preferred polarization for probing thin films and properties such as crystallinity, thus the largest  $P_s$  signal is preferred. It can be seen that the SHG signal strength for  $Pp$  and  $P_s$  are similar at the angles corresponding to the  $P_s$  peaks. This means the two different signals are comparable and that it would be possible to measure changes in both  $Pp$  and  $P_s$  at  $P_s$  peak azimuthal angles.

After these measurements, the following experiments will be carried out on substrates cut along the [112] direction corresponding to 90°, as shown in Figure 3.2b. This is due to the substrate being mounted vertically in the chamber. As it was shown that this orientation leads to a  $P_s$  peak and a  $Pp$  signal in the same range. As these experiments were made with a different incident angle and in free space with the native oxide layer, the signal values may be different when making the SHG experiments in the vacuum chamber. Figure 3.2b shows an illustration of a Si(111) wafer with the crystalline axis and the grey rectangle is the substrate and how it is cut.

### 3.3 Nonlinear Spectroscopy on Si

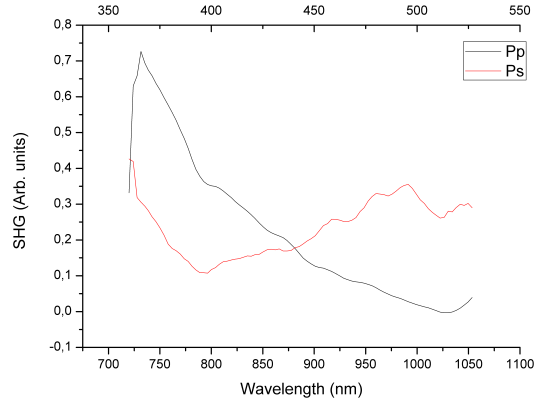


**Figure 3.3:** Spectra for the second harmonic signal intensity from 720 to 1050 nm wavelength with  $\theta = 60^\circ$  on Si for  $Pp$  and  $Ps$  polarization.

To see how the reflected second harmonic signal of the sample surface depends on the wavelength of the pulsed laser, different measurements were carried out and will be referred to as spectra measurements. All substrates used were Si(111) for both Ag, Al and AlN film growth. Due to Si being the substrate of choice for this project, it is important to examine in order to create a baseline.

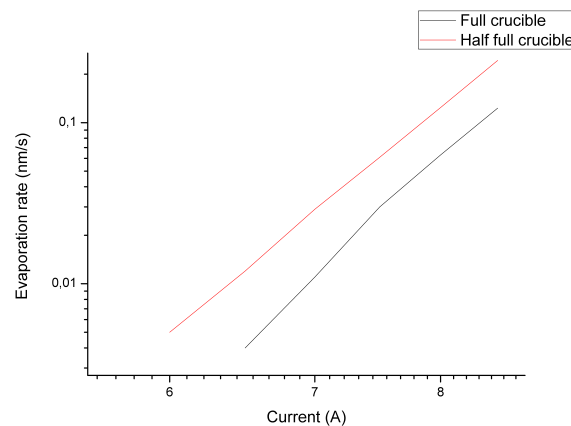
All spectra were in the range from 720 to 1050 nm (1.72 to 1.18 eV) of the pulse laser. Spectra were measured both for  $Pp$  and  $Ps$  and a reference was measured with a quartz wedge crystal for  $Pp$  as the intensity of the pulse depends on the wavelength of the OPO. Pedersen and Morgen [68, 69, 70] and Pedersen et al. [71] have made several papers on SHG from a Si(111)  $7 \times 7$  reconstruction. Three different peaks were observed when measuring a spectrum from 688 nm to 1240 nm, located at 730 nm, 954 nm, and 1060 nm. The first peak is due to a strain induced resonance near the band gap of Si at 3.4 eV (365 nm) [72], which was also concluded by Daum et al. [73]. This peak will also be referred to as the stress induced peak. The two following peaks arise from surface states caused by dangling bonds after the reconstruction and would quickly diminish if the dangling bonds are extinguished. [68] These will be referred to as dangling bonds peaks.

Figure 3.3 shows spectra for  $Pp$  and  $Ps$  on the Si surface. Here a clear peak is observed around 730 nm of the pulse laser for the  $Pp$ . This is well in line with the aforementioned peak observed by Pedersen and Morgen [68]. Looking at the  $Ps$  signal a similar peak is seen, though at a slightly lower wavelength. The peak is cut short due to the degeneration of the OPO which gives data out of propor-

tions and diminishes the scale of the rest of the data. The  $P_s$  signal is lower than  $P_p$ , which could be due to destructive interference between the contribution from the surface states stemming from the reconstruction and the interband transition [74, 75, 23]. Tom et al. [29] theorizes for an isotropic medium no s-polarized SH signal can be generated from a purely s- or p-polarized fundamental beam, thus the s-polarized signal contains the anisotropic contribution. This could explain the difference in signal strength between  $P_p$  and  $P_s$  as the difference in the orientation of the uppermost layers would affect only the s-polarized signal. Looking at the  $P_s$  signal a second peak can be observed around 960 nm and 1000 nm, which is in the same range as the two second peaks observed by Pedersen and Morgen [68]. These peaks stem from dangling bonds being present at the surface after reconstruction, which could explain why the peak is not present in the  $P_p$  signal.

Three different nonlinear spectra peaks are shown on the Si(111) surface and will be used as a baseline for further spectra measurements to see how the signal changes at these three wavelengths for surfaces different to the substrate.

### 3.4 Evaporation Rate



**Figure 3.4:** Evaporation rate measured with quartz crystal at different currents plotted with a logarithmic scale bar.

The flux of the evaporated material can have a big influence on the growth of the thin film. Thus in order to ensure a steady and comparable evaporation rate throughout the different experiments, measurements were carried out using a Q-pod quartz crystal monitor.

Figure 3.4 shows the evaporation rate as a function of the current through the

coil. Here it can clearly be seen that the flux is exponentially dependant on the current as soon as a steady rate is achieved. A rate of around 0.01 nm/s is wanted for the experiments, as a too high flux would undermine detecting the individual peaks from the SHG signal as the film grows, as the thickness changes too rapidly for the detector. Another possible outcome of the high flux is a more disordered growth. That means that a current of 7 A with a full crucible should lead to a desired evaporation rate. The evaporation rate was measured again after the crucible was half empty as seen in Figure 3.4. Here a huge difference is observed when compared to the full crucible with a doubling of the evaporation rate. This could be due to a few reasons. First, it could be contributed to the reduction of the mass present in the crucible. The mass could be assumed to be half, but the energy added to the crucible stays constant. It's known from thermodynamics that the temperature is linear dependant on the mass and the energy transferred, which means that half the mass takes half the energy to heat up, thus a doubling in the evaporation could be expected, if all the heat from the crucible is transferred. The heat transfer from the crucible to the Ag might change throughout the experiments, as the contact area between the Ag and the crucible shrinks during evaporation, meaning less energy is transferred and that other factors might play in to get the doubling in rate.

The second factor could come from the shape of the crucible. As the Ag evaporates, the surface of the Ag is moved further into the crucible as seen in Figure 3.5. This would lead to a chimney effect where the spread of the evaporated Ag is reduced, as some of the evaporated Ag would hit the crucible walls, this Ag would then re-evaporate, in new directions, leading to a higher surface area, thus a higher evaporation rate. This combined with wetting of the crucible walls could be the main factor for the increase in evaporation rate as the Ag evaporates.

The Third factor could be the pressure from the vapor. As the Ag evaporates, the pressure around the crucible will increase. This pressure increase leads to a more dense gas with more collisions, thus moving the effective point of evaporation. The empty space inside the crucible will increase as Ag evaporates, leading to a higher pressure, Thus more collisions and less directional evaporation. These collisions could also form aggregates of Ag, that could end up on the surface

These experiments show that thermal evaporation from a crucible is an unreliable method as the evaporation rate depends on the amount of Ag, meaning the rate will change constantly throughout the experiments, with a doubling already occurring halfway through the Ag. But it is possible to estimate the film thickness, at a specific current, by measuring the rate before and after deposition and then assume a linear tendency between these two measurements. This would lead to an estimated rate as a function of time, thus giving the actual thickness of the deposited film. Experiments will then have these two rates measured if able.



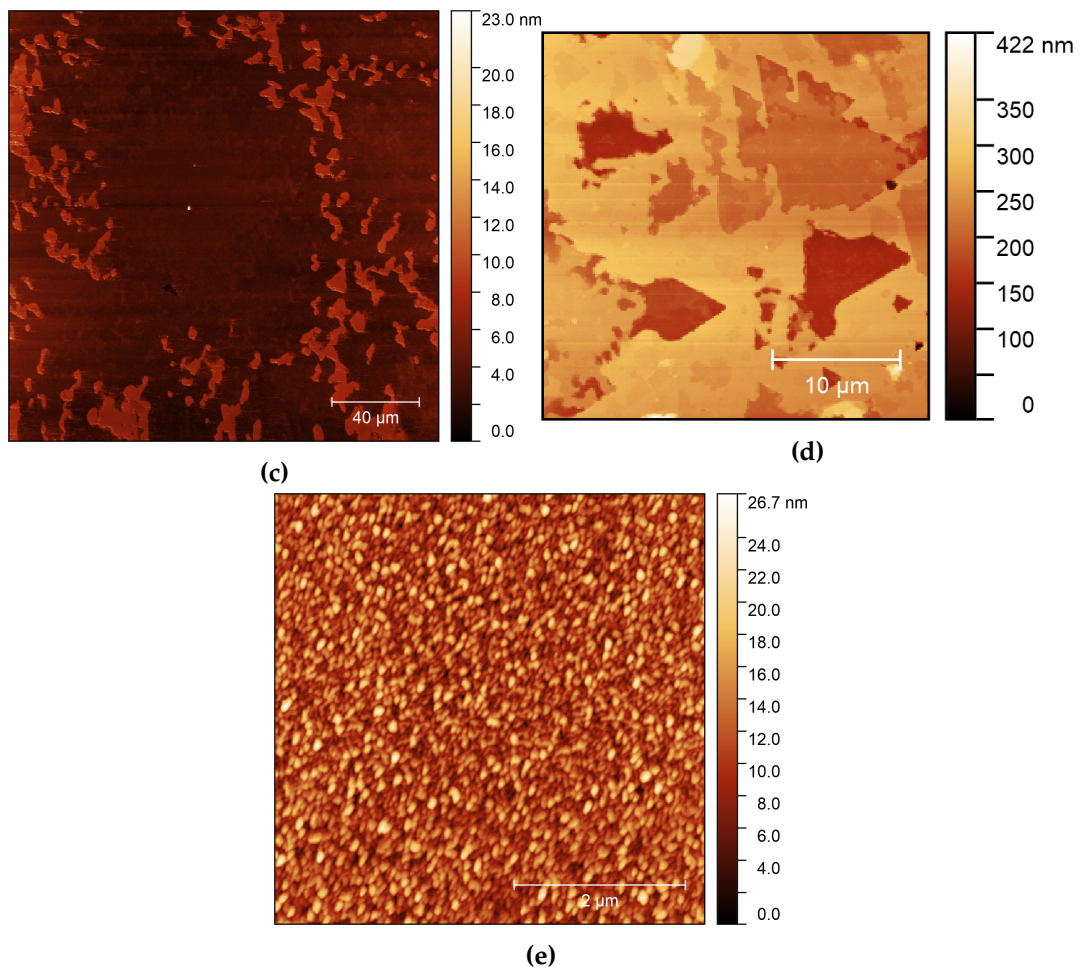


**Figure 3.6:** AFM images of Si(111) surface after deposition of Ag a) and b) with subsequent standard annealing. c), d) and e) without any extra treatment.

AFM measurements were carried out on Si after deposition of Ag. Figure 3.6a and 3.6b shows the Si surface after deposition of Ag and standard annealing as mentioned in Section 3.1, whereas Figures 3.6c, 3.6d, and 3.6e shows a surface after deposition but without annealing.

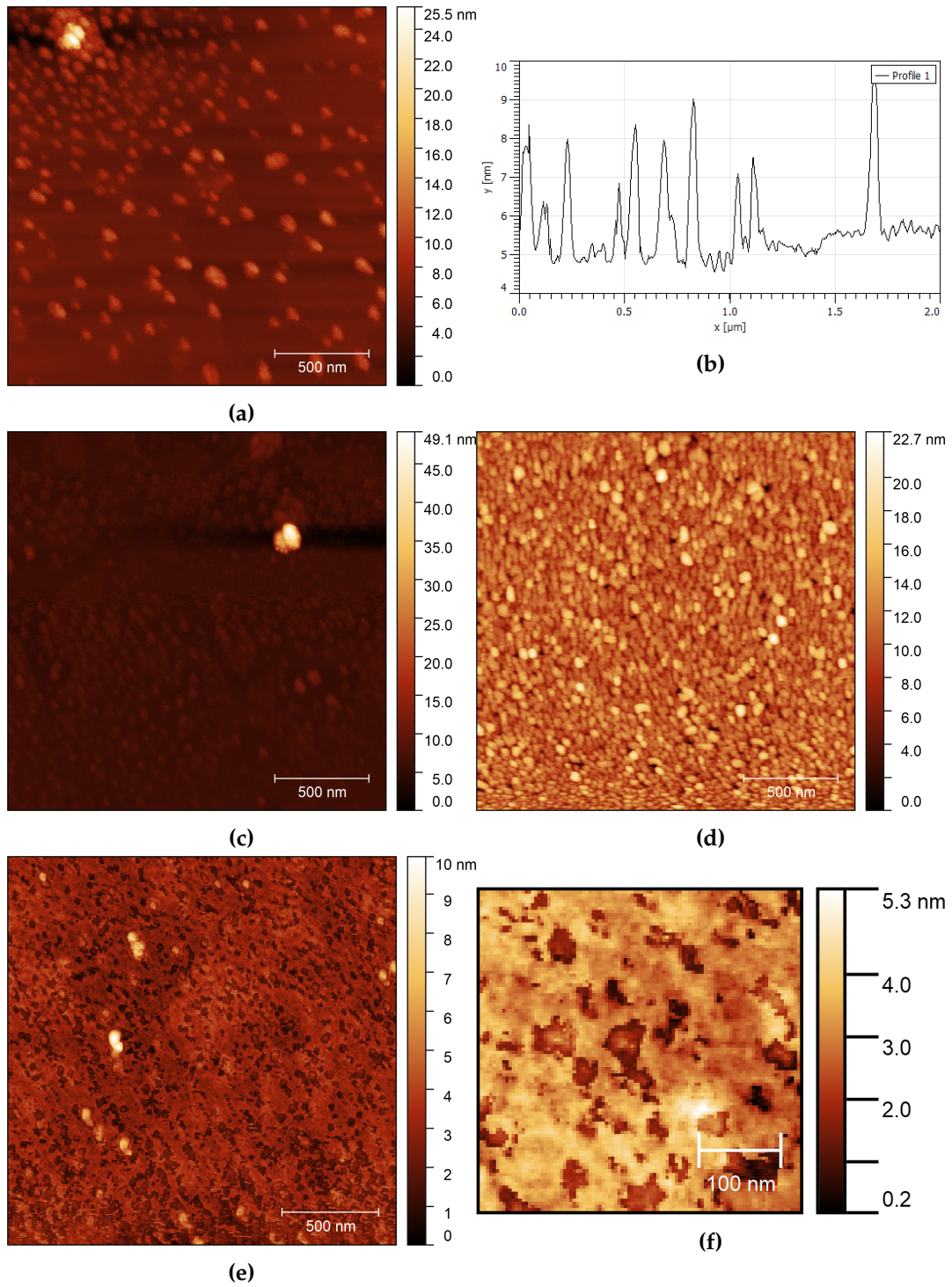
On Figure 3.6a no clear structures are present, instead small cavities and larger individual particles are observed randomly throughout the sample. Furthermore, lines can be seen through out the sample, these lines are most likely an artifact from the AFM itself as they occur on both sides of big particles with a valley and a hill on either side. nothing is present to indicate the existence of a thin film on the Si surface. This implies that the annealing of the Si surface is a suitable method for cleaning, allowing for further use of the same sample. The same tendency is

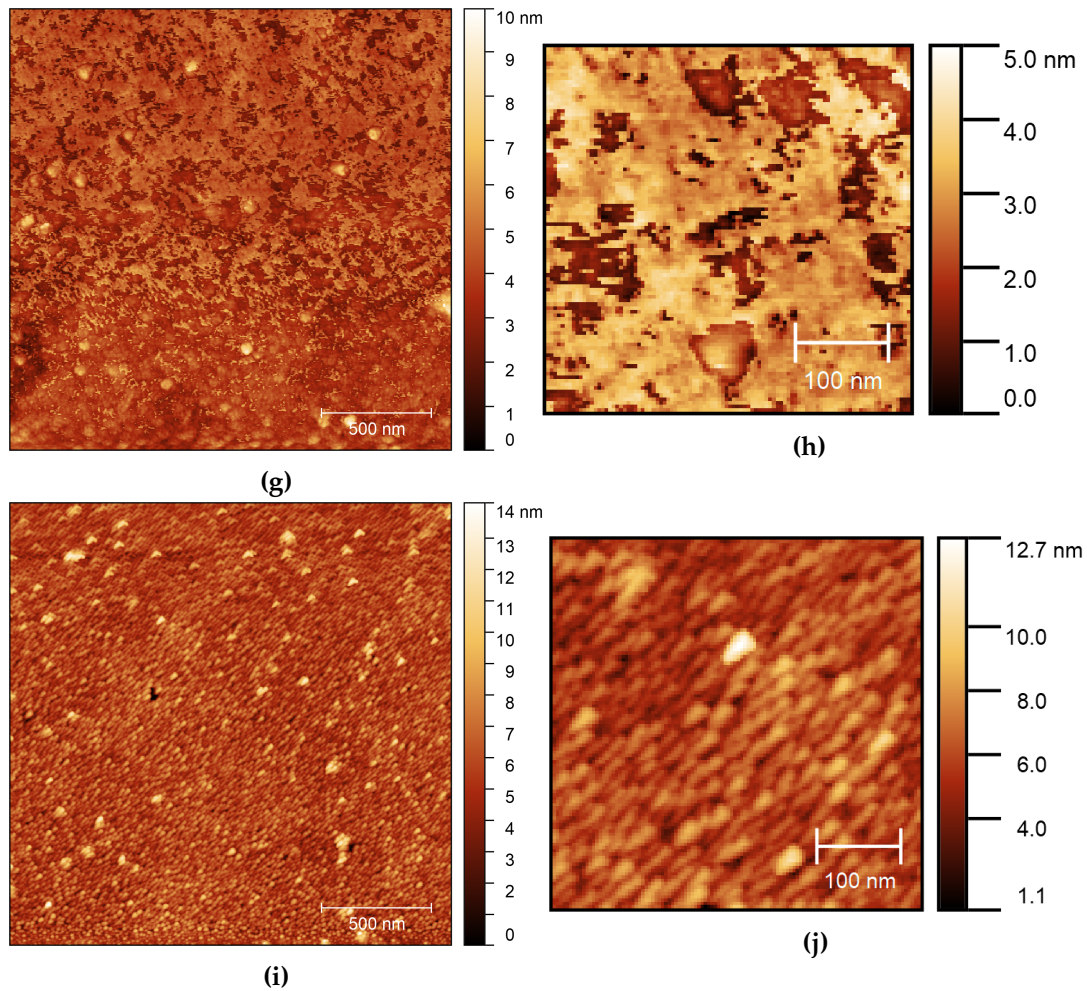
seen in Figure 3.6b. Here the measurement is carried out on the edge of the film between the treated and untreated area of the surface. Here no indication is visible between these two areas, which once again supports annealing as a cleaning method. The presence of cavities on both samples could either indicate Ag, or it could be imperfections in the Si surface. As they are seen on both the treated and untreated part of the sample on Figure 3.6b it's most likely from irregularities on the Si surface or an artifact from the AFM itself.

Figure 3.6c is measured on the center of a Si sample after deposition but without annealing. Here it is possible to see indications of an Ag thin film in form of triangular structures on the surface and a triangular vacancy in the center, meaning that the evaporation process, in fact, creates a thin film on the Si substrate. Figure 3.6d shows the same sample but near the edge of the treated area. Here huge triangular domains are observed mostly in the form of vacancies. These domains are a lot larger than those observed in the center of the sample as seen in Figure 3.6c. This could mean that the evaporation rate, and thus the thickness, varies at different positions on the surface relative to the evaporator.

Figure 3.6e tells another story, as instead of a film consisting of flat triangular domains, it consists entirely of small spherical domains. This could be caused by a few things. Firstly, it could be due to the surface not being a complete layer thus still forming islands. As mentioned in Section 1.4 a large lattice mismatch is found between Ag and Si, thus a combination of layer and island growth is expected, as explained by Stranski-Krastanov growth [1]. As more material is deposited, it is possible to observe Ostwald Ripening [76], which is a growth mode in which smaller particles aggregate together to form larger structures. This combined with deposited material filling out the gaps, it should create a coherent film, despite the difference in surface tension. Another reason could be sputtering during deposition, so instead of having a steady rate of deposition, Ag is deposited on the surface in bursts, thus hindering stable growth. Lastly, it could be due to Ag forming aggregates before hitting the substrate surface, thus depositing as preformed particles.

3.5.2 AFM on Wedge





**Figure 3.7:** AFM images of a Si surface a) near the area of deposition. b) Histogram of a). c) With an Ag thin film with an estimated thickness of 3 nm. d) With an Ag thin film with an estimated thickness of 8 nm. e) and f) with an Ag thin film with an estimated thickness of 10 nm. g) and h) with an Ag thin film with an estimated thickness of 15 nm. i) and j) shows AFM images of an area of a wedge sample where GLAD might be present

In order to better study different film thickness of Ag on Si(111) a wedge was created and AFM measurements were carried out. Figure 3.7 shows selected AFM images of different steps on the wedge to see the growth at different thicknesses. The histogram correlates to the AFM image on the left. The remaining histograms can be seen in Appendix B.

Figure 3.7a shows an AFM image of the untreated Si surface near the edge. Here no indication of a clear Ag film is present, but small particles with a height of around  $3 \pm 0.5$  nm is visibly spread throughout the surface. This could indicate that the method of shadowing for parts of the sample is suitable for the experiments as it blocks most of the incoming Ag. Only some Ag has reached this part of the surface and, due to the mismatch between Ag and Si, has formed islands, instead of a coherent film. These particles are more densely packed in the top of the images which is closer to the edge between treated and untreated area. This could indicate that the Ag is being deposited behind the blocking screen but the amount falls drastically with the distance.

Figure 3.7c shows AFM measurements carried out on the area of the wedge that should have a thickness of around 3 nm. Here islands are present again as it was in Figure 3.7a, but closer packed and with an average height of  $2.5 \pm 0.3$  nm. This could indicate that a film is starting to grow between these islands and is further supported by a height difference of around 2 nm between the top and bottom area of the images. So at a thickness of around 3 nm a coherent film is starting to form on the surface on the Si substrate.

Figure 3.7d shows AFM measurements carried out on the area of the wedge that should respond to around 8 nm in thickness. Here the sample is covered in closely packed particles with a height around  $2.5 \pm 0.4$  nm compared to the surface of the film. The coherent film in between these island has a height of around 6.5 nm when comparing the average surface height to the dark spots on the surface. When comparing the size of the islands sticking up above the film on Figures 3.7a, 3.7c and 3.7d, it's roughly within the same size range. This could indicate that the growth of the film follows the growth of these islands. So the growth of the islands happens and then the film grows in between them and when a complete film is grown more islands begin to form. It could also be that the islands and the film grow at the same rate, thus keeping the height difference between them consistent.

Figure 3.7e and 3.7f shows images of the surface with an estimated thickness of around 10 nm. Here no islands are seen as they were on the previous images, instead a smooth coherent film can be observed with very few particles scattered over the surface. These particles have an average height around  $6 \pm 1.5$  nm. When

looking closer at the film on Figure 3.7e, small areas can be seen breaking up the surface, and when zooming in, as seen in Figure 3.7f, they seem to be growing in a triangular shape. This could indicate that the growth of the Ag is no longer influenced by the Si substrate

These triangular domains are also spotted on Figure 3.7g and 3.7h. These depict the surface of an expected thickness of around 15 nm and here a coherent film, interrupted by cavities, is once again visible. The domains on Figure 3.7h are within a size range of  $60 \pm 10$  nm whereas the domains on figure 3.7f is within  $30 \pm 10$  nm. This could mean that the film continues to grow after the first coherent layer is formed and so does the triangular domains present on the surface.

Lastly Figure 3.7i and 3.7j shows an interesting phenomenon. Here the particles present on the surface seems to be directional instead of growing straight up. This could be due to a phenomenon called glancing angle deposition (GLAD), where the angle of incident is large in relation to the surface normal. This leads to directional growth of surface structures as they cast a shadow on each other, thus blocking the incoming flux for everything but the top of the grown structures. GLAD could have occurred on the sample due to the growth of islands when the sample is directly exposed to the flux. These islands would then act as a seed for GLAD structures to grow from when they are moved behind the screen. If some Ag makes it up behind the screen, which was seen in Figure 3.7a, GLAD structures would grow as the islands creates a shadow for each other.

### 3.6 Evaporation of Ag

The three different thin films being of focus in this report is Ag, Al, and AlN. The first measurements were done on Ag as it is one of the most well studied thin films for SHG and is used to get a general understanding of SHG in metals.

#### 3.6.1 In Situ Measurements of Ag Evaporation on Si

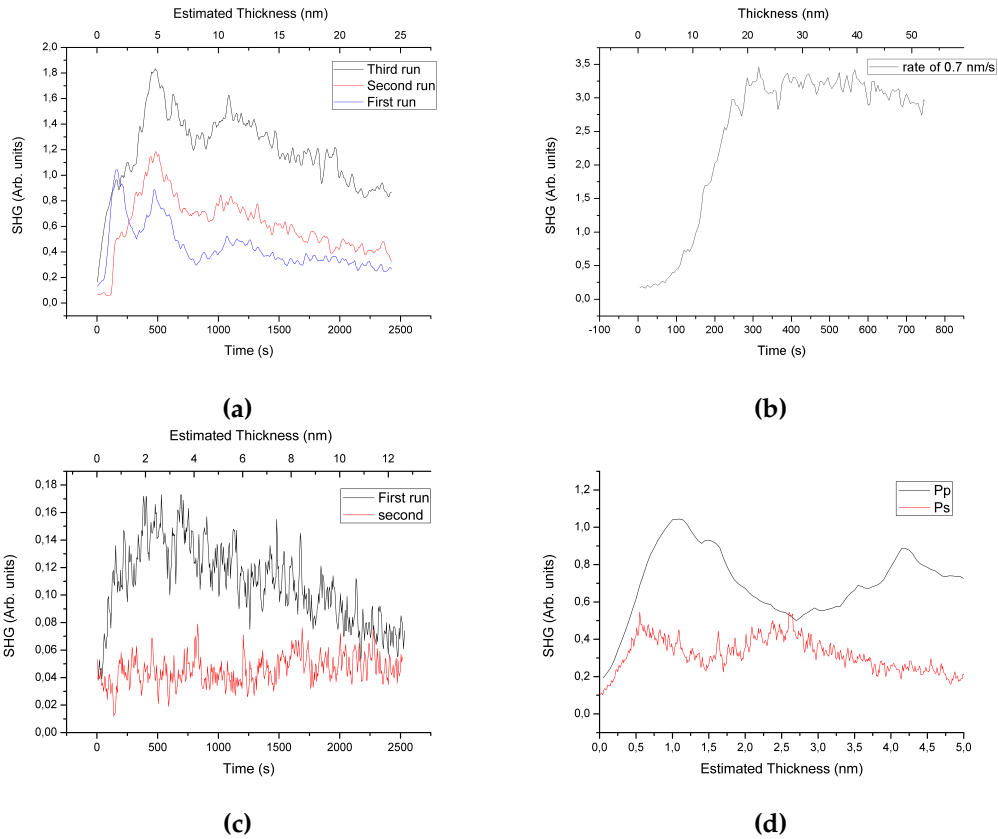


**Figure 3.8:** The SHG intensity during Ag deposition measured with the Nd:YAG laser at 793 nm fundamental wave for  $P_p$  with  $\theta = 60^\circ$  with an estimated rate of a) 0.01 nm/s. b) 0.07 nm/s. c)  $P_s$  signal with estimated rate of 0.005 nm/s for two different runs. d) Comparison between  $P_s$  signal with estimated rate 0.002 nm/s and  $P_p$  with estimated rate of 0.01 nm/s.

Figure 3.8a shows the reflected SHG signal measured during evaporation of Ag utilizing the thermal evaporation setup mentioned in Section 2.1.4. The current from the power supply connected to the evaporator was set to 7 A for all three runs and the fundamental wave was 793 nm (1.56 eV) corresponding to a second harmonic wave of 397 nm (3.12 eV). The estimated thickness is based on an expected deposition rate of 0.01 nm/s, based on measurements from the Q-pod prior

to the first run. Though, as mentioned in Section 3.4, the evaporation rate changes with the amount of material present in the crucible, where the decreasing amount of material leads to a higher rate. This could explain the first peak in the first run missing in the two consecutive runs. Another possibility is the very steep increase in signal, which could indicate a delay in the software or detector.

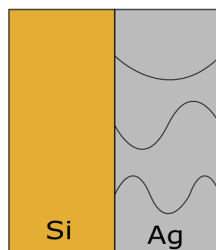


**Figure 3.9:** Illustration of the standing waves in Ag for different film thickness on Si.

A similarity between the three runs lies in the oscillating behavior of the signal. This corresponds well with the findings of Pedersen et al. [71]. Even though the SHG measurements were on a wedge with different thickness of Ag created at a temperature of 170 K compared to a continuous measurement during growth at room temperature which was made in this report. These decaying oscillations stem from quantum wells in the Ag. Every time the film is thick enough to support a standing wave, a resonance peak is seen, as can be seen in Figure 3.9. The Bohr-Sommerfeld Quantization rule  $2kd + \phi_C + \phi_B = 2\pi n$  gives the requisite for the standing waves, with  $k$  being the wave vector of a free electron propagating in a layer with thickness  $d$  and  $\phi_C$  and  $\phi_B$  being the phase changes upon reflection at crystal and surface barrier respectively. [77] The decay is due to increased absorption in the metal as the thickness increases and less signal is able to be generated from the Si surface. Comparing more with the work of Pedersen et al. [71] the thickness range is from 0 to roughly 50 ML. Going by atomic diameter and packing of atoms one ML should have a thickness of approximately 0.25 nm, thus a couple of individual peaks are expected within the first 12 nm of Ag. Similar peaks are visible in Figure 3.8a, thus 0.01 nm/s seem sufficient for probing quantum well states in Ag using the Nd:YAG laser.

The first run seems to have an additional peak at the beginning, this could be due to the speed at which the collector collects data since the second and third runs would have a higher deposition rate and thus fewer data points. Another possible explanation for the missing first peak and also the tendency of larger signal for the later runs is the effect of the annealing. If the annealing process has not reset the Si surface by removing all the Ag, the starting point for each run would be different. The first peak would not be visible if that thickness was already reached or bypassed at the start of the second and third run, combined with the possibility of

fewer data points, due to a higher rate. An important note is, besides the first peak in the first run, the three runs align pretty well, indicating similar growth as the quantum well resonances are very thickness specific. This speaks more of a similar rate and starting point for the three runs and the difference for first peak lying in the detector and software. As mentioned in Section 1.4 Ag growth on Si(111) is more prone to growing a combination of islands and layers instead of just layers. These islands have shown to enhance the SHG signal [78] and if some islands are still present on the probed surface or diffused Ag in the Si surface, it may increase the signal and explain the difference in intensity for the three runs.

Figure 3.8b shows another attempt at achieving oscillations in the SHG signal through quantum wells occurring in the Ag film at different thicknesses. Instead of the oscillations seen in Figure 3.8a, here a steady increase in the SHG signal is visible. This could be due to the much higher evaporation of 0.07 nm/s making disordered growth more preferred, thus creating more islands and particles. Pedersen et al. [78] found a similar tendency when growing Ag on Si(111) at a substrate temperature of 210 K. At this low temperature, the Ag is not able to diffuse on the surface in order to create a stable layer and thus grows very disordered leading to an overall increase in the SHG intensity. The high evaporation rate would also give a more rapid change in thickness, which might be too rapid for the equipment to keep up, as the repetition rate of the laser cannot go beyond 10 Hz, thus causing the individual peaks to disappear into the steady increase of the overall signal.

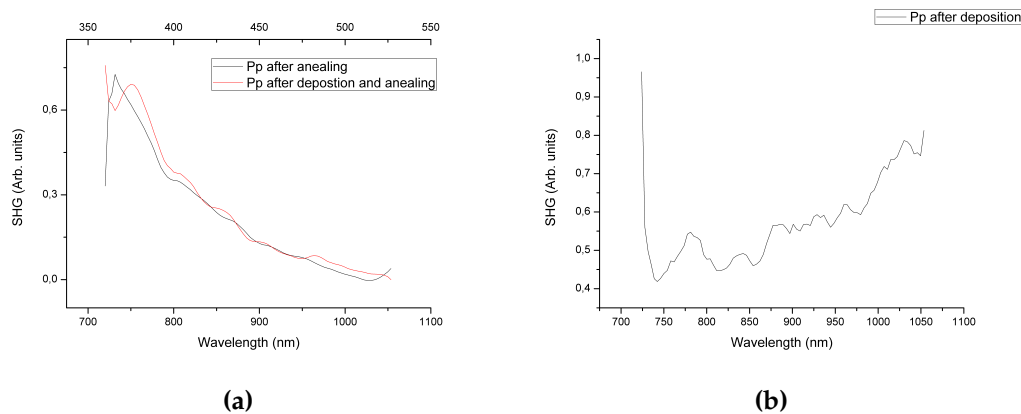
In situ measurements of Ag deposition were also made with  $P_s$  polarization to see the difference from  $P_p$  which can be seen in Figure 3.8c. The first run shows a similar tendency as seen in Figure 3.8a, but the individual oscillations are more difficult to distinguish. Pedersen et al. [71] saw a similar difference between  $P_p$  and  $P_s$  where the  $P_s$  signal show half the period length compared to  $P_p$  at half the amplitude, which would explain the more rapid oscillating behavior. Same is seen in Figure 3.8d, in which the first two peaks for  $P_s$  are roughly at the same intensity and first afterwards, a decay is seen. Comparing  $P_s$  and  $P_p$  in Figure 3.8d the period lengths are roughly 1.9 nm and 3.5 nm corresponding to 7.6 ML and 14 ML respectively. These results are close to the findings of Pedersen et al. [71].

The second run in Figure 3.8c does not show a peak followed by an oscillating decay, but instead an overall increase of the signal. As mentioned Ag islands have shown to yield enhancement of the SHG signal and the run parameters may have favored a more disordered growth and thus creating more islands. As mentioned in Section 3.4 the evaporation rate is highly dependant on the amount of Ag present in the crucible and a couple of longer evaporation experiments have been conducted between the two runs in Figure 3.8c without refill, thus the second

run might have had a higher rate than assumed and terminally giving a scenario reassembling the one in Figure 3.8b.

By comparing the three different runs seen in Figure 3.8a it seems there is a possibility of using SHG as a method for measuring the thickness of metallic thin films in situ. The SHG measurements seem to oscillate at the same thickness of the film if the difference in rate and the fact that only the first run used a completely clean Si surface is taken into account. This would mean that by just looking at the shape of a graph produced during a deposition run could give an estimate on the films exact thickness, under the assumption some sort of layer growth is present. By making more experiments with a lower rate, a possibility of more oscillations and by that more distinct thickness peaks could be possible with  $Pp$  polarization. This is due to the high deposition rate throughout these experiments and the limitations occurring from the laser as smaller changes are not observed with the low repetition rate of the laser, as was the problem seen on Figure 3.8b with a rate of 0.07 nm/s.

### 3.6.2 Nonlinear Spectroscopy of Ag Film on Si

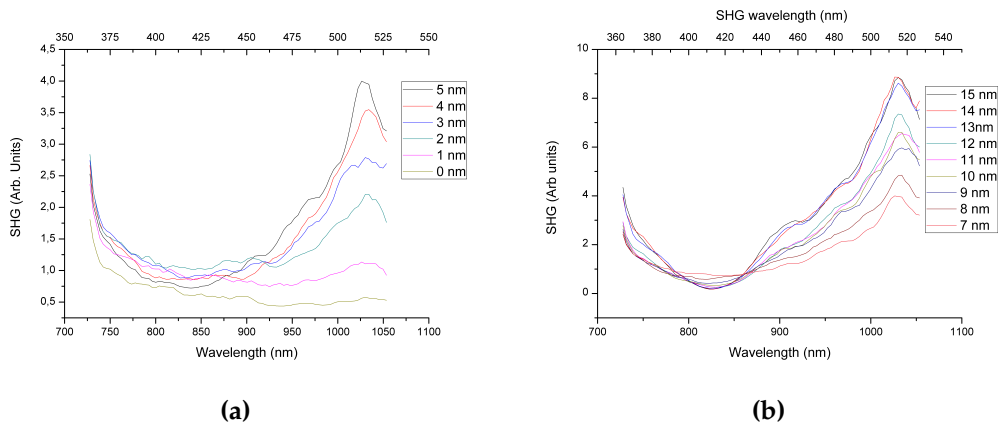


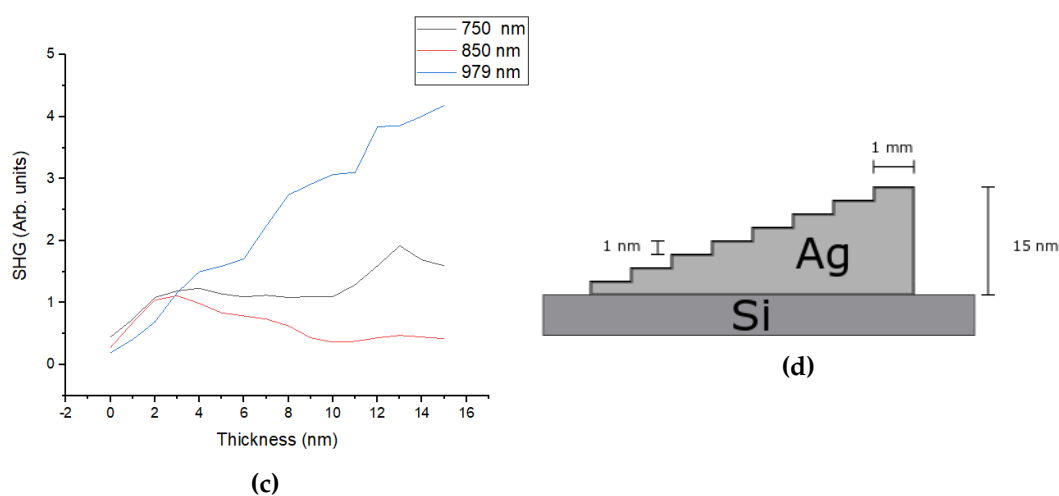
**Figure 3.10:** Spectra for the second harmonic signal intensity from 720 to 1050 nm wavelength with  $\theta = 60^\circ$  for a)  $Pp$  polarization on Si after annealing with and without deposition prior. b)  $Pp$  polarization after deposition of Ag on Si.

Figure 3.10a shows spectra measurements of a clean sample after annealing to remove foreign elements from the atmosphere and the native oxide layer, and the spectra measurements of a sample after deposition of Ag, followed by annealing. The two measurements are very well aligned in form and could indicate further approval for the annealing as a sufficient way of cleaning and resetting the surface in between Ag depositions, as mentioned in Section 3.1.

Figure 3.10b shows the spectra of a sample with Ag deposited on it. The SHG peak originating from the Si wafer is still visible at around the 730 nm of the pulse laser. This peak has been cut short in order to better being able to see the rest of the graph on the Figure. Thus only a thin layer of Ag must be present on the substrate since the Si is still generating a signal. As mentioned in Section 3.6.1, the disordered island growth of Ag on Si(111) can enhance the SHG intensity. This can explain the increased signal at the stress induced peak compared to Figure 3.3. The peak seen at the end around 1050 nm is not believed to be from dangling bonds, as was the case in Figure 3.3, since these bonds are very surface sensitive and as such should not be present after deposition of Ag. Another indication this peak is not from dangling bonds, is the lack of dangling bond peaks for the  $Pp$  polarization, seen in Figure 3.3. Instead this peak could originate from Ag nanoparticles as the plasmon resonance of Ag nanoparticles is in the range of 400-550 nm depending on size [79] and medium [80, 81]. This peak should increase with the amount of material deposited, if the deposition parameters have favored island and particle growth, as seen in Figure 3.8b. In Figure 3.10b the substrate temperature was room temperature, but an increased deposition rate could have created a similar scenario as seen in the low temperature experiments by Pedersen et al. [78], mentioned in Section 3.6.1. It is also worth mentioning the measurements at the beginning and the end of the spectrum could be influenced by the OPO as it has shown some limitations at the ends of its spectra.

### 3.6.3 Nonlinear Spectroscopy of Ag Wedge on Si





**Figure 3.11:** Nonlinear spectra measurements from 720-1050 nm at  $\theta = 60^\circ$  on a) the first seven steps of the wedge, b) the last 9 steps. c) The signal as a function of thickness at three different wavelengths. d) Illustration of the wedge.

As mentioned in Section 3.5.2, a wedge was created with each stage being 1 mm wide and 1 nm thicker than the previous going from 0 to 15 nm. Figures 3.11a and 3.11b shows the different spectra measurements made on the different stages on the wedge. Figure 3.11a being the first 6 nm. The first peak is the stress induced peak visible around the 730 nm. Comparing Figures 3.11a and 3.11b it is apparent that a thicker layer initially results in a higher intensity signal looking at the stress induced peak. This could be correlated to the SHG enhancement by the Ag island growth as mentioned in Section 3.6.1. Another interesting aspect is the signal strength at 979 nm showing a similar tendency as seen in Figure 3.10b with an increasing signal with increasing thickness.

In Figure 3.11b around the peak at 1000 nm a distinction can be seen with vertical jumps between 7 and 8 nm and again between 11 and 12 nm. As mentioned in Section 3.5.2 a nearly complete layer can be seen around 3, 8, 10 and 15 nm thickness, which corresponds roughly with the jumps seen in the spectra measurements. As mentioned earlier, it is the island and nanoparticle growth, which facilitates this increased signal, thus when the top of the film is closest to a complete layer, a lower signal is expected.

This tendency can also be seen in Figure 3.11c where the signal is plotted against the thickness for three different wavelengths. It can clearly be seen how the signal at 979 nm increases as the nanoparticles and islands form, but then the rate of increase decreases as the film becomes more coherent until more islands start to grow. The signal at 750 nm and 850 nm is seeing an initial increase from the enhanced signal corresponding to the first islands growing. Another possible

explanation for the signal increase around 750 nm is electric field induced second harmonic generation (EFISH). Equation 1.5 could be furthered to include a DC term  $P(2\omega) = \chi^2 E(\omega)E(\omega)E_{dc}$ , which would increase the polarization. The DC field could be externally applied, but when working with semiconductors, can also occur in the space charge region as an effect of band bending. [82] Depositing a metal would change the surface potential and thus increase the field strength of the electric field in the space charge region. [83]. The curve at 979 nm resembles the step isotherm [76] with each step correlating to a filled layer, as earlier described. These steps corresponds well with the growth seen in the AFM images in Section 3.5. The Si signal is more or less constant up until 10 nm thickness where a step is observed similar to the layer.

In Figure 3.8a in Section 3.6.1 it can be seen that after an initial peak for each of the three runs, the signal strength decays with increasing thickness. The wavelength was 793 nm and comparing to the graph of 979 nm in Figure 3.11c a steady increase is observed with thickness. If comparing to Figure 3.8b which had a rate seven times higher than expected, it keeps increasing even after 15 nm thickness, which is similar to the behavior of the 979 nm measurement in Figure 3.11c. Thus the step size could mimic a too high evaporation rate and facilitate a very disordered growth of islands and particles. If looking at the graph for 850 nm, the behavior is similar to what is seen in Figure 3.8a with an initial peak followed up by an oscillating decay in signal strength. Another possibility for the steadily increasing signal could be the spot size of the laser, as it is not able to be measured in the chamber. If the spot size has not been properly focused on one stage or is too wide and thus crossing over two different stages, which could be seen as a disordered surface. This would create a signal from two different thicknesses and could change the signal.

A second wedge was created, this time with roughly 0.3 nm between each stage. Looking at Figures 3.12a, 3.12b, 3.12c and 3.12d they show the same tendencies as those seen in Figure 3.11. An initial peak can be seen around 750 nm which is peaking around 1 nm. Until 3 nm when a complete layer is seen in the AFM images and the second peak at 1000 nm emerges. Though it is worth noticing, that the second peak is larger relative to the first two peaks as the thickness increases, the actual signal strength is oscillating and is at a minimum when the thickness is 5.66 nm. This can also be seen in Figure 3.12e. Figure 3.12e shows the signal as a function of thickness. The same wavelengths are chosen as Figure 3.11c, but this time the form is much more like the one seen in the in situ measurements, which could mean this wedge is mimicking a lower evaporation rate, compared to the first wedge. Figure 3.12f shows an in situ measurement compared with the wedge measurement. The peaks are located at the same thicknesses, though the amplitude of the signal is different.

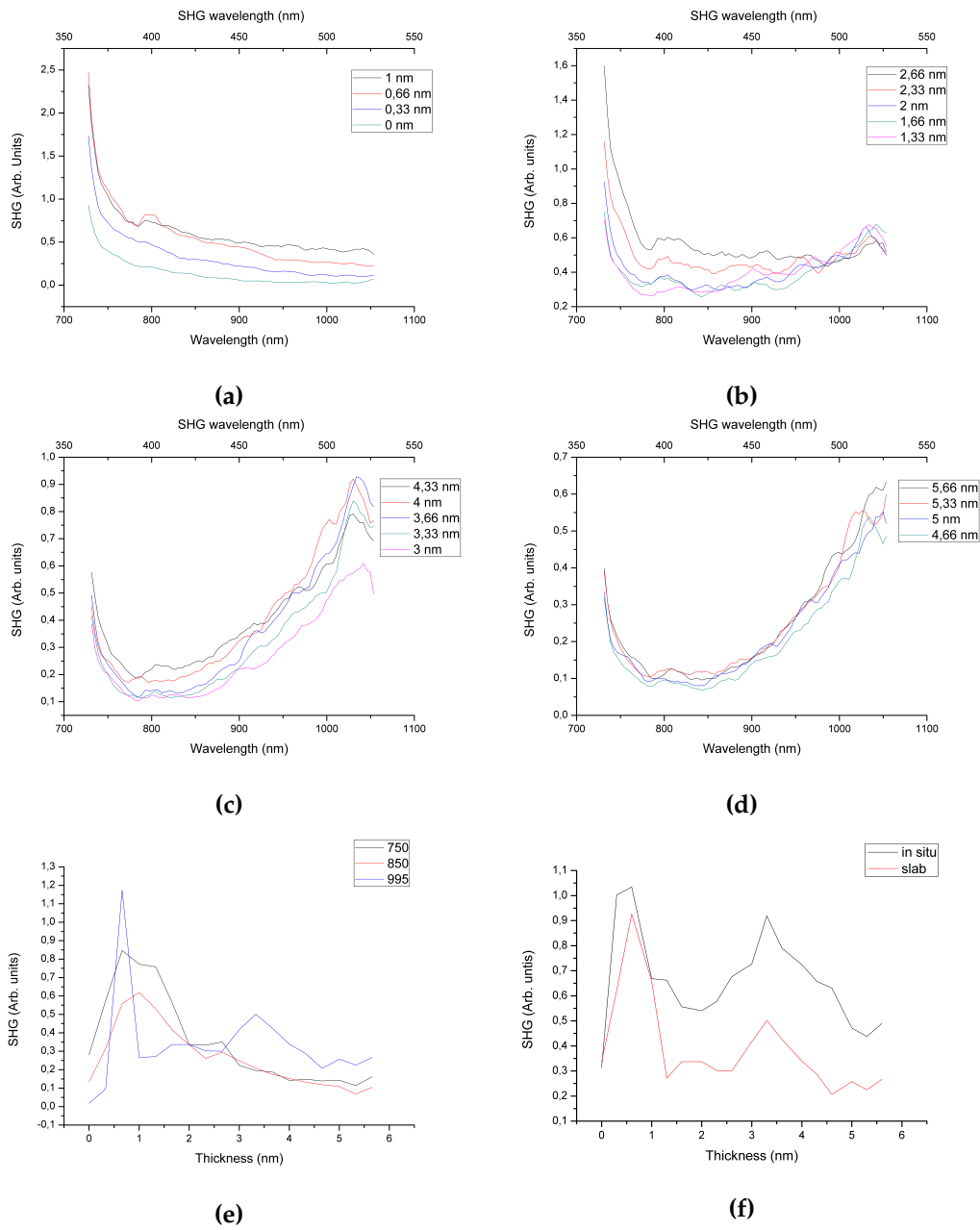


**Figure 3.12:** Nonlinear spectra measurements from 720-1050 nm at  $\theta = 60^\circ$  on wedge with step thickness a) from 0 to 1 nm, b) 1.33 to 2.66 nm, c) 3 to 4.33 nm, d) 4.66 to 5.66 nm. e) The change in thickness for different wavelengths. f) The wedge measurement compared to evaporation measurements at 792 nm.

This means that the in situ measurements would give peaks at the same thickness as with the wedge and thus would help validate the in situ measurement in terms

of thickness determination. The spectra measurements on the wedge were made the day after creating the wedge and even though the measurements were done in vacuum conditions, a small amount of oxide could still contaminate the surface and form a layer, which could explain the difference in signal strength seen in Figure 3.12f.

### 3.7 First AlN Setup

AlN thin films are more used in industry due to its many advantages as mentioned in Section 1.3. The setup used for Ag evaporation is not able to create AlN films due to lack of a nitrogen source thus another setup is needed. Both Al and AlN films were made in order to use the Al films to better compare to Ag and in order to test whether the atomic nitrogen has successfully been cracked from the  $N_2$  source. Due to the AlN setup having a different geometry than the previous setup, some experiments had to be made prior to AlN deposition. Primarily investigating the effect of the small incident angle of the fundamental beam and the ability of the AlN setup to prepare  $7 \times 7$  reconstructed surfaces for growth.

#### 3.7.1 Hydrogen Surface Treatment

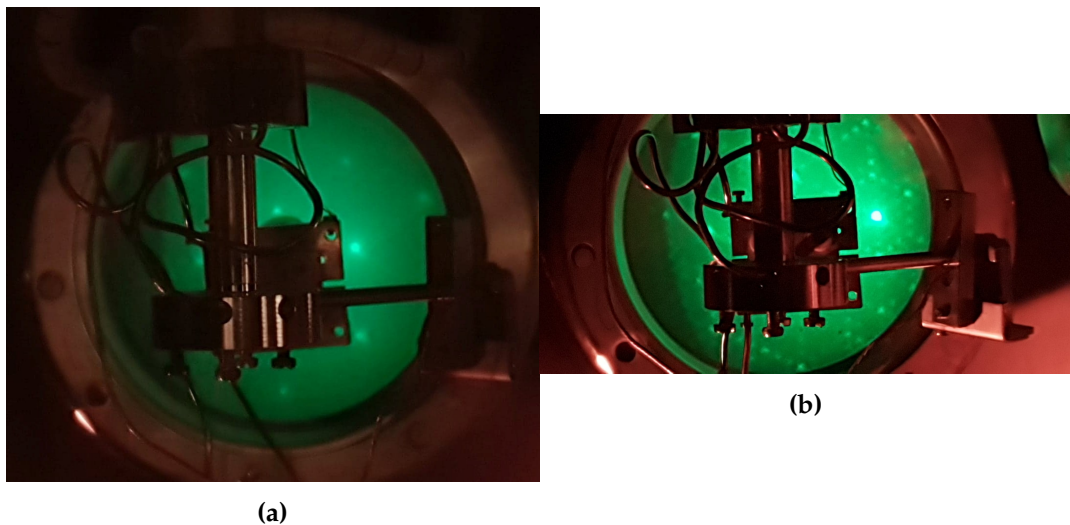


**Figure 3.13:** Images of LEED patterns of a hydrogen terminated Si(111) surface at a) 85 eV and room temperature. b) 90 eV and after 900 °C annealing.

Due to substrate heating limitations in the AlN setup, extra sample preparation was needed. The Si(111) substrates were submerged in HF in order to remove the native oxide layer and hydrogen terminate the surface. Getting a well-defined

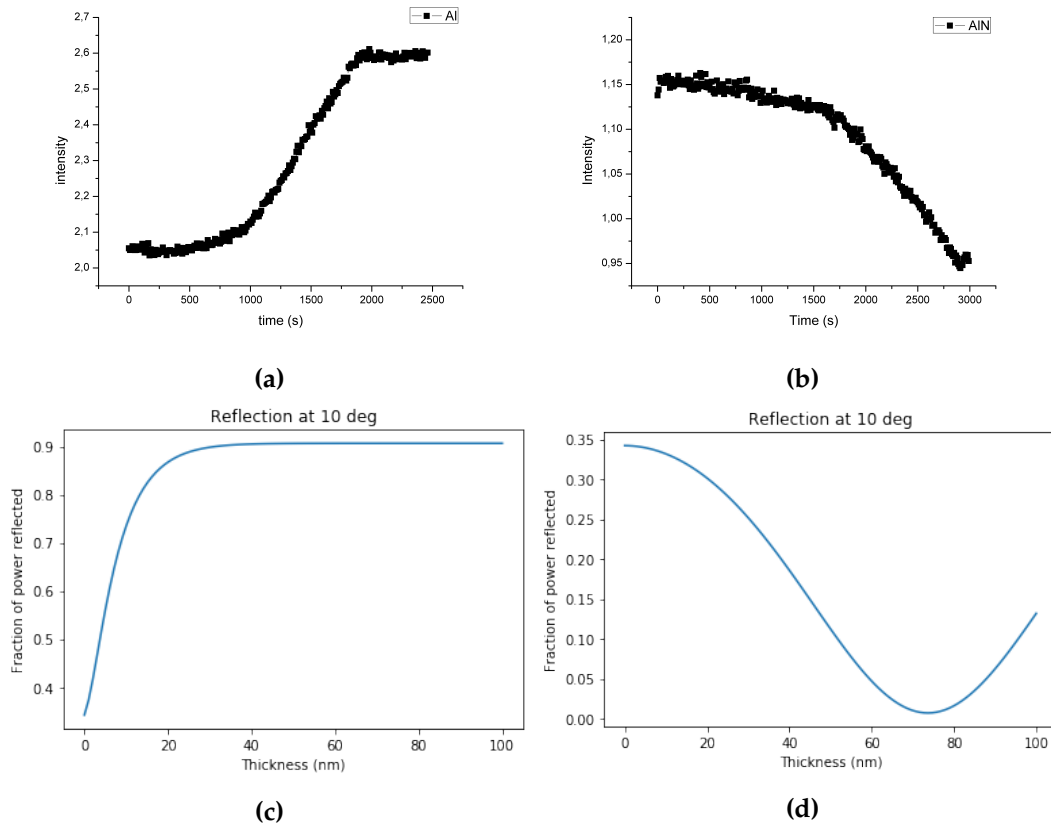
Si(111) surface is important for thin film growth and should be achievable at lower temperatures for a hydrogen terminated surface compared to a surface with a native oxide layer.

In order to examine at what temperature the  $7 \times 7$  Si(111) reconstruction was achieved for a hydrogen terminated surface, LEED was used. Figure 3.13a shows the LEED pattern of a hydrogen terminated Si(111) surface. A hexagonal pattern can be seen which suggests the HF has removed the oxide layer, as the native oxide layer would quench the signal. Comparing to the LEED patterns in Section 3.1, the spots in between is missing in Figure 3.13a, which is due to the hydrogen atoms bonding to the dangling bonds of the Si surface making a  $1 \times 1$  surface more favorable. This also shows successful hydrogen termination of the surface.

Increasing the substrate temperature by thermal annealing was done in order to find the lowest temperature at which a  $7 \times 7$  reconstruction occurs. Figure 3.13b shows a LEED pattern after heating the hydrogen terminated Si surface to  $900^\circ\text{C}$ , which shows the LEED pattern also observed in Section 3.1 proving that reconstruction has happened. Experiments, which will be discussed later, with the first AlN setup have shown that removal of the hydrogen termination was not possible by thermal annealing, indicating that the sample in the AlN setup does not reach  $900^\circ\text{C}$ . Thus it is not possible to create a well-defined surface to grow Al and AlN on, but due to the hydrogen terminated surface being more well-defined than an amorphous native oxide layer, the hydrogen termination method for sample preparation was still used for further experiments.

### 3.7.2 Linear Reflection Measurements

In order to have a second method for checking if a film was forming, linear reflection was utilized. As this method already has been tested and confirmed with the AlN setup, it will be used as a reference point for the nonlinear measurements in order to determine whether a film has grown on the surface. The method lies in using a 633 nm laser, p-polarized, running at 10 mW and a photo-detector to measure the intensity of the reflected light compared to the incident.



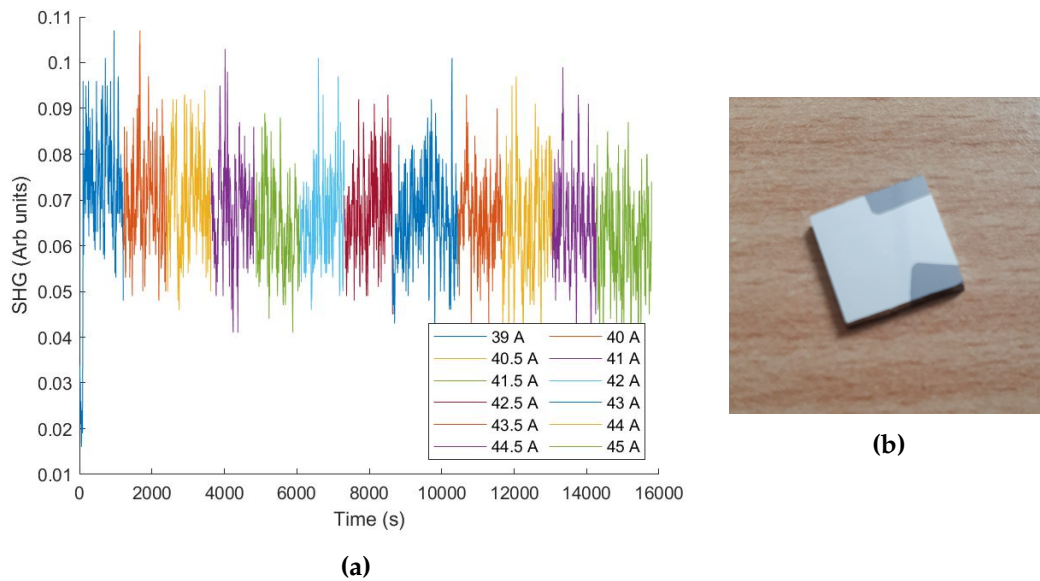
**Figure 3.14:** Linear reflection at 633 nm with a evaporator current of 40.5 A of a) Al deposition on Si. b) AlN deposition on Si with a nitrogen flow of 2 sccm and RF power of 400 W. c) Simulation of p-polarized reflection from different thickness of Al on Si at  $\theta = 10^\circ$  with a wavelength of 633 nm. d) Simulation of p-polarized reflection from different thickness of AlN on Si at  $\theta = 10^\circ$  with a wavelength of 633 nm.

Figure 3.14a shows the intensity spectra during evaporation of Al at 40.5 A. The intensity is starting to increase at around 1000 s, which is the time evaporation started. This increase indicates that the deposited film is Al as it follows the tendency seen in Figure 3.14c. Figure 3.14c shows a simulation of the fraction of light reflected at several different thickness of Al film. This increase in intensity will continue until the Al film is so thick that no transmitted light makes it to the surface. The simulation also indicates that the thickness can be estimated from the increase in reflected light.

Figure 3.14b shows the intensity for AlN evaporation. Here a decrease in the overall intensity is seen. This indicates that the deposited film is AlN, as it follows the tendency depicted in Figure 3.14d. As with Al, an estimation of film thickness should be possible by looking at the changes in reflected light, but instead of go-

ing towards a maximum in reflection, an oscillation would occur. This oscillation comes from the fact that AlN is transparent at 633 nm, leading to thin film interference. This phenomenon occurs when the reflected light from the upper and lower boundaries of a thin film interfere, creating either constructive or destructive interference. This will occur at different thicknesses for different wavelengths. As a clear indication of AlN growth is observed, future experiments will be carried out with gas flow of 2 sccm and RF power of 400 W.

### 3.7.3 In Situ Measurement of Al on Si

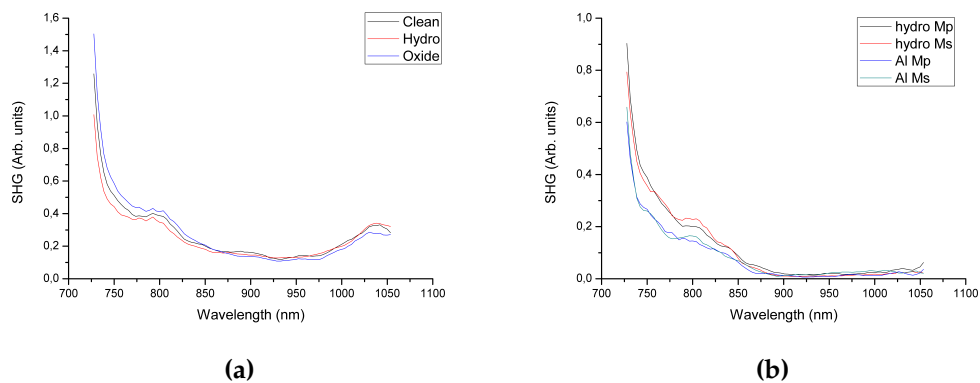


**Figure 3.15:** a) In Situ measurement of Al film growth at 790 nm at  $\theta = 10^\circ$  for varying currents. b) Image of Al film on Si.

Al and Ag are expected to grow similar on Si, as the two metals have similar lattice constants and surface energies. In terms of nonlinear measurement Krause et al. [84] found the SHG intensity of Ag films to be twice the intensity of Al films for 150 nm thick films. This was concluded to be due to the higher reflectivity of Al compared to Ag, thus less signal is actually transmitted through the film in order to generate a signal from the film/substrate interface. Che et al. [31] saw a very similar behavior for Al and Ag for 100 nm films at 10 to 70 mW incident laser power. Pedersen et al. [85] have measured SHG on Al films grown on Si(111) and find similar quantum well effects as with the Ag films on Si(111), so the SHG signal from the Al film is believed to have a similar form to the signal from Ag.

Figure 3.15a shows the SHG intensity as Al is evaporated onto the surface. The different colors correspond to different currents as the current is increased throughout the experiment. Comparing to the linear experiments mentioned in Section 3.7.2, a current of 40.5 A should yield Al evaporation, but no significant change is seen in Figure 3.15a. A small decay is observed over the course of 4.5 hours of experiments. Due to the similarities between Al and Ag, a decay is expected, but at a much faster rate than what is seen in Figure 3.15a. The oscillations with decreasing intensity is the shape expected for Al growth on Si(111), but due to small variation over a bigger time frame, these measurements are unreliable for detecting whether an Al film is grown. Looking at Figure 3.15b, which is an image taken of the sample after taking it out of the setup post deposition, clearly shows Al has evaporated onto the sample. Figure 3.7.3 has a very low signal strength, this is due to loss in the setup and alignment issues. This low signal also gives a worse noise to signal ratio as background noise and artifacts from the equipment may have a larger impact. The SHG data from the Al samples in this setup are insufficient in order to see any growth tendencies.

### 3.7.4 Nonlinear Spectroscopy on Al



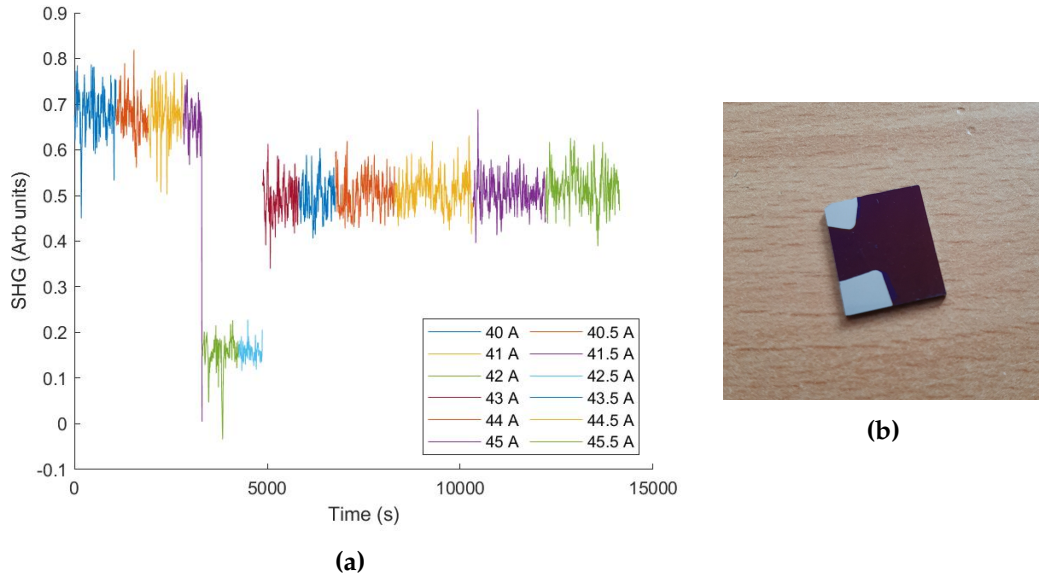
**Figure 3.16:** Spectra for the second harmonic signal intensity from 720 to 1050 nm wavelength for a) *Mm* signal on oxide layer, hydrogen terminated layer and annealed surface at  $\theta = 10^\circ$ . b) *Mp* and *Ms* on hydrogen layer and Al film at  $\theta = 10^\circ$ .

Figure 3.16a shows three different samples, all three being Si substrates with different preparation methods. Spectra measurements were made on the hydrogen terminated sample, a sample with a native oxide layer and a sample attempted heated up to roughly 1100 °C. All three show very similar curves, but with slight differences in intensity. Oxide has shown to introduce more stress to the interface thus potentially yielding higher intensity for the stress induced peak at 730 nm

[73]. The hydrogen terminated surface has the lowest intensity at this wavelength of the three and has also shown to decrease the stress of the system [73]. Looking at the 730 nm peak it could indicate the annealing has successfully cleaned the surface, but this is contradicted by the lack of dangling bonds peaks. The signal from dangling bonds would be expected to increase drastically if the surface was clean, indicating the substrate may not have reached the intended temperature of 1100 °C in order to remove the hydrogen terminated layer. Thus something is still present on the surface. A slight bump can be observed around 800 nm which is most likely an artifact from the laser. An increase in intensity is seen around 1040 nm which is not believed to come from dangling bonds as it is the same for all three samples in which at least two has a known surface not enabling dangling bonds on the Si surface. This could also be a normalization error if the starting point of the spectra for the reference and the measurement is not completely aligned. Since more rapid changes in intensity, can be seen at the end of the spectra for the OPO. This is also believed to be what is happening at the small bump around 800 nm.

Figure 3.16b shows the spectrum for a hydrogen terminated surface and a substrate with an Al film on for  $M_p$  and  $M_s$  polarization. No big difference is seen between  $M_p$  and  $M_s$ , and comparing the hydrogen terminated spectrum to the one in Figure 3.16a, they are very similar. A lower signal is generated from the Al film. This is due to the stress induced peak originating from Si, so applying a metallic film on top would reduce the Si signal, which could indicate some Al growth.

### 3.7.5 In Situ Measurement of AlN on Si



**Figure 3.17:** a) In Situ measurement of AlN film growth at 790 nm at  $\theta = 10^\circ$  for varying currents. b) Image of AlN film on Si measured to be 67 nm.

Figure 3.17a shows the SHG intensity as AlN is grown on the surface, with colors similar to Figure 3.15a. As mentioned a current of 40.5 A should be enough for growth of AlN film, but Figure 3.17a shows no change in intensity with an increase in current during growth. A drop in intensity is seen just prior 5000 seconds stemming from a power outage, which required everything to be turned on again. Due to AlN being non-centrosymmetric in bulk, as mentioned in Section 1.3, the intensity of the signal is expected to grow with increasing film thickness, up to a certain thickness due to phase matching. After four hours of evaporation, no indication can be seen from the SHG data. Comparing to the results of Lin et al. [39], measuring SHG on RF-sputtered AlN films of 220 nm thickness, the SHG intensity for a small incident angle is low to none, depending on the azimuthal angle. Blanc et al. [86] made SHG calculations and measurements on crystalline AlN film grown by magnetron sputtering. Materials with a hexagonal structure, such as AlN, will generate almost no to none intensity at small incident angles. The same can be concluded from Equation 1.14 when the KLC can be applied, since AlN has a bandgap at 200 nm and the measurements were done at 790 nm, it should be a reasonable assumption. Blanc et al. [86] tested the angle dependency for different growth conditions in order to provoke different crystalline orientations, which showed a big change in intensity for the respective incident angles. If the aluminum cathode was to be highly eroded, the growth characteristics would

be modified. For a 3  $\mu\text{m}$  thick film the outer layers would have a different optical axis orientation, which made a small incident angle give the most intensity instead of the lowest. Though, due to the run parameters in this experiments, these is not expected to be the case.

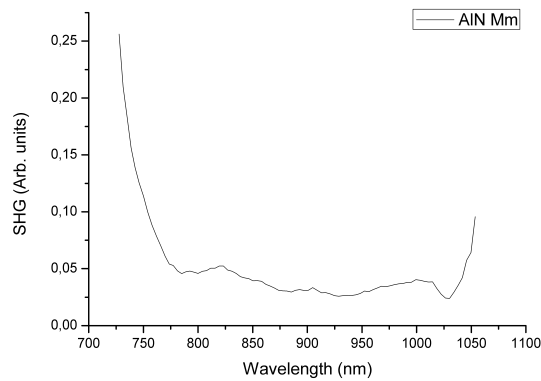


**Figure 3.18:** Nonlinear spectrum measurement on AlN evaporated on Si(111) with  $Mm$  polarization at  $\theta = 10^\circ$ . Evaporated at 40.5 A

Looking at Figure 3.17b, similar to the discussion of in situ Al measurements, the data itself shows no clear indication of evaporation, but the image clearly shows a film is present. The purple-like color also confirms the nitrogen has been successfully cracked in order to create AlN film instead of just evaporating Al. The film was measured to be roughly 67 nm using ellipsometry for the measurement. Though the ellipsometry model was only able to give something close to a fit with a refractive index of 1.85. Usually AlN has a refractive index of 2.1 [36]. This is true for a crystalline AlN film, other works have reported refractive index between 1.8 and 1.9 for amorphous AlN films [36, 87]. Since the film was grown at room temperature and with the earlier indications of lack of proper removal of either hydrogen or an oxide layer, it is plausible the film is indeed amorphous. This could also explain the lack of SHG, as a crystalline structure is required to get a signal. Like with the Al film measurements, the signal to noise ratio may not be good enough for proper tendencies to show, as both the light from the evaporation source and the AC power from the nitrogen source could create noise. It could also be contributed with signal loss from the laser, due to setup geometry.

Figure 3.18 shows a spectrum measured on an AlN film on a Si(111) substrate. A peak can be seen at around 730 nm and an increase in intensity can be seen around 1050 nm wavelength. The first peak is from the Si surface, as mentioned earlier. The intensity compared to the rest of the spectra could be due to increased

stress on the Si surface due to applied AlN film and if small amount of signal is generated from the film due to a small incident angle, as mentioned in Section 3.7.5. Most of the SHG signal generated would originate from the Si/AlN interface. As mentioned above, if the film is amorphous, no SHG signal is expected. The increase around 1050 nm is most likely an error in the normalization at the end of the limits of the OPO, since a film is present and thus no signal is expected to be generated from dangling bonds.

### 3.8 Nonlinear Spectroscopy in Azimuthal Angle Setup.

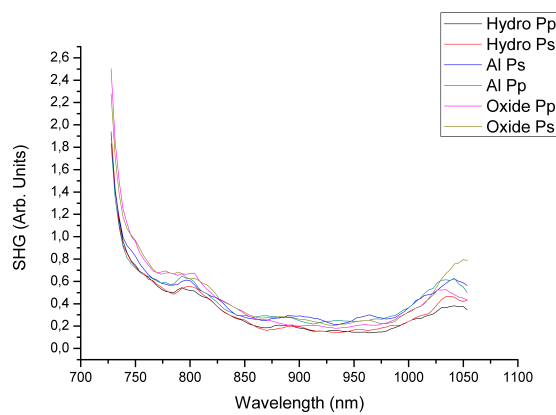


**Figure 3.19:** Spectra for the second harmonic signal intensity from 700 to 1050 nm wavelength for *Pp* and *Ps* on Al film, hydrogen layer and oxide layer at  $\theta = 45^\circ$ .

Figure 3.19 shows spectra for three different surfaces. These measurements were made in the azimuthal setup, thus having an incident angle of  $45^\circ$ . One immediate thing to notice is the higher signal intensity, compared to Figure 3.16, this could partly be due to a larger incident angle, but is probably most dominated by a more simple setup of mirrors and lenses, thus creating less loss. This makes the SHG intensity incomparable between the Figures 3.19 and 3.16, though some similarities are seen. Again no larger difference is seen in either *Pp* or *Ps* polarizations. All curves are very similar to each other and also compared to the spectra in Figure 3.16. The oxide layer has a slightly larger intensity, which could be from the increased stress as explained earlier. While the hydrogen terminated layer has a lower signal and Al lies in the middle. This is opposite compared to Figure 3.16 where the Al layer showed a lower SHG intensity than the hydrogen terminated layer. This could be due to the Al sample used in this setup is different from the one in Figure 3.16, which means it very likely has a different thickness. As mentioned in Section 3.7.3, Al can give similar intensity oscillations as seen in Ag, due to quantum wells, which could explain the difference in intensity compared to the

hydrogen terminated layer. The increase at the end of the spectra and the bump around 800 nm is also visible in Figure 3.19, as in Figure 3.16. This is most likely due to normalization errors, as was most probably the case earlier.

### 3.9 Second AlN Setup

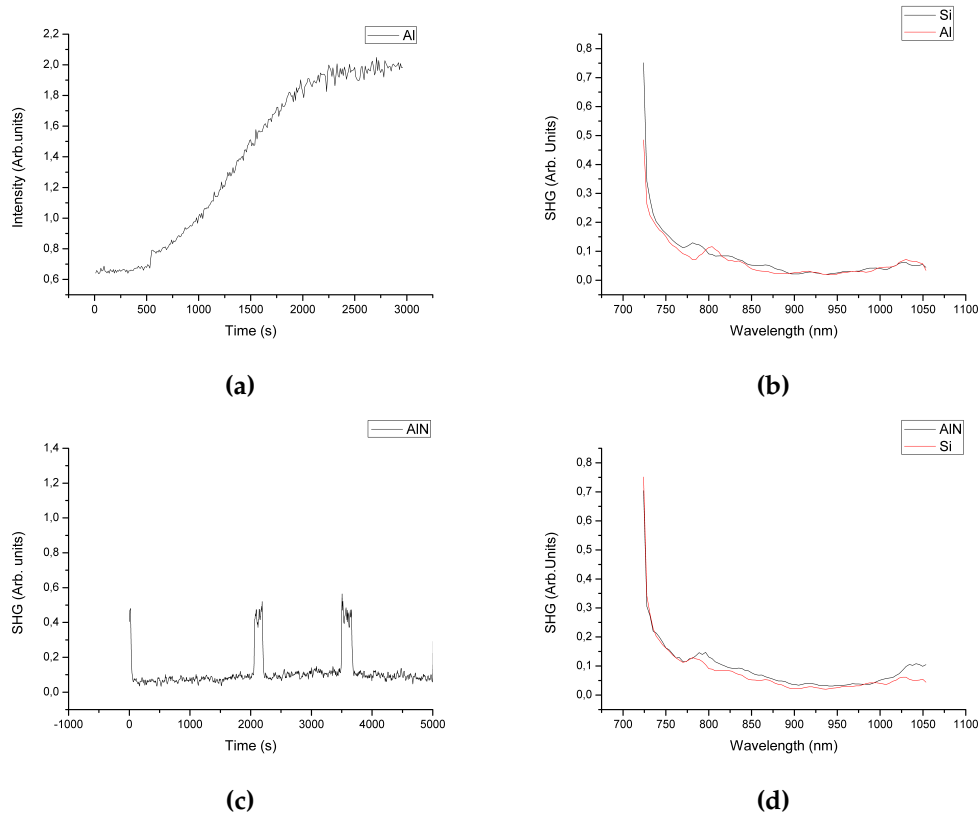


**Figure 3.20:** a) Linear in situ measurement of Al deposition on  $SiO_2$  633 nm. b) Nonlinear spectra of  $SiO_2$  and Al surface 720 to 1050 nm wavelength. c) Nonlinear in situ measurement of AlN on Si 797 nm. d) Nonlinear spectra of Si and AlN surface 720 to 1050 nm wavelength. All measurements had an  $\theta = 45^\circ$  and an evaporation current of 40.5 A for Al.

The purpose of the second iteration of the AlN setup, called the second AlN setup, was to increase the incident angle to  $\theta = 45^\circ$  as mentioned in Section 1.3, as the SHG intensity of a AlN film is very angle dependant. Thus the geometry limitations, in terms of incident angle, from the first AlN setup should not play a factor. Another benefit of the new setup is the improved rail added in order to limit the degrees of freedom for the detection equipment and as such made alignment easier. The added rail also allowed for use of the knife edge method in order to focus the beam on the sample. Though, due to the beam path from the laser, a

signal loss is still expected and it is not possible to set a pure p- or s-polarization for the pump beam without losing even more signal.

First linear measurements were done on Al deposition, in order to make sure an Al film could still be grown at a similar current in the new modified setup. Figure 3.20a shows the reflected intensity over time as Al is evaporated onto the surface. As seen in Section 3.7.2, once again the signal increases to a saturation level, as expected and explained earlier. Thus an Al film can be grown in the new setup.

After growth parameters have been confirmed, nonlinear spectra were measured on SiO<sub>2</sub> and Al in order to compare with previous measurements, which can be seen in Figure 3.20b. Looking at the 730 nm peak a decrease in intensity can be seen on the Al spectra compared to Si, as was seen in Figure 3.16b. This indicates growth of Al on the surface and thus both the linear and nonlinear measurements indicate that an Al film has been grown on the Si surface. Besides the first peak, the two spectra are very similar in curve and intensity. As seen in previous nonlinear spectra measurements using the first AlN setup, no peak can be seen around the 1050 nm wavelength, indicating no dangling bonds.

Figure 3.20c shows nonlinear in situ measurement of AlN deposition on SiO<sub>2</sub>. What may seem odd is the very low intensity measured with a couple of peaks shown. These peaks corresponded with the times at which the Al source were turned off. The explanation lies in an over-saturation of noise for the detector. The PMT is connected to a boxcar which integrates the signal over a designated time in order to differentiate signal from noise, but if noise raises the overall signal level above the integrated area, no signal will effectively be detected by the boxcar. The peaks stem from the signal from the Si surface and some noise from the nitrogen source, but overall the noise to signal ratio is way too low in this measurement to measure in situ growth of AlN with SHG.

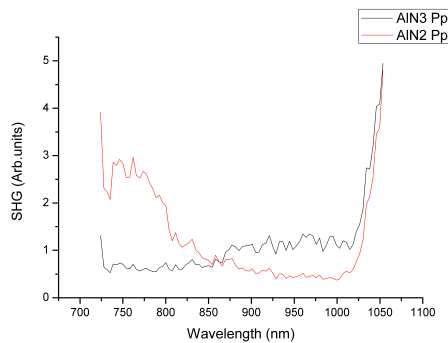
After growth of AlN in the second setup, a nonlinear spectrum measurement was carried out, the spectrum can be seen in Figure 3.20d. No difference can be seen between the AlN and SiO<sub>2</sub> spectra. As the AlN film was grown under the same conditions as those in the first AlN setup, combined with growing on SiO<sub>2</sub> instead of a hydrogen terminated Si surface, the film is most likely amorphous. This is further backed up by ellipsometry measurements made on AlN film grown in the second setup. The measurement showed a thickness of 91 nm and a refractive index of 1.85, though the fit to the model was worse compared to the ellipsometry measurements made on the first AlN film. The refractive index is similar to the measurement made on the previous film grown in the first setup, which indicates that an amorphous AlN film has been grown. This could explain the similarities in the spectra. Furthermore, since an oxide layer is already present on the Si surface,

the Si surface would already be strained and as such, the intensity would already have increased, as seen when depositing a layer on top of a clean Si(111) surface. Also since AlN is a transparent film, only the Si interface would be probed and give a similar signal as is seen in Figure 3.20d. In conclusion for this data, an amorphous AlN film has been grown upon a SiO<sub>2</sub> which yields no difference in the SHG intensity and in order to see a difference, a crystalline AlN film is needed, preferably on a substrate more close to a well-defined crystalline surface, than an amorphous oxide layer.

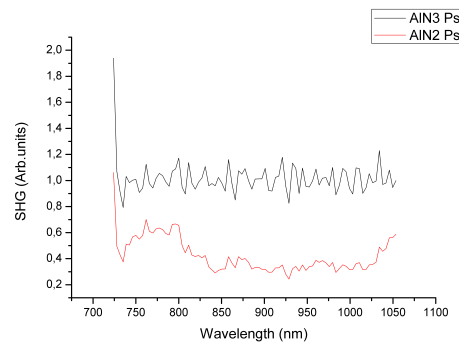
Experiments were made afterward with the Nd:YAG laser on both AlN and Si in the azimuthal angle setup where almost no SHG signal was measured, even though SiO<sub>2</sub> should give a signal as seen in Section 3.2. This could indicate the laser crystal is reaching its lifespan limit and needs to be changed.

### 3.9.1 AlN Growth With Heated Substrate

To investigate the possibility that the first two AlN films grown were amorphous (AlN1 and AlN2), a third film (AlN3) was grown under better conditions, with the substrate heated to 620 °C during the deposition and the Si(111) substrate was hydrogen terminated. The temperature was measured with the pyrometer, as this was now a possibility with the second iteration of the AlN setup. The sample was measured in the azimuthal setup, with both an azimuthal and a spectrum measurement. The second AlN film was measured the same way to see the difference.



(a)



(b)

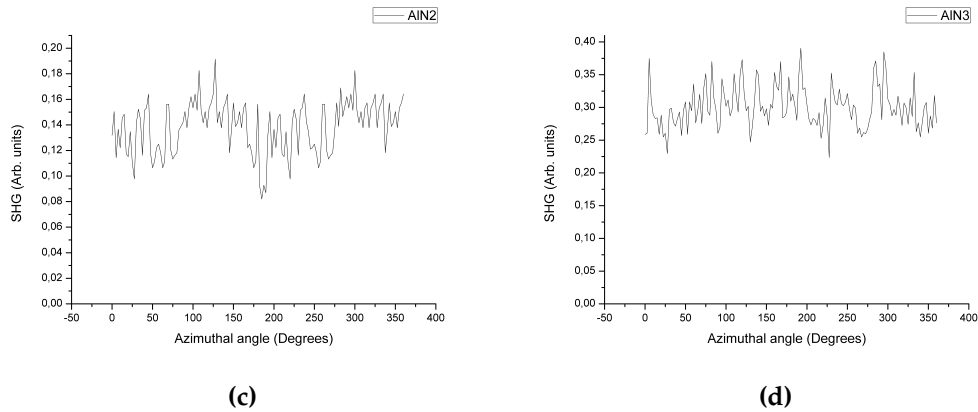


**Figure 3.21:** Nonlinear spectrum of two AlN films grown in the second AlN setup measured in the azimuthal setup at  $\theta = 45^\circ$  with a)  $Pp$  and b)  $Ps$  polarization c) Nonlinear azimuthal angle measurement at  $\theta = 45^\circ$  on AlN film at 830 nm wavelength grown without substrate heating, d) with substrate heating.

Figures 3.21a and 3.21b show nonlinear spectra measurements made on the second and third AlN film. As mentioned in Section 1.3, no  $Ps$  signal is expected to be generated and the SHG intensity should not rely on the azimuthal angle. Figure 3.21b shows the  $Ps$  polarization for the two films and neither show any real tendency with wavelength, except AIN2 has a bump around 750 to 800 nm. The overall lower signal intensity from AIN2 compared to AIN3 could be due to a more amorphous film combined with an oxide layer present prior to growth compared to AIN3 which had a hydrogen terminated surface for growth, as the oxide and amorphous AlN would bury the Si surface. If AIN3 is crystalline it would not generate more signal, but would not decrease the signal at the Si/AlN interface, thus could give a higher intensity in comparison to AIN2. The increase in signal for AIN3 could also be due to the crystalline orientation of AlN, as no signal is expected from  $Ps$  if the AlN film is uniform, but if some domains has another orientation, a  $Ps$  signal could be generated, thus leading to the increase seen. This orientation shift would be visible in an azimuthal measurement, as an orientation generating  $Ps$  signal would depend on the azimuthal angle. The bump mentioned earlier could be from the Si/SiO<sub>2</sub> interface, as oxide have shown to strain the Si and thereby increase the signal from the stress induced peak. This is not present on AIN3, which could be due to a lesser lattice mismatch between AlN and Si if AlN has grown towards a zinc-blende structure, thus introducing less strain on the Si to induce the bandgap peak, as mentioned in Section 1.3. Figure 3.21a shows the  $Pp$  spectra for AIN2 and AIN3. Again a peak can be seen around the 760 nm for AIN2 with a higher intensity compared with the  $Ps$  signal. This is from the Si surface as the oxide gives more strain as mentioned earlier and comparing to Figure 3.3 in Section 3.3, the  $Pp$  showed a larger intensity for this peak than the

$P_s$  signal, which is also apparent in these figures. Comparing the overall intensity seen in Figure 3.21a with Figure 3.19, a clear increase is observed. Both of these measurements were carried out in the azimuthal angle setup, and are thus comparable. This overall increase could indicate the presence of a crystalline AlN film, as its presence would increase the overall SHG signal generated due to its wurtzite structure.

A big increase is seen starting at 1000 nm, which could be a normalization error as mentioned in Section 3.7.5, or it could be leakage of the fundamental wave. This increase has been shown for all nonlinear  $Pp$  spectra measurements on AlN, which indicates a response from the AlN. Also in Figure 3.20d a slight increase can be seen for AlN starting at 1000 nm, thus something could indicate this wavelength has some relation to the AlN film. If this wavelength is correlated with AlN, it would be a suitable wavelength to use for in situ measurements.

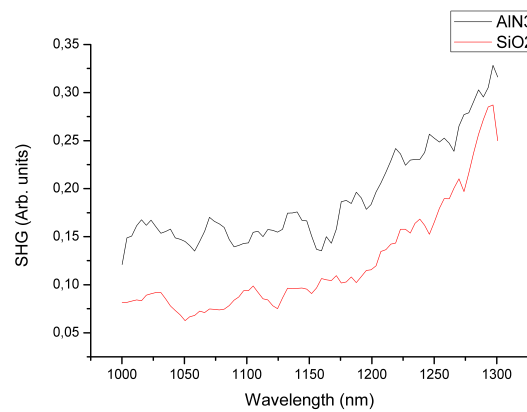


**Figure 3.22:** Nonlinear spectrum measurement for 1000 to 1300 nm at  $\theta = 45^\circ$  with  $Pp$  polarization for AlN3 and SiO2.

Due to the uncertainties behind the intensity increase seen towards the end of the spectra in Figures 3.18, 3.20d, and 1.13, further spectra measurements were done at a new spectrum range of 1000 to 1300 nm. Figure 3.22 shows the new spectra measurements made on SiO2 and AlN3, in which no intensity increase is seen at 1000 nm wavelength. Following the new measurements, the intensity increase is most probable due to limitations from the filter on the PMT used for the original spectra measurements, as the fundamental beam could leak into the detector, if a fault in the filter makes it unable to filter away everything at this wavelength. The signal intensity is expected to be much larger for the fundamental beam than the second harmonic beam and as such, would be able to explain the intensity increase seen. Though the SHG intensity for the AlN film was larger than that of SiO2, which indicates that a crystalline film has formed. As such if the inten-

sity increase was due to the film and not limitations in the setup, it should have shown on the new spectra measurements. An increase can be seen from roughly 1150 nm until the end of the spectra for both AlN3 and SiO2. This is most either from the normalization as the intensity of the reference was decreasing towards the end and as such would increase the total signal after normalization. It could also be an SHG response from the band gap present in Si at around 2.0 eV (620 nm).

The major difference between Figure 3.21c and 3.21d is the intensity. This difference in intensity could be due to two factors, both related to thickness. It could either mean that AlN3 film is thicker than AlN2 generating more signal, or that AlN2 is so thick that the intensity has started oscillating. Ellipsometry measurements show that AlN2 was thicker as it was measured to be 91 nm whereas AlN3 was measured to be 62 nm. A lower signal while having a thicker film could be due to phase matching, as mentioned in Section 1.2.2, since at some thickness the signal would start to decrease again unless a great phase matching is achieved. Though for crystalline AlN, in this wavelength, a coherence length of  $L_{coh} = \frac{830 \text{ nm}}{4(2.19-2.21)} = 4.15 \mu\text{m}$  is expected and thus phase matching should not pose a problem for a sub 100 nm film, even considering the wave has to go through the film twice as it reflects from the AlN/Si interface. The measured refractive index tells another tale, as AlN2 was measured to 1.84 and AlN3 was measured to 2.0. This could indicate that AlN2 is amorphous, but it can be seen in Figure 1.13 and 3.21b that it has the same tendency as AlN3. This could mean that parts of AlN2 are crystalline and other are amorphous, thus leading to an overall thinner crystalline film on AlN2, thus less signal. This indicates that SHG can measure the difference between crystalline and amorphous films.

Figures 3.21c and 3.21d show the azimuthal measurements at 830 nm carried out on the second and third AlN film respectively. Here no real tendency can be seen as a function of the angle, with only slight variations in the intensity measured. This indicates that both the AlN2 and AlN3 have a crystalline structure and are a composite film of Al and N. This is due to the fact that AlN has no dependency of the azimuthal angle as mentioned earlier. Though it is well known the Si(111) surface has an azimuthal angle dependency and would still contribute to the signal, but the signal generated from AlN would quench the azimuthal angle dependency and thus more difficult to see. Looking at Figure 3.21c an oscillation can be seen with a peak at roughly 120°, as seen in Figure 3.2a, which is due to the Si(111) surface. Chen et al. [38] measured a similar quenching of the Si(111) signal when measuring the signal for different azimuthal angles on an AlN film grown on an Si(111) surface for *Pp* and *Ps* polarization. Besides the oscillations from the Si(111), the remaining small variation in signal strength measured in Figure 3.21c and 3.21d, is most likely due to the setup and not a direct effect of the film, as these small fluctuations also can be seen at constant wavelength and angle.

### 3.10 Femtosecond Laser

The experiments carried out mentioned above have been done with the Nd:YAG laser, but a femtosecond laser theoretically should yield better results based on the work by Gielis et al. [33] The efficiency for SHG is based on the number of SHG photons  $S^{2\omega}$  radiated per second. The expression is based on the propagation of radiation in multi-layer systems based on the intensity of the second harmonic signal,

$$S^{2\omega} = \frac{\omega}{\epsilon_0 \hbar c^3 \cos^2 \theta} \frac{P_{av}^2(\omega)}{t_p R_{rep} A_s} \times \left| \sum_L e_L(2\omega) \cdot \chi_L^{(2)}(2\omega) : e_L(\omega) e_L(\omega) \right|^2. \quad (3.1)$$

Here  $P_{av}$  is the average power,  $t_p$  is the pulse duration,  $R_{rep}$  is the repetition rate,  $A_s$  is the irradiated area of the sample,  $\theta$  is the incident angle, and the last squared term refers to the polarization of the incident light and the propagation of the SHG electric field. If comparing the different laser systems under the same conditions such as substrate and film material, film thickness, incident angle, and wavelength, the main difference will lay in  $\frac{P_{av}^2(\omega)}{t_p R_{rep} A_s}$ , which will be denoted as the *LE* (Laser Efficiency) value, where bigger value is better for SHG experiments and due to the femtosecond pulse width, the Sapphire laser would yield more radiated photons even with a higher repetition rate. Calculating the *LE* value for the Nd:YAG laser used in this report yields a value of  $LE = 2000 \text{ W}$ , whereas the sapphire laser has a *LE* value of  $LE \approx 19000 \text{ W}$  with a valued average power of 350 mW. Using the sapphire laser almost radiates 10 times as many SHG photons per second compared to the Nd:YAG laser, which has proved to generate enough photons in order to get a measurable signal, thus the sapphire laser should be viable for SHG experiments. Looking at the much higher repetition rate for the sapphire laser, it should give a better time resolution compared to the Nd:YAG, which in turn should make measurements possible at a higher evaporation rate compared to previous experiments of this report.

Experiments were done with the sapphire laser on an Si(111) sample in the Ag setup. The results can be seen in Table 3.1 showing the number of counts by the PMT for different polarizations of the sapphire laser. The signal strength did not change after a 10 min cooling period post-annealing.

Measurements on the quartz crystal reference gave 24000 counts and background noise corresponded to roughly 1000-2000 counts, thus optimally 10000 counts is needed to have a proper noise to signal ratio. Looking at Table 3.1, after annealing of the Si(111) substrate the p-polarized pump beam was able to generate enough photons for reliable measurement in the Ag setup.

	<b>Polarization</b>	<b>Count</b>
<b>Pre-Annealing</b>	Pm	8000
	Sm	5000
<b>Post-Annealing</b>	Pm	10000
	Sm	5000

**Table 3.1:** Photon counts using a PMT set to 2300 V on a Si(111) surface with a native oxide layer and after annealing at 15 A, for *Pm* and *Sm* polarizations.

### 3.11 Obstacles and Experiences

Through this project, many obstacles have proven time-consuming to overcome, but have given some experience, which is worthwhile noting for future work. Even though this is not the first time the authors of this report has worked with vacuum, some new experiences came along. When baking a vacuum chamber it is important to make sure all bolts are properly greased, so they won't get stuck and make opening the chamber that much more difficult. Another factor is double checking the wiring for components inside the chamber, as the soldering of the wire on the back of the quartz crystal would be damaged by continuous baking of the chamber. Another optimization for the Ag chamber would be to implement a load lock, as every time the sample had to be changed, the entire chamber had to be opened up, which meant several days of pumping and baking in order to get sufficient pressure, only to end up with leaks and leak checking for some time, due to the pressure being higher than expected after a certain amount of pumping time.

Due to the sensitivity of the detection equipment for SHG, every experiment had to be conducted in total darkness in order to not create too much noise compared to the signal, or completely drown the PMT. Many problems occurring from noise was attempted to be fixed with cardboard and tape to close off any unnecessary light sources such as equipment and the evaporator. When doing in situ measurements usually a very well-defined wavelength is used and as such the SH wavelength is well known. Therefore, more precise filters could be used in order to improve the signal to noise ratio. Since neither of the AlN setups used in this project had any kind of way for measuring the flux of the evaporated material, the run conditions were based on past experiences, which required time in order to get a better grasp of how the deposition parameters affected the film and even at what currents Al would start to evaporate.

Later experiments have shown a lack of crystallinity in the AlN film which imposes a clear problem for SHG, which could have been overcome with a well-defined surface and substrate heating during growth. The geometry of the first

AlN setup made it difficult to reliably measure the temperature of the substrate, thus it was based on past experiences whether the temperatures for substrate cleaning was reached.

Working with crystalline AlN also created certain complications, as no articles were found that measured the SHG response of AlN in the spectrum used in this report. This means no easy comparison for the results gathered on AlN were found by the authors. This problem could be overcome by having a well defined AlN crystal, as it would be possible to get the SHG response, both as a function of wavelength and orientation. Thus allowing for comparisons with the grown AlN films.

Due to artifacts from the laser, it is important to normalize all data to a reference. A quartz crystal was used as a reference in this report. The wavelength of the OPO might have slightly changed during or between measurements, thus creating references for each measurement is preferred. This was not possible in the AlN setups and thus some artifacts still remain. Having a way to make a reference for each measurement, no matter what setups were used, would make the data more telling in terms of actual tendencies from the samples and not just artifacts from the equipment. The second iteration of the AlN setup contained a rail for mounting lenses and mirrors. Though the design proved slightly flawed as the entire rail rather easily started to vibrate which is unfavorable when working with high precision. This meant great care had to be taken when moving around the setup, while adjusting or during measurements in order to avoid inducing vibrations in the rail. Finally, keeping a log over the laser use would prove beneficial as the Nd:YAG crystal wears over time during its lifespan and the efficiency decreases. The remaining lifespan is easier to predict if keeping a log over the use as a preset amount of use is listed by the manufacturer.



## Chapter 4

# Conclusion

The goal of this project was to investigate the possibility of using second harmonic generation for in situ measurements on thin films, with a primary focus on measuring thickness and crystallinity.

Firstly, Si(111) substrates with different surface morphology can be characterized utilizing SHG, as clean Si(111), SiO<sub>2</sub>, and hydrogen terminated Si have shown to yield different signal intensities, both when a scanning over a range of wavelengths and for different azimuthal angles. On a clean Si(111) surface, dangling bonds can be observed as peaks at 950 nm or 1050 nm in the *Ps* signal, and will vanish as soon as the surface undergoes changes and something binds to the surface. A difference can also be seen between Si(111), Si/SiO<sub>2</sub>, and hydrogen terminated surfaces at 730 nm, as they each induce different amounts of strain, leading to different intensities in the SHG signal, with the highest intensity from Si/SiO<sub>2</sub> interface, as it produces the most strain.

Secondly, SHG can indubitably be utilized as an in situ measurement of thickness for metallic films. This is due to the quantum wells phenomenon, as seen in Ag and Al, as the signal will oscillate as a function of the thickness. These oscillations occur due to certain film thickness being able to support standing waves, depending on the wavelength. These oscillations are very thickness specific and are showing for both in situ measurements and measurements carried out after the film is grown. Thus leading to a precise method for measuring the thickness of metallic films for the first 10 nm for Ag. Thicker films are problematic for this kind of thickness measurements as almost all the light propagating through the film will be absorbed.

Lastly, this report has shown SHG can be used to characterize a non-centrosymmetric crystal with a wurtzite structure, such as AlN. Comparing the *Pp* and *Ps* signal for

an AlN film, only changes in  $Pp$  is expected for a crystalline film and thus SHG can be used as a method for measuring the crystallinity of wurtzite films like AlN. This could be expanded to include other crystalline structures depending on how the individual  $d_{eff}$  is dependant on polarization, incident angle, and azimuthal angle. No SHG signal is generated from amorphous materials, as an optical axis is needed to create a change in polarization, meaning it can be used to distinguish between crystalline and amorphous films or a combination of both. Comparing this method to linear measurements which are only able to indicate the thickness of the film, independent of crystallinity. A suitable wavelength usable for in situ measurements, when using Si as a substrate, is at 750 nm, as a change in intensity is observed at this wavelength if inconsistencies occur in the film. This SH peak is related to Si and as such can be used to probe modifications on the Si surface compared to a clean Si surface. AlN has a bandgap at 200 nm and as such, most wavelengths above 400 nm are suitable for in situ SHG measurements.

In conclusion, SHG has shown to be a very sensitive method for probing surfaces, interfaces, and thin films. By varying the incident angle, the azimuthal angle, the beam polarization, and comparing to other experiments, information about thickness and crystallinity is able to be gathered. Further work developing theoretical models, considering the susceptibility tensors for different crystal structures, can be used for comparison with experimental data to give a more complete understanding.

## Chapter 5

# Outlook

### 5.1 Model of SHG Setup

One of the thoughts going into this project was to be able to use in situ measurements utilizing SHG in an industrial setting to make a real-time method for quality testing thin films. With that in mind, a prototype was designed based on the experiences made by the authors. This prototype builds upon a combination of already existing techniques and results from this report in order to optimize the process. These optimizations include things like a compact design, cost of the added modules, and the ability to tune and change the parameters of the measurements carried out on the sample. All this led to a design that will be presented and the decisions behind it explained in this chapter.

Figure 5.1 shows a schematic model made using Autodesk Inventor software. The model is made as a theoretical setup for SHG to be used in an industrial setting. Figure 5.1a shows the entire setup, where dimensions and overall design are roughly based on the modular setups used by Polyteknik A/S, with a main chamber containing the sample holder, a top part with the sputtering source, and a bottom part containing the pumping system.

The main chamber, highlighted with a yellow box in Figure 5.1a, has no direct changes, except holes for attachment of the windows seen in Figure 5.1d. These windows are offset from the chamber walls and are facing upwards to avoid evaporation on the glass to avoid blocking the laser. This would also work if the sample and evaporator switch's places, as some process run this way, by flipping the orientation making the glass point downwards.

Due to the light contamination sensitivity, as seen throughout the experiments in this report, the side attachments, called wings, seen in Figures 5.1b and 5.1c are concealed to the outside, to avoid light contamination from outside sources. The

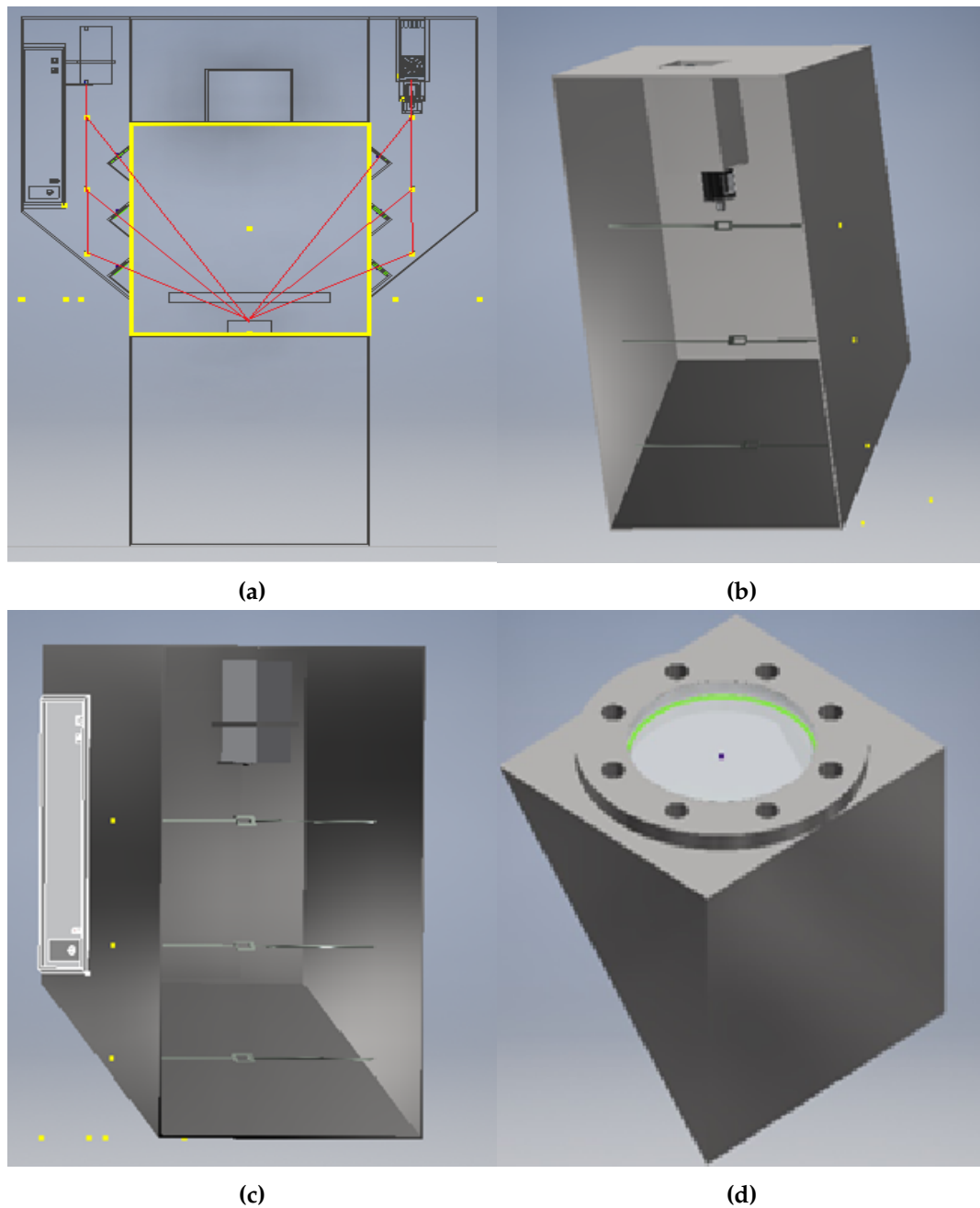


**Figure 5.1:** Model of industrial SHG setup made in Inventor. a) Main chamber with the different light paths . b) Right wing. c) Left wing. d) Window

wings also serve the purpose of making the SHG addition to the chamber as compact as possible, by having everything required present on the sides of the main chamber.

The right wing, seen in Figure 5.1b, contains a PMT detector, a polarizer controlled by a stepper motor and a filter which can be changed depending on the wavelength of the incoming SHG signal. Both the polarizer and the stepper motor can be controlled while the wing is sealed, but the filter can only be changed by opening the wing. The left wing, seen in Figure 5.1c, contains the fiber laser and its power supply and a Mounted Achromatic Wave Plate. The power supply and controls of the laser can be accessed with the wing closed as it is built into the side of the wing. The mounted achromatic wave plate can also be controlled by a stepper motor and controls the polarization of the fiber laser, making it possible to scan with both p- and s-polarized light.

Both the wings have three mirrors controlled by a sliding mechanism altering the path of the light. The sliding mechanism has two possible positions, either *on* or *off*. Here *on* is when the mirror is directly in front of the beam, and *off* is when the gap in the rod is in front of the beam thus allowing the beam to reach the next mirror. This mechanism is shown in Figure 5.2. These mirrors are aligned and angled with the windows on the main chamber and all focus down on the same point, the center of the substrate holder, thus allowing for up to three different incident angles at  $23^\circ$ ,  $45^\circ$  and  $63^\circ$ , as this range of angles has been found to be most optimal for SHG measurements.

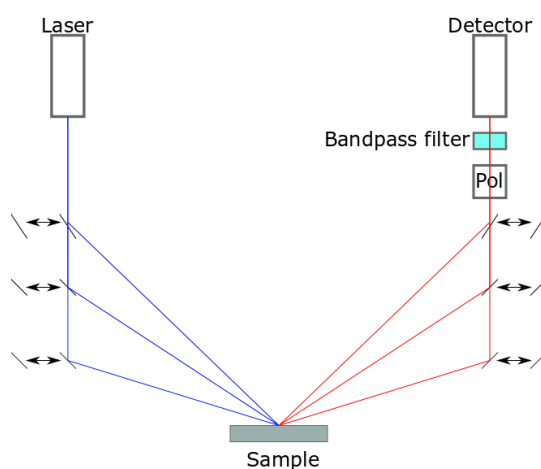
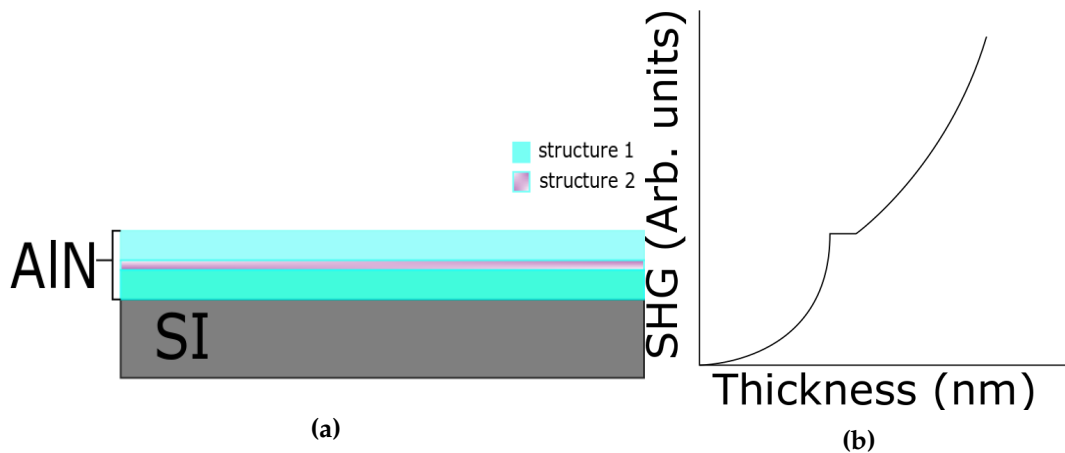


Figure 5.2: Schematic showing the optical arrangement in the industrial setup.

The different apertures were selected based on price and compatibility. The FP200 fiber laser in the prototype has a wavelength of 1064 nm and  $LE = 2500$  which is higher than the Nd:YAG and thus should be sufficient for SHG while still being capable of outputting a repetition rate of 1 MHz. This is then paired with a FL05532-10 bandpass filter with a center wavelength of 532 nm to only allowing the

SHG wave to pass. The detector chosen is a PicoQuant PMA Photon Counting, as it can handle up to 80 MHz, and works within the desired wavelength. All product details can be seen in Appendix C. One of the big differences between industry and a lab environment is the evaporation rate, as epitaxial growth is nowhere near fast enough in order to produce a sufficient amount of thin films and often sputtering is the main deposition method chosen. As seen in Section 3.6.1, a high evaporation rate diminishes the data gathering using the Nd:YAG laser, but theoretically a higher repetition rate should better this problem, which is why having a MHz repetition rate was one of the criteria for the laser chosen for the prototype. Another big difference is the working pressure, as inert gasses are used in industry to create plasma when using techniques such as magnetron sputtering. Literature often recommends UHV when working with SHG, which is mostly due to the surface sensitivity of the SHG intensity and thus a minimum of contamination is preferred. The base pressure in most industrial setups is actually very low and starts increasing when introducing other gasses into the chamber, which should not have a big impact on SHG. This is a big advantage of using SHG as a probing method compared to LEED.



**Figure 5.3:** Illustration of a) a AlN film with a structure variation and b) the SHG response to this change.

In order to use SHG for precise measurement of film crystallinity and quality, a theoretical model has to be made, which can be fitted to the data in order to extract values. As theoretical modeling was not the main focus of this project, it has not been further investigated, but a way to check the uniformity of the film during growth could be done without any theoretical model. AlN and gallium nitride (GaN) films are non-centrosymmetric and of the wurtzite structure, thus is expected to behave similarly in the SHG intensity. For these thin films, the intensity should increase quadratically as mentioned in Section 1.3, but if at some

point during growth, the structure is changed, there should be anomalies in the measurement which would correspond to a point of nonuniformity in the film. An illustration can be seen in Figure 5.3 to give an example of what this could look like. Another way to use SHG for measurements without extensive theoretical models is by using it for thickness measurements of metallic films. As seen in Section 3.6, the SHG signal will oscillate with the thickness due to quantum well effects and these oscillations correspond to specific thicknesses depending on the wavelength and material. Though it is important to note these quantum well effects will only appear for very thin films. Pedersen et al. [71, 85] have shown oscillations up to 40 ML (10 nm) for Ag and 20 ML (5 nm) for Al.

## 5.2 Methods for Comparison of SHG Measurements

Examples of other methods which could be used for quality checking of thin films and measuring the crystallinity are Raman spectroscopy, Reflection high-energy electron diffraction (RHEED) and X-ray diffraction (XRD). RHEED is similar to LEED except it uses higher energy electrons and a large incident angle relative to the surface normal. Since RHEED uses electrons and not a light source, it is not possible to probe an entire thin film, depending on the thickness. The pressure requirements make it unable to do in situ measurements unless the film is grown epitaxial. For sputtering of nitride films, the working pressure would be too high for RHEED. [88]

XRD can be used for general characterization of crystalline materials. XRD bombards a material surface with x-rays in order to dislodge electrons from the inner shells of the material in question. The energy and angle required for this can be used to gain information about the medium, utilizing Braggs law [30]. Using XRD for measurements requires a lot more room for the detector, as it needs to be movable, compared to RHEED, LEED, and SHG which all have stationary detectors. XRD excels at measuring unknown crystalline materials, but often when making a thin film, the composition is already known. Though in case of composite films, such as nitride films, it is not given that the nitrogen has been cracked properly in order to make atomic nitrogen for the film. [89]

Raman spectroscopy is a method for analyzing vibrational states in a medium. Raman spectroscopy utilizes inelastic scattering, also known as Raman scattering. Photons are able to excite electrons in a medium to a higher energy state and the afterwards emitted photon is of another, often lower, energy due to some of the energy exciting phonons in the medium. This shift in wavelength can be used to very precisely determine the medium, as the vibrational modes from the chemical bonds are very material dependant. This can also be used to measure the crystalline orientation, by looking at the polarization of the outgoing photon compared

Group 5.326A

CHAPTER 5. OUTLOOK

to the incident. [90]

# Bibliography

- [1] H. Lüth, *Solid Surfaces, Interfaces and Thin Films*. Springer, 5 ed., 2015.
- [2] C. Duquenne, M. P. Besland, P. Y. Tessier, E. Gautron, Y. Scudeller, and D. Averty, "Thermal conductivity of aluminium nitride thin films prepared by reactive magnetron sputtering," *Journal of Physics D: Applied Physics*, vol. 45, p. 015301, 1 2012.
- [3] H. Frey and H. R. Khan, *Handbook of Thin-Film Technology*. Berlin, Heidelberg: Springer Berlin Heidelberg, 2015.
- [4] R. W. Boyd, *Nonlinear optics*. New York: Academic Press, 3 ed., 2008.
- [5] Kerr J., "A new relation between electricity and light: Dielectric media birifrige," *Phil. Mag*, vol. 4,, pp. 337–348, 11 1875.
- [6] G. New, *Introduction to Nonlinear Optics*. Cambridge: Cambridge University Press, 1 ed., 2011.
- [7] P. A. Franken, A. E. Hill, C. W. Peters, and G. Weinreich, "Generation of Optical Harmonics," *Physical Review Letters*, vol. 7, pp. 118–119, 8 1961.
- [8] Y. R. Shen, "Surface nonlinear optics: A historical perspective," *IEEE Journal on Selected Topics in Quantum Electronics*, vol. 6, pp. 1375–1379, 11 2000.
- [9] J. A. Armstrong, N. Bloembergen, J. Ducuing, and P. S. Pershan, "Interactions between light waves in a nonlinear dielectric," *Physical Review*, vol. 127, pp. 1918–1939, 9 1962.
- [10] N. Bloembergen and P. S. Pershan, "Light waves at the boundary of nonlinear media," *Physical Review*, vol. 128, pp. 606–622, 10 1962.
- [11] J. Ducuing and N. Bloembergen, "Observation of reflected light harmonics at the boundary of piezoelectric crystals," *Physical Review Letters*, vol. 10, pp. 474–476, 6 1963.

- [12] F. Brown, R. E. Parks, and A. M. Sleeper, "Nonlinear optical reflection from a metallic boundary," *Physical Review Letters*, vol. 14, pp. 1029–1031, 6 1965.
- [13] E. Garmire, "Nonlinear optics in daily life," *Optics Express*, vol. 21, no. 25, 2013.
- [14] D. S. Bhatkhande, V. G. Pangarkar, and A. A. Beenackers, "Photocatalytic degradation for environmental applications - A review," 1 2002.
- [15] H. W. Paerl, P. T. Bland, N. D. Bowles, and M. E. Haibach, "Adaptation to High-Intensity, Low-Wavelength Light among Surface Blooms of the Cyanobacterium *Microcystis aeruginosa*," *Applied and environmental microbiology*, vol. 49, pp. 1046–52, 5 1985.
- [16] G. Tallents, E. Wagenaars, and G. Pert, "Optical lithography: Lithography at EUV wavelengths," *Nature Photonics*, vol. 4, pp. 809–811, 12 2010.
- [17] P. Campagnola, "Second harmonic generation imaging microscopy: Applications to diseases diagnostics," *Analytical Chemistry*, vol. 83, pp. 3224–3231, 5 2011.
- [18] H. Hu, K. Wang, H. Long, W. Liu, B. Wang, and P. Lu, "Precise determination of the crystallographic orientations in single ZnS nanowires by second-harmonic generation microscopy," *Nano Letters*, vol. 15, pp. 3351–3357, 5 2015.
- [19] M. J. d. Dood, "Second-harmonic generation," *Huygens Laboratorium*, 2006.
- [20] N. M. Terlinden, *Second-harmonic generation spectroscopy for interface studies of dielectric thin films on silicon*. Eindhoven: Technische Universiteit Eindhoven, 2012.
- [21] D. A. Kleinman, "Nonlinear Dielectric Polarization in Optical Media," *Physical Review*, vol. 126, pp. 1977–1979, 6 1962.
- [22] P. W. Milonni and J. H. Eberly, *Lasers*. New York: Wiley, 1988.
- [23] J. E. Sipe, D. J. Moss, and H. M. Van Driel, "Phenomenological theory of optical second- and third-harmonic generation from cubic centrosymmetric crystals," *Physical Review B*, vol. 35, pp. 1129–1141, 1 1987.
- [24] D. Sands, *Introduction to crystallography*. New York: Dover, 1 ed., 1993.
- [25] F. Jona, J. A. Strozier, and W. S. Yang, "Low-energy electron diffraction for surface structure analysis," *Reports on Progress in Physics*, vol. 45, pp. 527–585, 5 1982.

- [26] T. F. Heinz, M. M. T. Loy, and W. A. Thompson, "Study of symmetry and disordering of Si(111)-7x7 surfaces by optical second harmonic generation," *Journal of Vacuum Science & Technology B: Microelectronics and Nanometer Structures*, vol. 3, p. 1467, 9 1985.
- [27] V. Mizrahi and J. E. Sipe, "Phenomenological treatment of surface second-harmonic generation," *Journal of the Optical Society of America B*, vol. 5, no. 3, pp. 660–667, 1988.
- [28] P. Guyot-Sionnest, W. Chen, and Y. R. Shen, "General considerations on optical second-harmonic generation from surfaces and interfaces," *Physical Review B*, vol. 33, pp. 8254–8263, 6 1986.
- [29] H. W. K. Tom, T. F. Heinz, and Y. R. Shen, "Second-harmonic reflection from silicon surfaces and its relation to structural symmetry," *Physical Review Letters*, vol. 51, pp. 1983–1986, 11 1983.
- [30] C. Kittel, *Introduction to solid state physics*. Wiley, 8 ed., 2005.
- [31] F. Che, S. Grabtchak, W. M. Whelan, S. A. Ponomarenko, and M. Cada, "Relative SHG measurements of metal thin films: Gold, silver, aluminum, cobalt, chromium, germanium, nickel, antimony, titanium, titanium nitride, tungsten, zinc, silicon and indium tin oxide," *Results in Physics*, vol. 7, pp. 593–595, 2017.
- [32] G. I. Stegeman and R. A. Stegeman, *Nonlinear Optics: Phenomena, Materials and Devices*. Wiley, 2012.
- [33] J. J. H. Gielis, P. M. Gevers, I. M. P. Aarts, M. C. M. van de Sanden, and W. M. M. Kessels, "Optical second-harmonic generation in thin film systems," *Journal of Vacuum Science & Technology A: Vacuum, Surfaces, and Films*, vol. 26, no. 6, pp. 1519–1537, 2008.
- [34] K. Dovidenko, S. Oktyabrsky, J. Narayan, and M. Razeghi, "Aluminum nitride films on different orientations of sapphire and silicon," *Journal of Applied Physics*, vol. 79, pp. 2439–2445, 3 1996.
- [35] T. Koppe, H. Hofsäss, and U. Vetter, "Overview of band-edge and defect related luminescence in aluminum nitride," 10 2016.
- [36] H. Morkoç, *Handbook of Nitride Semiconductors and Devices*, vol. 1. Wiley-VCH, 2009.
- [37] W. Class, "AN ALUMINUM NITRIDE MELTING TECHNIQUE," tech. rep., NASA Report CR-1171, 1968.

- [38] C. S. Chen, J. T. Lue, C. L. Wu, S. Gwo, and K. Y. Lo, "A study of surface and interlayer structures of epitaxially grown group-III nitride compound films on Si(111) substrates by second-harmonic generation," *Journal of Physics Condensed Matter*, vol. 15, pp. 6537–6548, 10 2003.
- [39] W. P. Lin, P. M. Lundquist, G. K. Wong, E. D. Rippert, and J. B. Ketterson, "Second order optical nonlinearities of radio frequency sputter-deposited AlN thin films," *Applied Physics Letters*, vol. 63, pp. 2875–2877, 11 1993.
- [40] M. C. Larciprete, A. Bosco, A. Belardini, R. Li Voti, G. Leahu, C. Sibilìa, E. Fazio, R. Ostuni, M. Bertolotti, A. Passaseo, B. Potì, and Z. Del Prete, "Blue second harmonic generation from aluminum nitride films deposited onto silicon by sputtering technique," *Journal of Applied Physics*, vol. 100, p. 023507, 7 2006.
- [41] D. Blanc, A. Cachard, and J.-C. Pommier, "All-optical probing of material structure by second-harmonic generation: application to piezoelectric aluminum nitride thin films," *Opt. Eng.*, vol. 36, no. 4, pp. 1191–1195, 1997.
- [42] S. A. Kukushkin, A. V. Osipov, V. N. Bessolov, B. K. Medvedev, V. K. Nevolin, and K. A. Tcarik, "SUBSTRATES FOR EPITAXY OF GALLIUM NITRIDE: NEW MATERIALS AND TECHNIQUES," tech. rep., 2008.
- [43] T. F. Heinz, M. M. T. Loy, and W. A. Thompson, "Study of Si(111) surfaces by optical second-harmonic generation: Reconstruction and surface phase transformation," *Physical Review Letters*, vol. 54, pp. 63–66, 1 1985.
- [44] M. Morita, T. Ohmi, E. Hasegawa, M. Kawakami, and M. Ohwada, "Growth of native oxide on a silicon surface," *Journal of Applied Physics*, vol. 68, pp. 1272–1281, 8 1990.
- [45] G. E. Becker and J. C. Bean, "Acceptor dopants in silicon molecular-beam epitaxy," *Journal of Applied Physics*, vol. 48, pp. 3395–3399, 8 1977.
- [46] A. Ishizaka, "Low Temperature Surface Cleaning of Silicon and Its Application to Silicon MBE," *Journal of The Electrochemical Society*, vol. 133, p. 666, 4 2006.
- [47] J. F. McGilp, "Determining metal-semiconductor interface structure by optical second-harmonic generation," *Semiconductor Science and Technology*, vol. 2, pp. 102–107, 2 1987.
- [48] G. Reider and T. Heinz, "Second-order Nonlinear Optical Effects at Surfaces and Interfaces: Recent Advances," in *Photonic Probes of Surfaces* (P. Halevi, ed.), vol. 2, ch. 9, pp. 413–478, Elsevier, 1995.

- [49] D. B. Fenner, D. K. Biegelsen, and R. D. Bringans, "Silicon surface passivation by hydrogen termination: A comparative study of preparation methods," *Journal of Applied Physics*, vol. 66, pp. 419–424, 7 1989.
- [50] L. Bell, T. Lin, R. Fathauer, P. Grunthner, F. Schowengerdt, W. Kaiser, J. Mazur, M. Hecht, and F. Grunthner, "Hydrogen-terminated silicon substrates for low-temperature molecular beam epitaxy," *Thin Solid Films*, vol. 183, pp. 197–212, 12 2002.
- [51] G. Meyer and K. H. Rieder, "Low temperature STM study on the growth of ultrathin Ag films on Si(111)7x7," *Surface Science*, vol. 331-333, pp. 600–605, 7 1995.
- [52] E. J. Van Loenen, M. Iwami, R. M. Tromp, and J. F. Van Der Veen, "The adsorption of Ag on the Si(111) 7x7 surface at room temperature studied by medium energy ion scattering, LEED and AES," *Surface Science*, vol. 137, pp. 1–22, 2 1984.
- [53] M. A. M. A. Van Hove, W. H. W. H. Weinberg, and C.-M. C.-M. Chan, *Low-energy electron diffraction : experiment, theory, and surface structure determination*. Berlin, Heidelberg: Springer-Verlag, 1 ed., 1986.
- [54] M. Ebrahimzadeh, "Parametric light generation," *Philosophical Transactions of the Royal Society A: Mathematical, Physical and Engineering Sciences*, vol. 361, pp. 2731–2750, 12 2003.
- [55] J. Hecht, *The Laser Guidebook*. McGraw-Hill Professional Publishing, 2 ed., 1999.
- [56] D. M. Hoffman, B. Singh, and J. H. Thomas, *Handbook of vacuum science and technology*. Academic Press, 1 ed., 1998.
- [57] W. Umrath, H. Adam†, A. Bolz, H. Boy, H. Dohmen, K. Gogol, W. Jorisch, W. Mönning, H.-J. Mundinger, H.-D. Otten, H. S. Willi Scheer, W. Schwarz, K. Stepputat, D. Urban, H.-J. Wirtzfeld, and H.-J. Zenker, "Fundamentals of vacuum Technology," *Products and References Book Leybold Vacuum*, 2007.
- [58] A. Penzkofer, "Solid state lasers," 1 1988.
- [59] J. R. Lakowicz, *Principles of fluorescence spectroscopy*. Springer, 3 ed., 2006.
- [60] R. J. Blume, "'Boxcar' integrator with long holding times," *Review of Scientific Instruments*, vol. 32, no. 9, pp. 1016–1018, 1961.
- [61] W. E. Hoke, P. J. Lemonias, and D. G. Weir, "Evaluation of a new plasma source for molecular beam epitaxial growth of InN and GaN films," *Journal of Crystal Growth*, vol. 111, pp. 1024–1028, 5 1991.

- [62] J. M. Van Hove, G. J. Cosimini, E. Nelson, A. M. Wowchak, and P. P. Chow, "GaN growth by a controllable RF-excited nitrogen source," *Journal of Crystal Growth*, vol. 150, pp. 908–911, 5 1995.
- [63] G. Binnig, C. F. Quate, and C. Gerber, "Atomic Force Microscope," *Physical Review Letters*, vol. 56, pp. 930–933, 3 1986.
- [64] H. Fujiwara and Wiley InterScience (Online service), *Spectroscopic Ellipsometry : Principles and Applications*. John Wiley & Sons, 2007.
- [65] M. Saitoh, F. Shoji, K. Oura, and T. Hanawa, "Initial growth process and surface structure of Ag on Si(111) studied by low-energy Ion-Scattering Spectroscopy (ISS) and LEED-AES," *Surface Science*, vol. 112, pp. 306–324, 12 1981.
- [66] G. H. Lu, M. Huang, M. Cuma, and F. Liu, "Relative stability of Si surfaces: A first-principles study," *Surface Science*, vol. 588, pp. 61–70, 8 2005.
- [67] F. Rollert, N. A. Stolwijk, and H. Mehrer, "Solubility, diffusion and thermodynamic properties of silver in silicon," *Journal of Physics D: Applied Physics*, vol. 20, pp. 1148–1155, 9 1987.
- [68] K. Pedersen and P. Morgen, "Dispersion of optical second-harmonic generation from Si(111)7x7," *Physical Review B*, vol. 52, pp. R2277–R2280, 7 1995.
- [69] K. Pedersen and P. Morgen, "Dispersion of optical second-harmonic generation of Si(111) 7x7 during oxygen adsorption," *Physical Review B - Condensed Matter and Materials Physics*, vol. 53, pp. 9544–9547, 4 1996.
- [70] K. Pedersen and P. Morgen, "Optical second-harmonic generation spectroscopy on Si(111)7x7," *Surface Science*, vol. 377-379, pp. 393–397, 4 1997.
- [71] K. Pedersen, T. G. Pedersen, and P. Morgen, "Surface and interface resonances in second harmonic generation from metallic quantum wells on Si(111)," *Physical Review B - Condensed Matter and Materials Physics*, vol. 73, p. 125440, 3 2006.
- [72] D. Milovzorov, "Nonlinear Optoelectronic Devices Based on Nanocrystalline Silicon Films: Acoustoelectrical Switches for Optical Modes, Nonlinear Optical Switches and," in *Nanocrystal* (Y. Masuda, ed.), ch. 18, pp. 460–494, InTech, 6 2011.
- [73] W. Daum, H. J. Krause, U. Reichel, and H. Ibach, "Identification of strained silicon layers at Si-SiO<sub>2</sub> interfaces and clean Si surfaces by nonlinear optical spectroscopy," *Physical Review Letters*, vol. 71, pp. 1234–1237, 8 1993.
- [74] K. Pedersen and P. Morgen, "Second-harmonic generation spectroscopy on reconstructed Si(111) surfaces," in *Physica Status Solidi C: Conferences*, vol. 0, pp. 3065–3069, John Wiley & Sons, Ltd, 12 2003.

- [75] U. Höfer, "Nonlinear optical investigations of the dynamics of hydrogen interaction with silicon surfaces," *Applied Physics A: Materials Science and Processing*, vol. 63, pp. 533–547, 12 1996.
- [76] H.-J. Butt, K. Graf, and M. Kappl, *Physics and Chemistry of Interfaces*. Weinheim, FRG: Wiley-VCH Verlag GmbH & Co. KGaA, 9 2003.
- [77] N. V. Smith, N. B. Brookes, Y. Chang, and P. D. Johnson, "Quantum-well and tight-binding analyses of spin-polarized photoemission from Ag/Fe(001) overlayers," *Physical Review B*, vol. 49, pp. 332–338, 1 1994.
- [78] K. Pedersen, C. Tomas, and P. Morgen, "Deposition and growth of Ag on Si(111) surfaces studied by optical second-harmonic generation," *Surface and Interface Analysis*, vol. 26, pp. 872–875, 11 2002.
- [79] D. Paramelle, A. Sadovoy, S. Gorelik, P. Free, J. Hobley, and D. G. Fernig, "A rapid method to estimate the concentration of citrate capped silver nanoparticles from UV-visible light spectra," *Analyst*, vol. 139, pp. 4855–4861, 7 2014.
- [80] C. Novo, A. M. Funston, I. Pastoriza-Santos, L. M. Liz-Marzán, and P. Mulvaney, "Influence of the medium refractive index on the optical properties of single gold triangular prisms on a substrate," *Journal of Physical Chemistry C*, vol. 112, no. 1, pp. 3–7, 2008.
- [81] A. Hilger, N. Cüppers, M. Tenfelde, and U. Kreibig, "Surface and interface effects in the optical properties of silver nanoparticles," *European Physical Journal D*, vol. 10, no. 1, pp. 115–118, 2000.
- [82] G. Lüpke, "Characterization of semiconductor interfaces by second-harmonic generation," 11 1999.
- [83] Donald A. Neamen, *Semiconductor physics and devices*. New York: McGraw-Hill Education, 4 ed., 2012.
- [84] D. Krause, C. W. Teplin, and C. T. Rogers, "Optical surface second harmonic measurements of Isotropic thin-film metals: Gold, silver, copper, aluminum, and tantalum," *Journal of Applied Physics*, vol. 96, pp. 3626–3634, 10 2004.
- [85] K. Pedersen, P. K. Kristensen, J. Rafaelsen, N. Skivesen, T. G. Pedersen, P. Morgen, Z. Li, and S. V. Hoffmann, "Optical second-harmonic generation and photoemission from Al quantum wells on Si(1 1 1) 7×7," *Thin Solid Films*, vol. 443, pp. 78–83, 10 2003.
- [86] D. Blanc, A. Cachard, J. C. Pommier, J. F. Roux, and J. L. Coutaz, "Characterization of aluminium nitride thin film structure using second-harmonic generation," *Optical Materials*, vol. 3, pp. 41–45, 2 1994.

- [87] F. Hajakbari, M. M. Larijani, M. Ghoranneviss, M. Aslaninejad, and A. Hojabri, "Optical properties of amorphous AlN thin films on glass and silicon substrates grown by single ion beam sputtering," *Japanese Journal of Applied Physics*, vol. 49, p. 095802, 9 2010.
- [88] A. Ichimiya and P. I. Cohen, *Reflection high-energy electron diffraction*. Cambridge University Press, 2004.
- [89] C. D. Rosa and F. Auriemma, *Crystals and Crystallinity in Polymers*. 2013.
- [90] N. B. Colthup, L. H. Daly, and S. E. Wiberley, *Introduction to infrared and Raman spectroscopy*. Academic Press, 3 ed., 1990.
- [91] R. C. Powell, *Symmetry, Group Theory, and the Physical Properties of Crystals*. Springer Berlin Heidelberg, 2010.

## Appendix A

# Temperature Measurements

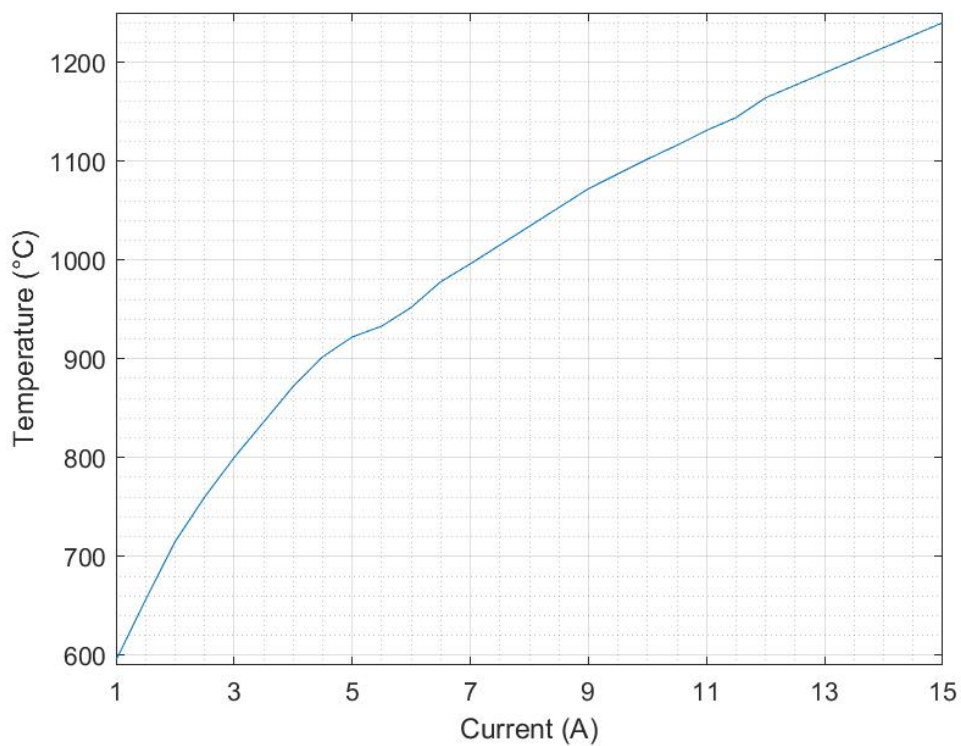


**Figure A.1:** Temperature measurements made on Si(111) surface after annealing and subsequent cooling to room temperature made with \*Insert name of equipment here\*.



# Appendix B

## AFM Histograms

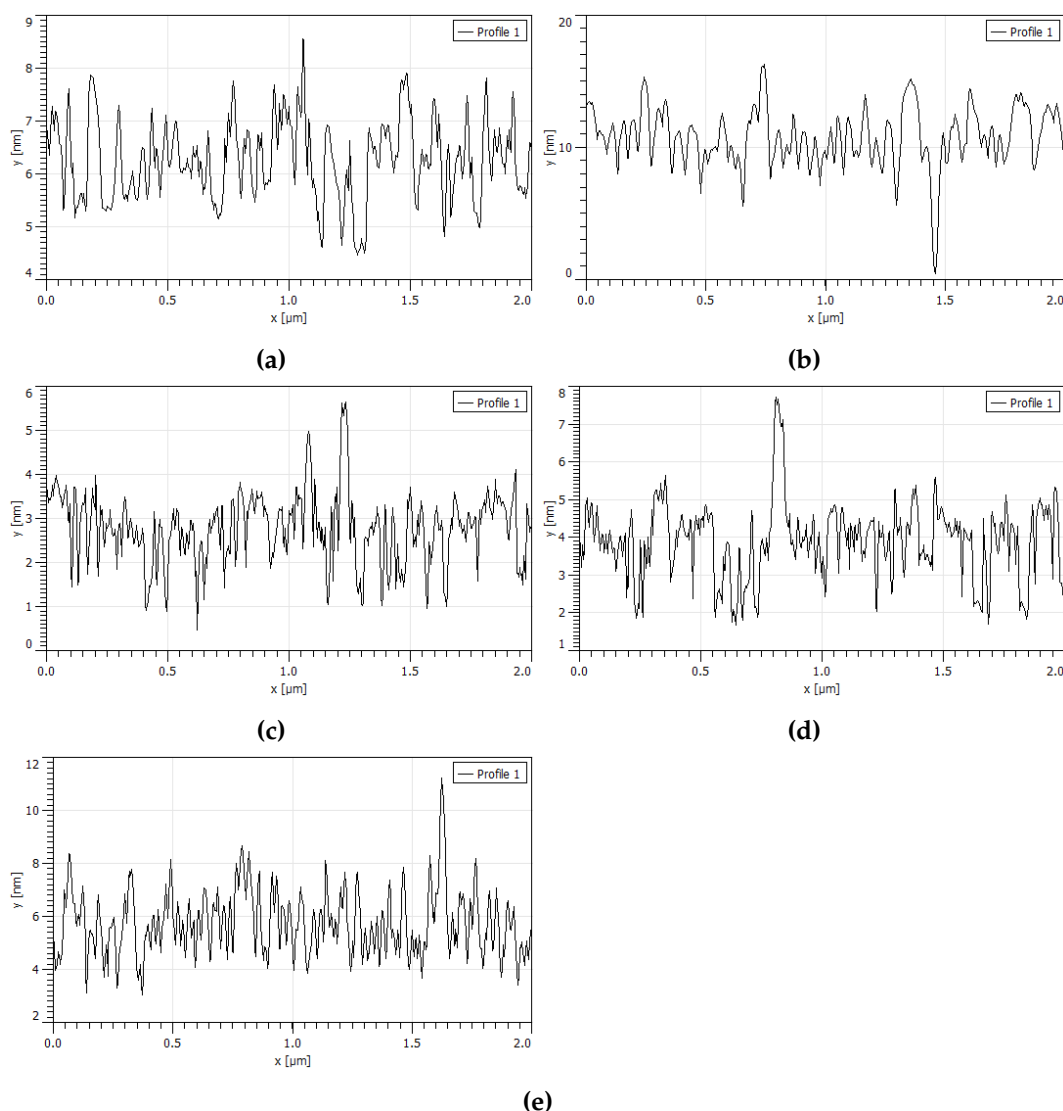


**Figure B.1:** AFM histograms correlating to a) Figure 3.7c. b) Figure 3.7d. c) Figure 3.7e. d) Figure 3.7g, e) Figure 3.7i



# Appendix C

## Equipment

tem # Prefix	GL5	GL10	GL10P	GL15
Extinction Ratio <sup>a</sup>			100 000:1	
Substrate		<a href="#">Laser Quality Natural Calcite<sup>b</sup></a> (Low Scatter)		
Transmitted Wavefront Error		≤λ/4 Over Clear Aperture at 633 nm		
Transmitted Beam Deviation		<3 arcmin		
Surface Quality (Input and Output Faces)		20-10 Scratch-Dig		
Surface Quality (Exit Ports)		80-50 Scratch-Dig		
Clear Aperture <sup>c</sup>	Ø5.0 mm	Ø10.0 mm	Ø10.0 mm	Ø15.0 mm
Prism Dimensions (W x L) <sup>d</sup>	6.5 mm x 7.5 mm	12.2 mm x 13.7 mm	12.2 mm x 16.5 mm	17.2 mm x 21.6 mm

Coating Specifications		
Coating Designation <sup>e</sup>	Reflectance <sup>f</sup> (Avg.)	Damage Threshold <sup>g</sup>
Uncoated (350 nm - 2.3 μm)	N/A	20 J/cm <sup>2</sup> (1064 nm, 10 ns, 10 Hz, Ø0.433 mm)
-A (350 - 700 nm)	<1%	10 J/cm <sup>2</sup> (532 nm, 10 ns, 10 Hz, Ø0.750 mm)
-B (650 - 1050 nm)	<1%	10 J/cm <sup>2</sup> (810 nm, 10 ns, 10 Hz, Ø0.155 mm)
-C (1050 - 1700 nm)	<1%	10 J/cm <sup>2</sup> (1542 nm, 10 ns, 10 Hz, Ø0.177 mm)
-C26 (1064 nm V Coating)	<0.25%	15 J/cm <sup>2</sup> (1064 nm, 10 ns, 10 Hz, Ø0.433 mm)

Figure C.1: Specifications for DMBP740B polarizer. 21.65 €

Item #	CWL <sup>a</sup>	FWHM <sup>b</sup>	T (Min) <sup>c</sup>	Blocking <sup>d</sup>	Transmission/OD Data <sup>e</sup>	Laser Line	Size
FL532-10	532 ± 2 nm	10 ± 2 nm	70%	200 - 1150 nm		Nd:YAG	Ø1"

Figure C.2: Specifications for FL05532-10 bandpass filter. 45.13 €

**Electrical Parameters**

Cathode type	-06	-07	-40	-40 mod	-42	-50
Wavelength range	220 nm - 650 nm	220 nm - 850 nm	300 nm - 720 nm	300 nm - 720 nm	300 nm - 870 nm	380 nm - 890 nm
Dark counts (cooled, typ. value)	< 100 cps	< 200 cps	< 700 cps	< 4000 cps	< 500 cps	< 1000 cps
Transit time spread (FWHM, typ. value)	< 50 ps	< 50 ps	< 120 ps	< 120 ps	< 130 ps	< 160 ps
Overload shutdown at	80 MHz (with CW excitation, lower values at different conditions)					
Single electron response width (typ. value)	600 ps					
Pulse rise/fall time (typ. value)	400 ps					

**Signal Output (Timing)**

Connector	SMA female
Impedance	50 Ohms
Polarity	negative

**Signal Output (Analog)**

Connector	SMA female
Impedance	> 1000 Ohms
Polarity	positive
Max. output voltage	+10 V (corresponds to 50 Mcps)
Time constant of the amplifier	20 $\mu$ s

**Figure C.3:** Specifications for PicoQuant PMA Hybrid series Photon Counting

Model	LightWire FP200
<b>MAIN SPECIFICATIONS <sup>1)</sup></b>	
Central wavelength	1064 nm, tunable $\pm 0.2$ nm
Pulse duration	$9 \pm 1$ ps
Spectral bandwidth	$0.25 \pm 0.05$ nm
Oscillator pulse repetition rate	$40 \pm 2$ MHz
Pulse repetition rate range using frequency divider	20 kHz – 40 MHz ( $PRR = PRR_{osc} / N$ , $N = 1, 4, 5, \dots, 2000$ )
Output power	> 200 mW at 10 MHz > 40 mW at 1 MHz > 5 mW at 100 kHz
Pulse energy	> 50 nJ at repetition rates < 200 kHz
Polarization	linear, vertical, > 100:1 extinction
Optical output	collimator & isolator node <sup>2)</sup> (free space output)
Umbilical	3 m length armored cable $\varnothing 5$ mm
Beam diameter	$0.9 \pm 0.1$ mm
Beam height	48 mm
Beam quality	$M^2 < 1.1$
Pulse train monitoring	photodiode output for oscillator train, TTL synch pulse for laser output
Dimensions of control unit (L $\times$ W $\times$ H)	315 $\times$ 450 $\times$ 95 (stand alone) or 315 $\times$ 482 $\times$ 95 (19" rack mountable)
Dimensions of collimator & isolator node (L $\times$ W $\times$ H)	164 $\times$ 72 $\times$ 73 mm
Weight (with/without pulse picker)	< 10 kg
Control interface	USB, CAN, RS232, LAN, WLAN
Power supply (AC/DC adapter included)	100 – 240 V, 50 – 60 Hz AC
Power consumption	maximal 230 W (typical 60 W)
Operating conditions	10 – 30 $^{\circ}$ C, humidity – not condensing

1. Due to continuous improvement all specifications are subject to change without notice.
2. FP200 model is provided with specially designed collimator & isolator node, which shouldn't be disconnected from output fiber without Ekspla approval.

**Figure C.4:** Specifications for Ekspla LightWire FP200 compact picosecond laser. 21000€

<b>Axial Force [Max]</b>	10N
<b>Cable Length [min]</b>	300mm
<b>Configuration</b>	Unipolar
<b>Current/Phase</b>	0.8A
<b>Detent Torque</b>	150 g-cm
<b>Dielectric Strength</b>	500 VAC for 1 minute
<b>Face Size</b>	NEMA 17
<b>Holding Torque</b>	2.6 kg-cm
<b>Housing Height [Max] (W)</b>	42.3mm
<b>Inductance/Phase</b>	6.7mH
<b>Insulation Resistance</b>	100 Megaohms Min. (500 VDC)
<b>Location Diameter (D)</b>	22mm
<b>Location Width (LW)</b>	2mm
<b>Motor Length (L)</b>	40mm
<b>Mounting Hole Width (H)</b>	31mm
<b>No. of Leads</b>	6
<b>No. of Phases</b>	2
<b>Operational Temperature Range</b>	-20/+50 Degrees C
<b>Radial Force [Max]</b>	28N (20mm from flange)
<b>Resistance/Phase</b>	7.5 Ohms
<b>Rotor Inertia</b>	54 g-cm <sup>2</sup>

**Figure C.5:** Specifications for Accu NEMA 17 Stepper Motor. 11.9€

## Appendix D

### $d_{eff}$ calculations for AlN

AlN has a hexagonal wurtzite structure, which gives d-matrix while assuming KSC is valid:

$$d = \begin{bmatrix} 0 & 0 & 0 & 0 & d_{15} & 0 \\ 0 & 0 & 0 & d_{15} & 0 & 0 \\ d_{15} & d_{15} & d_{33} & 0 & 0 & 0 \end{bmatrix}. \quad (D.1)$$

Linearly polarized light in a uniaxial crystal can be represented as a superposition of two waves with ordinary (o) and extraordinary (e) polarizations. Choosing a coordinate system, as seen in Figure D.1 with Z being along the optical axis of the uniaxial crystal. The polarization of the ordinary wave ( $p^o$ ) laying in the XY plane varying with the azimuthal angle  $\phi$  while being perpendicular to both  $k$  and Z. The polarization of the extraordinary wave ( $p^e$ ) laying in the  $kZ$  plane varying with both the incident angle  $\theta$  and  $\phi$ .

the effective d-matrix can be calculated from  $d_{eff} = p_3 \cdot dp_1 p_2$  with  $p_1$ ,  $p_2$  and  $p_3$  being either o or e polarized. Thus it can be written as,

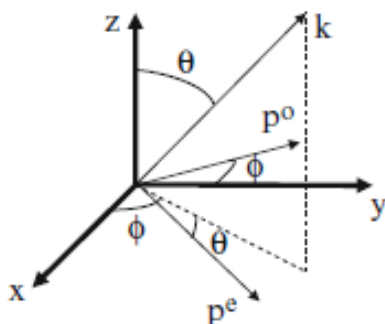


Figure D.1: Coordinate system for ordinary and extraordinary vectors. [91]

$$p_1 p_2 = \begin{bmatrix} p_{1x} p_{2x} \\ p_{1y} p_{2y} \\ p_{1z} p_{2z} \\ p_{1y} p_{2z} + p_{1z} p_{2y} \\ p_{1x} p_{2z} + p_{1z} p_{2x} \\ p_{1x} p_{2y} + p_{1y} p_{2x} \end{bmatrix}. \quad (D.2)$$

The  $Pp$  (eee) polarization will be evaluated.

$$d_{eff} = (\cos(\theta)\cos(\phi), \cos(\theta)\sin(\phi), -\sin(\theta))$$

$$\begin{bmatrix} 0 & 0 & 0 & 0 & d_{15} & 0 \\ 0 & 0 & 0 & d_{15} & 0 & 0 \\ d_{15} & d_{15} & d_{33} & 0 & 0 & 0 \end{bmatrix} \begin{bmatrix} \cos^2(\theta)\cos^2(\phi) \\ \cos^2(\theta)\sin^2(\phi) \\ \sin^2(\theta) \\ -2\sin(\theta)\cos(\theta)\sin(\phi) \\ -2\sin(\theta)\cos(\theta)\cos(\phi) \\ 2\cos^2(\theta)\sin(\phi)\cos(\phi) \end{bmatrix}. \quad (D.3)$$

Taking the dot product of the two matrices,

$$d_{eff} = (\cos(\theta)\cos(\phi), \cos(\theta)\sin(\phi), -\sin(\theta))$$

$$\begin{bmatrix} -2d_{15}\sin(\theta)\cos(\theta)\cos(\phi) \\ -2d_{15}\sin(\theta)\cos(\theta)\sin(\phi) \\ d_{15}\cos^2(\theta)\cos^2(\phi) + d_{15}\cos^2(\theta)\sin^2(\phi) + d_{33}\sin^2(\theta) \end{bmatrix}. \quad (D.4)$$

Now taking the dot product of the vectors,

$$d_{eff} = -2d_{15}\sin(\theta)\cos^2(\theta)\cos^2(\phi) - 2d_{15}\sin(\theta)\cos^2(\theta)\sin^2(\phi)$$

$$- d_{15}\cos^2(\theta)\cos^2(\phi)\sin(\theta)$$

$$- d_{15}\cos^2(\theta)\sin^2(\phi)\sin(\theta) - d_{33}\sin^3(\theta)$$

$$= d_{15}\cos^2\sin(\theta)(\theta)(-2\cos^2(\phi) - 2\sin^2(\phi) - \cos^2(\phi) - \sin^2(\phi))$$

$$- d_{33}\sin^3(\theta)$$

$$= -3d_{15}\cos^2(\theta)\sin(\theta) - d_{33}\sin^3(\theta) \quad (D.5)$$

Since the magnitude of  $d_{eff}$  is of primary interest, the sign can be changed.

$$d_{eff} = 3d_{15}\cos^2(\theta)\sin(\theta) + d_{33}\sin^3(\theta). \quad (D.6)$$